**University of Alberta**

# 3D ELASTIC-PLASTIC MODELLING OF A CRACKED PLATE AND A COMPOSITE PATCH REPAIR

by

**Folarin Edward Ozah** 

A thesis submitted to the Faculty of Graduate Studies and Research in partial fulfillment of the requirements for the degree of **Master of Science**.

Department of Mechanical Engineering

Edmonton, Alberta
Fall 2005

*Your file Votre référence*
*ISBN: 0-494-09253-X*
*Our file Notre référence*
*ISBN: 0-494-09253-X*

To God the Father, and the Lord Jesus Christ

# Abstract

Three-dimensional finite element method is utilized to analyse the plasticity-induced crack closure (PICC) phenomenon in a cracked plate under constant amplitude loading conditions, and variable amplitude loading conditions. The latter including a single spike tensile overload and a single compressive overload (underload). To accurately capture the PICC process the choice of material model is of vital importance, therefore this thesis considers a relatively new model, the Ellyin-Xia model, and the more widely employed kinematic hardening model. The study shows significant different in the results obtained while employing the two models.

The thesis extends the three-dimensional finite element model employed for the PICC analyses to the application of bonded patch repair technology. The study indicates that the application of a patch repair results in significant reduction in PICC (crack opening stress) and the stress intensity factor $K$, which is the driving force for crack propagation.

# Acknowledgements

I would like to thank Dr. Ellyin and Dr. Xia for encouraging and challenging me during my research, and also for their guidance and assistance while writing this thesis.

I would also like to thank the members of the Advanced Composite Materials Engineering Group for their occasional insight into the problem at hand.

# Contents

# List of Tables

# List of Figures

# Chapter 1

# Introduction

Cracks are flaws that exist in all kinds of structures, and are a cause of extreme concern to engineers in the design and during the service life of engineering structures. Their existence may be caused by inherent defects in material, the manufacturing process, in service fatigue damage, exposure to harsh environmental conditions and various other factors. The study of this phenomenon of cracks has led to the development of a branch of solid mechanics known as fracture mechanics, which deals with the characterization and behaviour of cracks in a stressed body. It provides a methodology for the evaluation under various loading conditions of bodies with these defects.

Linear elastic fracture mechanics (LEFM) is used to evaluate the crack boundary value problem (BVP) when the region at the crack tip responds based on the classical elasticity theory, where the crack tip is defined as the crack's cutting edge along the thickness of the the structure. In the majority of metallic materials, the presence of a high stress at the crack tip leads to the development of a plastic domain in the region around the crack tip resulting in the inaccuracy of LEFM. Therefore the material representation can no longer be elastic, leading to the requirement of a different material model formulation to evaluate the crack BVP. The case of particular interest in this study is when plastic deformation prevails in the inelastic domain requiring an elastic-plastic formulation to evaluate the cracked BVP. This necessitates a material

constitutive relation which describes the elastic-plastic behaviour to be employed.

If the loading condition of the structure is cyclic, after a critical number of cycles the already existent crack or a newly formed crack would tend to grow till it reaches a critical length where fracture of the structure occurs. The region between the start or detection of crack growth and the final fracture of the structure is depicted in Figure 1.1 where fatigue crack growth occurs, and it consists of three regions. Region I is the threshold regime where there is slow or no crack growth. Region II also called the Paris regime is where stable growth occurs and is the region of interest. And Region III, the fracture regime is where rapid unstable growth growth occurs and eventually, fracture takes place.

Let us now consider the cyclic loading process in the region of interest, Region II. During the loading section of a cycle, plastic deformation is induced around the crack tip and local plastic strains develop at the crack tip due to stress singularity. As the structure is unloaded, these strains are not fully reversed resulting in the formation of a plastic wake zone behind the crack tip as the front advances. Also upon unloading, the plastic deformation region leads to a zone of compressive residual stress at the crack tip and ahead of the front. These zones, mainly the plastic wake zone and partly the residual compressive stress zone combine to result in the plasticity-induced crack closure (PICC) phenomenon [5]. This phenomenon as the name implies results in a closure effect on the crack surfaces, requiring that the remote load applied overcomes these residual zones of compression before the crack can open.

In order to numerically model PICC with the finite element technique, the choice of a material constitutive relation for the elastic-plastic formulation will be of major importance in obtaining realistic solutions to the BVP. Although various material models exist to examine elastic-plastic behaviour, the classical models: elastic-perfectly plastic, isotropic hardening and kinematic hardening, widely used in finite element modelling of the PICC phenomenon in 3-D, have limitations. These material models either do not account for cyclic hardening (and) or the Bauschinger

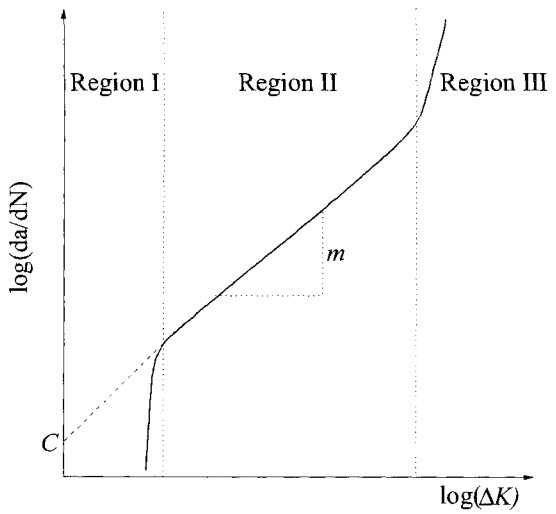


Figure 1.1: Fatigue crack growth behaviour

*The regime of interest is Region II which describes the crack growth rate as directly proportional to the stress intensity factor range.*

effect which are characteristics of engineering metals undergoing cyclic plasticity that affect the PICC process and consequently fatigue crack growth. As a result, this thesis investigates the use of a material model that accounts for these effects under constant amplitude loading, the effect of a tensile overload and the effect of a compressive overload (also referred to a an underload).

The growth of cracks may be arrested or retarded by using patch repair technology, where adhesively bonded composites or metals are used to bridge the crack providing reinforcement to the crack zone. The reinforcement provided by the bonded patch repair serves to transfer load away from the crack and strengthen the crack region. This causes a reduction in the stress singularity at the crack tip and the crack tip opening displacement, resulting in a reduction in the driving force for fatigue crack growth. Composites are the materials of choice for this technology as they can be designed to meet specific strength and service requirements and can easily be applied in situ. This thesis also investigates the use of composite patch repair technology considering the effect of varying patch thickness and the effect of

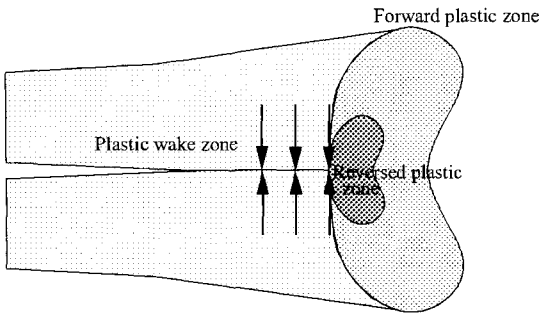


Figure 1.2: Plasticity zones inducing crack closure

*The zones of interest are the plastic wake zone behind the crack front; the reversed plastic zone which represents the yielded region in compression at minimum load ahead of the front. The forward plastic zone which represents the yielded region at maximum load - monotonic yield zone.*

PICC on crack growth arrest or retardation.

## 1.1 Plasticity-induced crack closure

The phenomenon of PICC as stated in the introduction to this chapter results from the combined effects of the plastic wake zone and the residual compressive zone (i.e the reversed plastic zone) as shown in Figure 1.2. During the unloading process of a cycle these zones cause the crack surfaces to close before minimum load is reached and upon reloading the crack surfaces do not open until the applied load overcomes the residual compressive stress in the plastic wake and reversed plastic zones. Therefore, the crack does not grow during the part of the cyclic loading when the crack surfaces are closed and it can only grow after the crack surfaces are fully open.

In order to predict fatigue crack propagation, Paris and Erdogan [9] defined the crack growth rate in Region II (see Figure 1.1) as

$$da/dN = C\,(\Delta K)^m, \tag{1.1}$$

where $a$ is the crack length, $N$ is the number of loading cycles, $C$ and $m$ are assumed to be material constants and $\Delta K$, the opening mode ($K_I$) stress intensity factor

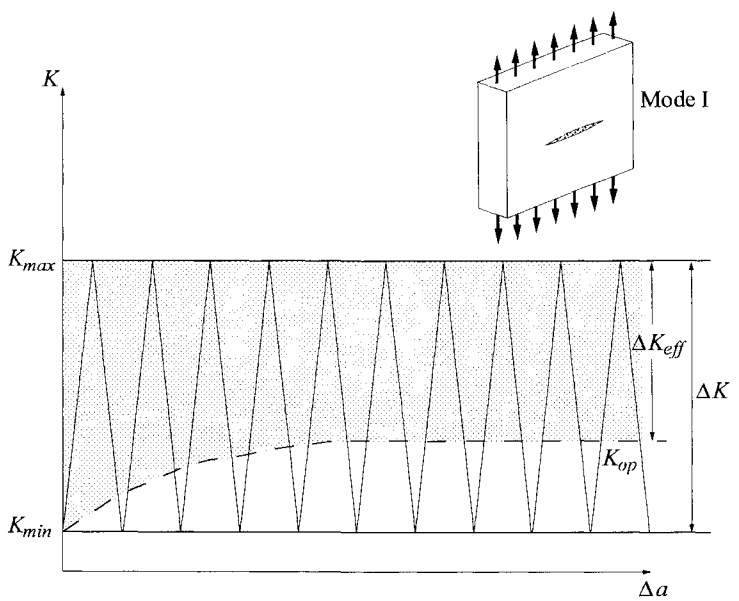


Figure 1.3: Crack opening mode I

*Shown here is crack opening profile in terms of $K_I$ for a middle-crack tension geometry.*

(SIF) range denoting the difference between the maximum and minimum values of $K_I$ (i.e $K_{max}-K_{min}$). Equation (1.1) is not valid for a material undergoing plasticity-induced fatigue crack closure because as stated in the preceding paragraph, fatigue crack growth can only occur while the crack is completely open during a loading cycle. To predict fatigue crack propagation when PICC occurs at the crack surfaces, a crack tip parameter was introduced by Elber [5], the effective stress intensity factor range $\Delta K_{eff}$, defined as the difference between $K_{max}$ and $K_{op}$, the opening mode SIF at the point when the crack surfaces become completely open during the loading portion of a cycle. Figure 1.3 shows a schematic of $\Delta K$ and $\Delta K_{eff}$. The Paris equation (1.1) for fatigue crack propagation is then modified for the case of PICC by replacing $\Delta K$ with $\Delta K_{eff}$, and the equation becomes

$$da/dN = C\,(\Delta K_{eff})^m\,. \tag{1.2}$$

The stress intensity factor, $K$ solutions, can not be obtained directly for the elastic-plastic formulation due to plasticity occurring at the crack front, rather the $K$

solutions are obtained from the path independent $J$-integral solutions which captures the stress and strain field intensity ahead of the crack tip by describing an arbitrary path independent contour away from, and enclosing the plasticity zone.

For PICC, the point at which the crack becomes fully open is defined by the size and extent of the plastic wake and reversed plastic zones, cyclic hardening and the Bauschinger effect. Therefore the $K_{op}$ solutions or the opening stress, $\sigma_{op}$, solutions depend on the material constitutive relation employed to describe these effects. An elastic-plastic material model introduced by Ellyin and Xia [6–8] which has been shown to capture and describe these effects is employed for this study using the finite element method.

## 1.2 Bonded Patch Repair Technology

To avoid catastrophic failures in engineering structures due to fatigue crack propagation, patch repair technology using adhesively bonded composite materials is employed to bridge the crack region as the patch has the following advantages [2, 10]: it can be manufactured to meet specific strength requirements and also as thin as possible so that it does not significantly affect the geometry of the cracked structure; reduces corrosion; additional stress concentrations are at reduced levels; allows for application to complex structural contours. The patch works based on two main mechanisms:

Due to the load-transfer characteristic of the bonded patch repair and its strengthening effect, there is a reduction in $\Delta\sigma$ in the cracked structure such that under opening mode loading conditions, the SIF $K_I$, for the patch repaired structure $K_{pr}$, does not go beyond a limiting value $K_\infty$ as shown in Figure 1.4 [1, 3] for the case of a thick patch repair of a thin plate. While for a thin patch repair of a thick plate, the crack opening stress governs the crack growth driving force $K$. Therefore the resulting reduction in the $\Delta K$ causing a reduction in the crack growth driving force. It can be seen that the SIF range employed in the Paris equation (1.1) for the patch

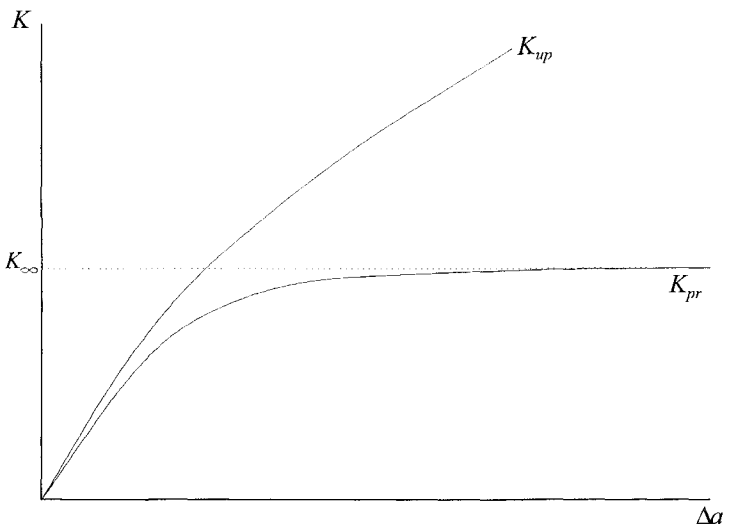


Figure 1.4: Reduction in $K$ with the application of a patch

*The stress intensity factor for the crack plate, $K_{up}$-(unpatched), is reduced to $K_{pr}$-(patched) for the patch repaired plate and the SIF does not exceed a limiting stress intensity factor, $K_\infty$.*

repair case is such that $\Delta K_{pr} < \Delta K_{up}$, which implies $\Delta N_{pr} > \Delta N_{up}$ (assuming $dN \approx \Delta N$, $da \approx \Delta a$, and that $\Delta a$ is the same for both cases) meaning that there would be an increase in the service life of the structure. Also due to the bridging effect of the patch repair, the crack tip opening displacement (CTOD) which is also a driving force in crack propagation is reduced by the constraining effect provided by the repair. The displacement is given by:

$$\delta_t = \frac{K_{eff}^2}{E\sigma_0} \tag{1.3}$$

Therefore as $K_{eff} \searrow$, $\delta_t \searrow$. This implies as $K_{eff} \to K_{th}$, $\delta_t \to 0$, resulting in an increase in fatigue life.

A number of researchers [4, 11] have shown that in practice, the patch and adhesive properties influence the performance of the bonded composite repair.

## 1.3 Layout of the Thesis

This chapter gives a brief introduction to the phenomenon of PICC and the technology of adhesively bonded patch repair. It outlines the major areas of fatigue and fracture mechanics used to investigate the PICC process, and the need of a material constitutive relation that captures and describes the effects of cyclic plasticity for this study. The chapter also briefly discusses the use of composite patch repairs as a way of restoring structural strength and increasing the service life of a cracked engineering structure.

Chapter 2, considers the 3-D plasticity-induced crack closure boundary value problem subject to constant-amplitude loading. A review of literature on the current state of 3-D finite element modelling of the plasticity-induced crack closure phenomenon is presented, with a more in-depth look at 3-D modelling. It outlines the limitations of current classical material models employed for 3-D analysis and considers the use of the proposed material constitutive relation which is implanted into the finite element computation code to account for the current limitations. The results obtained when employing this material model to solve the non-linear boundary value problem are compared to those obtained for the classical kinematic hardening material model.

Chapter 3 deals with the 3-D plasticity-induced crack closure boundary value problem subject to the application of a single spike tensile overload, and a single spike compressive overload (underload). A state of the art review on the effects of the application of an overload and an underload is presented. The effects of an overload and an underload in cyclic plasticity on the plasticity-induced crack closure process as captured by the Ellyin-Xia material model is presented and compared to the results obtained for the classical kinematic hardening model.

And in Chapter 4, an extension to the 3-D crack problem is presented using the Ellyin-Xia material constitutive relation introduced in chapter 2, that is the use of

bonded patch repair technology to repair a cracked plate using with a composite material. The effect of varying patch thickness on a thick plates is investigated. Also the effect of the plasticity-induced crack closure process on the repaired plate is presented.

Finally chapter 5 provides conclusions to the studies made in the thesis, and suggests future areas of research that might be of interest.

# Bibliography


[1] J. B. Avram. Fatigue response of thin stiffened aluminum cracked panels repaired with bonded composite patches. AFIT/GMS/ENY/01M-01, School of Engineering, Air Force Institute of Technology (AU), Wright-Patterson AFB OH, 2001.

[2] A. A. Baker. Repair of cracked of defective metallic components with advanced fibre composites - an overview of Australian work. *Composite Structures*, 2: 153–181, 1984.

[3] A. A. Baker. Crack patching: Experimental Studies, Practical Applications. In *Bonded Repair of Aircraft Structure*, pages 107–172, Dordrecht, 1988. Martinus Nijhoff Publishers.

[4] A. A. Baker. Bonded composite repair for fatigue-cracked primary aircraft structure. *Composite Structures*, 47:431–443, 1999.

[5] W. Elber. Fatigue crack growth under cyclic tension. *Engineering Fracture Mechanics*, 2:37–45, 1970.

[6] F. Ellyin. *Fatigue Damage, Crack Growth and Life Prediction.* Chapman & Hall, London, 1997.

[7] F. Ellyin and Z. Xia. A rate-independent constitutive model for transient non-proportional loading. *J. Mech. Phys. Solids*, 37(1):71–91, 1989.

[8] F. Ellyin, Z. Xia, and J. Wu. A new elastic-plastic constitutive model inserted into the user-supplied material model of ADINA. *Computers and Structures*, 56:189–208, 1992.

[9] P. C. Paris and F. Erdogan. A critical analysis of crack propagation. *Journal of basic engineering*, 85:528–534, 1963.

[10] P. D. Roberts. Patching cracked steel pressure vessels. Master's thesis, University of Alberta, Edmonton, Alberta, 1995.

[11] V. R. S. Turaga and S. Ripudaman. Modelling of patch repairs to a thin cracked sheet. *Engineering Fracture Mechanics*, 62:267–289, 1999.

# Chapter 2

# 3D Modelling of Plasticity Induced Fatigue Crack Closure: constant amplitude cyclic loading

## 2.1 Introduction

Many researchers have investigated the crack problem in engineering structures, and various mechanisms have been identified contributing to the crack closure in these structures: mainly the roughness of fracture surfaces, the presence of oxides, and the development of wake plasticity. Of interest in this study is wake plasticity, which is the primary mechanism of crack closure at medium and high $\Delta K$ values [2].

Since the phenomenon of plasticity induced crack closure PICC, was first identified by Elber [11], the finite element method has been used to successfully model the non-linear crack problem. Majority of these finite element studies consider 2-D models under plane strain and plane stress conditions, while 3-D simulations are relatively few. These 3-D crack closure studies are characterized by models that mostly employ either an elastic-perfectly plastic, an isotropic strain hardening or a kinematic hardening material model for the solution of the elastic-plastic formulation. Of these, only the kinematic hardening model captures the Bauschinger effect in cyclic plasticity which has been shown to have an important effect on the crack closure process [22, 25]. Therefore the solutions to the non-linear crack tip fields employing these models vary. It is therefore necessary to employ a material model that captures the PICC process accurately.

In this investigation, an elastic-plastic constitutive relation proposed by Ellyin and Xia [12, 14, 15] is employed as the material model for the solution of the non-linear problem subject to constant amplitude cyclic loading and the results obtained using this model are compared to those obtained with the classical kinematic hardening model.

## 2.2 State of the Art Review

The modelling of the PICC process in 3-D [3–5, 7, 23–25, 27, 29, 33, 34] allows for better understanding and prediction of the crack growth behaviour which can not be obtained with a 2-D model. These works have shown that due to the changing state of stress through the thickness of the plate, there is a variation in crack opening values along the crack tip resulting in tunnelling shape effect as the crack grows under cyclic loading conditions. Due to the complexity of modelling the shape evolution, the shape effect is usually neglected and the crack tip growth is modelled by advancing the crack tip a constant elemental length through the thickness of the geometry. Finite element procedure for modelling the PICC process in 3-D used by the noted works are basically the same and entail employing an elastic-plastic material formulation to permit the capture of plastic deformation occurring around the crack tip and the formation of wake plasticity which induces closure as the crack propagates. The model is cycled between maximum and minimum values based on the stress ratio, $R$. While the model is thus loaded, the stresses and displacements along the crack plane are monitored to determine when the crack opens or closes and also to detect crack surface contact so that the boundary conditions may be changed appropriately. And finally the crack is advance by node release once every cycle by an elemental length $\Delta a_e$ to model crack growth. In order to perform accurate finite element analyses using these procedures, there are a number of specific modelling issues that must be considered [17, 18, 21]. Following are the modelling issues with respect to 3-D analysis of the PICC process.

### 2.2.1 *Mesh generation and mesh refinement*

The finite element studies on 3-D models of the PICC process have considered the middle-crack tension (MT), Compact tension and part-through surface flaw geometries employing either eight-noded brick elements or six-noded elements. There is a tendency for these elements to exhibit plane strain locking at the vicinity around the crack tip exhibiting a state of stress similar to plane strain behaviour, and this locking can be avoided by using a reduced integration scheme or the $\overline{B}$ element formulation for the elements [29]. Also when 2-D or 3-D elements are used, the element aspect ratios must be taken into consideration around the crack tip because of the existence of high strain gradients with aspects ratio $\cong 1$ so that the results are not affected [26].

The mesh refinement issues for 3-D models are more complex than that of 2-D ones due to the state of stress variation through the thickness of the geometry. In the 3-D analysis, the state of stress changes from a near plane-stress condition at the exterior to a near plane-strain condition at the interior. These conditions give rise to a forward plastic zone at the exterior that is about three time the size of the interior forward plastic zone, therefore the interior plastic zone would be the governing factor for refinement. In order to perform mesh refinement studies for 3-D models, Skinner and Daniewicz [27] used the mesh refinement requirement for 2-D models [10, 19, 20] as a guideline which requires that to obtain convergence of crack opening value for PICC analyses under plane-strain conditions with a stress ratio $R = 0$, $\Delta a_e/r_f \leq 0.1$, where $\Delta a_e$ is an element size in the forward plastic zone $r_f$. More recently Solanki [30] has proposed the additional requirement for 2-D models [28] that there should be approximately 3-4 ($\Delta a_e$) elements in the reversed plastic zone $r_r$.

These investigations concluded that to obtain convergence of crack opening values there should be at least 5 $\Delta a_e$ element in the interior forward plastic zone (i.e $\Delta a_e/r_f \leq 0.2$) although the requirement that there should be about 3 to 4 $\Delta a_e$ elements in the interior reversed plastic zone (i.e $\Delta a_e)/r_r \leq 0.25$) could not be

satified by Solanki [30].

### 2.2.2 *Crack advance and crack surface contact schemes*

Modelling of the PICC process requires that the crack is propagated so that there is a formation of wake plasticity behind the crack tip and residual compressive stresses ahead of the crack tip which induce closure. In 3-D FE analyses the crack tip is advanced by an elemental length $\Delta a_e$ by crack tip node release through the thickness ignoring the shape evolution, thus simplifying the modelling process. It should be noted that such automatic propagation is independent of the strain and stress levels around the crack tip, thus making the analysis suitable for crack tip opening values prediction and not fatigue life propagation [29]. Now the question arises: after how many cycles and at what point during a load cycle should the crack be advanced?

Since the crack is generally advanced automatically with no criteria, it is advanced once every load cycle. And the point at which it should be propagated has lead researchers to investigate various options: mainly advancing at maximum or minimum load. The former which is considered more realistic but due to associated convergence difficulties the latter is used as an alternative. 3-D studies that have considered advance at maximum load with the MT geometry [5, 23, 27] have not encountered convergence difficulties. For the surface flaw geometry Solanki [30] conducted PICC analyses with node release at maximum and minimum load and found little difference in crack opening stress values. Zhang and Bowen. [33] also conducted node release for three schemes: advancing the crack at 10%, 50% and 100% of the maximum load showed no difference in crack opening displacement but minor variations in crack opening stress values.

As the crack is unloaded during these load cycles, the crack surfaces close resulting in surface contact and a variable boundary value problem. Various techniques have been employed to model the contact process and to avoid surface penetration and convergence difficulties. Chermahini et al. [5] employed a very stiff spring to constrain boundary displacements along the crack surface nodes when there is negative displacement and the spring is then removed by setting its stiffness to zero

if and when the displacement becomes positive to allow for opening during cyclic loading. Zhang and Bowen [34] used an interface element to monitor contact between the mesh geometry and the plane of symmetry by introducing a rigid surface along this plane. Recently the works reported in Refs. [27, 30] employed a more direct approach by monitoring the displacement of each crack surface node during unloading, when the displacement becomes zero or negative a nodal fixity is applied to simulate contact and prevent penetration. Upon reloading each node is monitored for a positive reaction force whereby the nodal fixity is removed.

### 2.2.3 *Determination of crack opening values*

In order to capture the trends of the PICC process through the thickness of the geometry with the finite element analysis another modelling question must be addressed: when is the crack fully opening or closed during a load cycle?

As with the other modelling issues different methods have been employed to determine crack opening values. Most 3-D analyses like 2-D studies determine crack opening levels by monitoring the displacement or the reaction force of each node on the crack surface, or the stress of each element adjacent to the crack surface behind the crack tip. Therefore the crack opening level is taken when the last crack surface node has a positive displacement or positive reaction force or the stress of last element becomes tensile through the thickness of the geometry. Likewise the closure levels are taken when these conditions are reversed.

Of interest here is the 2-D work of Wu and Ellyin [31] which suggests that these methods of determining the crack opening values are not accurate enough. For the crack to be considered opened it should have a potential to propagate and to be considered closed the potential should be removed. Therefore it was proposed that the nodal reaction force of the crack tip be monitored and when it becomes tensile the crack now has a potential to propagate, thus the crack is opened. Likewise when the reaction force becomes compressive at the crack tip the crack no longer has a potential to propagate, thus the crack is closed.

### 2.2.4 *Constitutive relationship*

3-D studies of PICC have mainly employed an elastic-perfectly plastic[3–7, 23, 27, 29], with a few of these studies considering material hardening with either an isotropic strain hardening [33, 34] or a kinematic hardening model [24, 25]. These hardening models have employed a bi-linear material relationship. Skinner and Daniewicz [27] have shown that as the hardening slope $H$ is increased the crack opening values decrease. This implies as $H$ is increased $\Delta K_{eff} = K_{max} - K_{op}$ is also increased resulting in a larger driving force for crack propagation. Also Roychowdhury and Dodds Jr. [25] compared the effects of using an isotropic hardening vs. a kinematic hardening model, and found that the results obtained showed considerably higher crack opening values for the isotropic hardening model than the kinematic hardening model which means that the resulting driving force $\Delta K_{eff}$ is lower for the former. These works show that the crack opening values are strongly influenced by the choice of the constitutive relationship employed. Therefore, the choice of an appropriate elastoplastic model becomes an important issue to correctly capture the behaviour of industrial materials.

### 2.2.5 *Statement of the Problem*

Although the development of wake plasticity behind the crack tip and a zone of residual compressive stress at and ahead of the crack tip at minimum load are primary to the PICC process as discussed in chapter one, other effects of cyclic plasticity on the process also need to be considered. A cracked structure undergoing cyclic plasticity at the crack tip will be strongly influenced by cyclic hardening and/or softening and by the Bauschinger effect [22] which affect the PICC process. Therefore a material model that better describes the cyclic plastic behaviour and the resulting effects on the material, while subject to constant-amplitude loading; will be of paramount value in the analysis of this closure mechanism. Thus the solution to the non-linear PICC problem is dependent on the choice of the elastic-plastic constitutive relation employed for the analysis.

As stated earlier, the majority of the reported 3-D studies employ an elastic-

perfectly plastic, while a few have used an isotropic strain hardening material model, both of which ignore the Bauschinger effect in cyclic plasticity, thus giving solutions that over predict the crack opening level. This is because the Bauschinger effect tends to increase the level of damage accumulation at the crack tip resulting in a reduction in the crack opening level [22, 25]. Although the kinematic hardening model considers the Bauschinger effect, there is a need to consider alternate material models that can more adequately capture the hardening or softening process associated with cyclic plasticity.

This study considers the use of a material constitutive relationship proposed by Ellyin and co-workers [12, 14, 15] which can be used to simulate quasi-static proportional and non-proportional loadings conditions while accurately capturing the effects of cyclic plasticity and it is employed as the material model for the elastic-plastic formulation. So why employ this model? The model is chosen for the following reasons [31]:

- the motion of the yield surface is described by the current yield surface, the memory surface and the limit memory surface which characterize certain material properties and these can be obtained experimentally. Thus, the model gives a description of the evolution of the yield surface which is closer to that obtained experimentally as compared to the more widely used classical models.

- the size of the yield surface is given as a function of the material's cyclic behaviour (e.g. non-Masing and Masing behaviour). Therefore the Ramberg-Osgood relation which has three parameters for a better fit to experimental curves is used to fit the uniaxial experimental curves of the material.

This material model is used to solve the non-linear crack problem subject to constant amplitude loading conditions. The kinematic hardening model provided in the ANSYS® material model library [1] is also employed for comparative purpose.

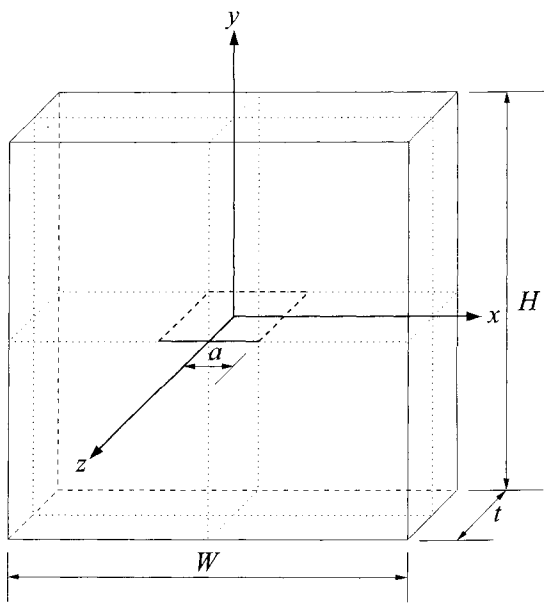


Figure 2.1: Middle-tension geometry
*With its three planes of symmetry, xy, yz and zx.*

## 2.3 Finite Element Model

The following sections describe the geometrical model and mesh generation, crack advance and crack surface contact schemes, determination of crack opening values, elastic-plastic material constitutive models employed, boundary and loading conditions, and the computational code used.

### 2.3.1 *Geometric model and mesh generation*

In this study a middle-crack tension geometry is considered similar to the 2-D model used by Wu and Ellyin [16, 31]. The current study considers a 3-D geometrical configuration as shown in Figure 2.1, having the following dimensions: height, $H$ = 80mm; width, $W$ = 80mm; thickness, $t$ = 8mm and an initial crack length, 2a = 8mm. The material was assumed to be ASTM 516 Gr. 70 steel employing: a) a bi-linear kinematic hardening model similar to that used in Ref. [31], and b) The Ellyin-Xia material constitutive relationship. Due to symmetry only one-eighths of the plate is modelled.

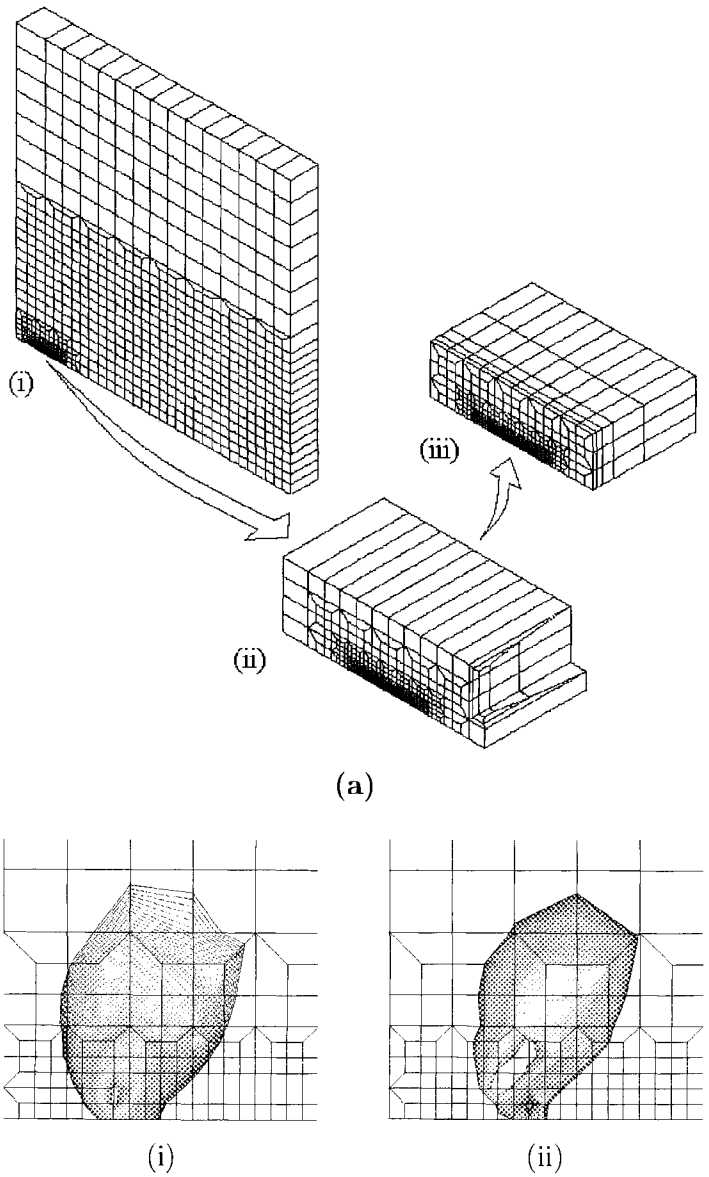


Figure 2.2: Mesh refinement

*a) shows how the mesh is refined with special consideration for the region around the crack tip, and b) which shows the number of elements in the forward plastic zones for the i) Ellyin-Xia model and ii) kinematic hardening model.*

Modelling of the cracked plate employing the kinematic hardening model is accomplished using a 3-D 8-nodes structural solid, SOLID45, while the modelling of the cracked plate incorporating the Ellyin-Xia constitutive relation is achieved using a 3-D 8-nodes structural solid in the 18x family elements, SOLID185, which permits the use of the ANSYS User Programmable Features routine USERMAT.

Figure 2.2(a) shows a typical mesh of the model. The region away from the crack tip consists of single layered brick elements as shown in Figure 2.2(a-i) with a transition to five layers through the half-thickness of the plate in the vicinity of the crack tip (see Figures 2.2(a-ii) and 2.2(a-iii)). These five layer thicknesses are chosen to match the works of Roychowdhury and Dodds Jr. [24, 25] which have layer thicknesses of $0.25t$, $0.15t$, $0.05t$, $0.03t$ and $0.02t$ where the smallest layer was located on the exterior surface of the model ($z = 0.5t$). These thicknesses allow for adequate capture of the state of stress through the half-thickness of the plate which rapidly changes from near plane strain conditions at the interior of the geometry to near plane stress conditions at the exterior surface [4, 5, 7].

The mesh has its finest refinement at the crack tip region with the smallest element length $\Delta a_e$ by which the crack is propagated once every cycle. As discussed in the state of the art review, the plastic zone must contain a minimum number of smallest elements to properly capture the PICC process. Therefore, a mesh refinement study was performed using $\Delta a_e = 0.08$mm, 0.04mm, and 0.02mm. Each mesh was checked against the following: a) the requirement for 2-D models that $\Delta a_e/r_f \leq 0.1$ and $\Delta a_e)/r_r \leq 0.25$, where $r_f$ is the forward plastic zone and $r_r$ is the reversed plastic zone. These are assumed to be the area defined by the ratio of von-Mises stress to yield stress $\sigma_e/\sigma_o \geq 0.95$ at maximum and minimum load respectively. b) the works of Solanki [30] and Skinner and Daneiwicz [27] which stated that five elements in the forward plastic zone of the interior surface (near plane strain region) of a 3-D model is sufficient to obtain convergence of crack opening levels. Figures 2.2(b-i) and 2.2(b-ii) show the number of $\Delta a_e = 0.02$mm elements in the forward plastic zone for the interior surface at maximum load during the 2nd load cycle for the Ellyin-Xia model and the kinematic hardening model

respectively (by the 5th load cycle both models have a minimum of $5\Delta a_e$ elements in the forward plastic zone). The number of $\Delta a_e$ elements in the plastics zones are given in Table 2.1 for the three meshes for the case of the kinematic hardening model.

Table 2.1: Elements in plastic zones

| Mesh | Plastic zone | | | |
|---|---|---|---|---|
| $\Delta a_e$ | Forward | | Reversed | |
| | exterior | interior | exterior | interior |
| 0.08mm | 2 | 1 | 0 | 0 |
| 0.04mm | 6 | 3 | 1 | 0 |
| 0.02mm | 11 | 5 | 3 | 2 |

Figure 2.3 shows mesh convergence plots for stabilized opening levels for the MT geometry employing two material models. These show that the mesh with $\Delta a_e = 0.02$mm satisfies the requirements for convergence and the plots for the geometry employing the two material models show that there is convergence for this mesh refinement, therefore this mesh is used for all analyses and consists of 4129 elements and 5798 nodes with 17394 degrees of freedom.

### 2.3.2 *Crack advance and crack surface contact schemes*

For this study the crack is advanced at the top of the load cycle similar to previous 3-D works. And the crack closure scheme was modelled similar to that used by Skinner et al. [26, 27].

The contact scheme employed is as follows: during unloading the displacement values of the crack surface nodes were monitored, once a surface node has negative displacement the node is constrained in the crack surface plane. After the unloading path at minimum load the constrains on the surface nodes are removed before reloading.

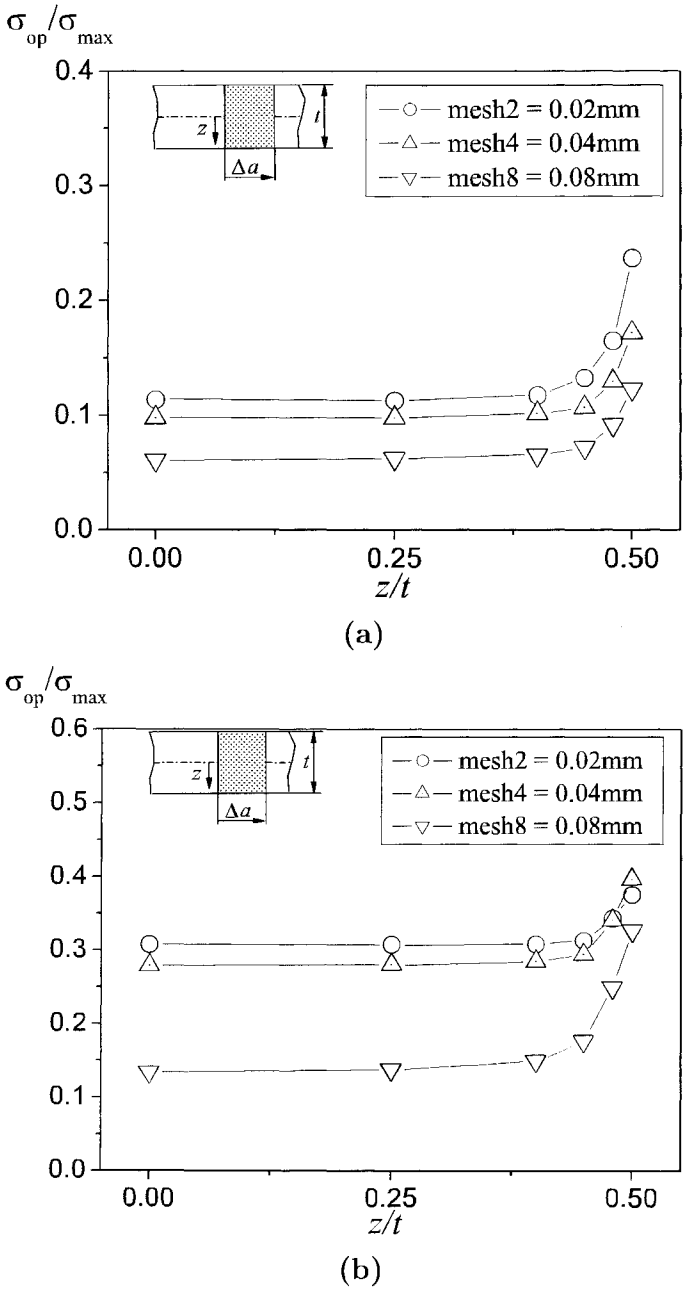


Figure 2.3: Convergence plots

*a) Ellyin-Xia model, and b) Kinematic hardening model*

### 2.3.3 *Crack opening determination*

The work of Wu and Ellyin [31] was extended to this study whereby the crack should have a potential to propagate to be considered opened. During the propagation the

crack must tear through its present front to grow. The works of Ref. [5, 9, 24] show that the crack opening profile follows the trend in Figure 2.4, therefore the front will be the last region to have tensile stresses before the crack can grow. For this study the crack tip nodes were monitored and when the reaction force of a node becomes tensile that point along the front is taken as open. In order to obtain a more accurate crack opening value at the crack tip nodes each nodal reaction force was monitored for each load step and once it became tensile (positive), the zero value was obtained by linear interpolation between this tensile value and the compressive (negative) value from the previous load step.

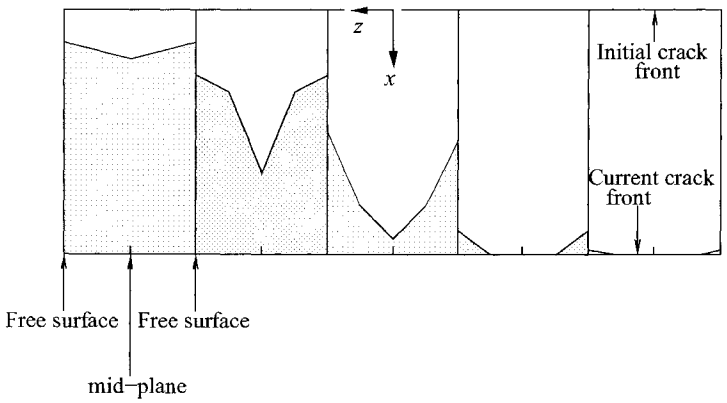


Figure 2.4: Crack opening profile

*Evolution of the crack surface on the crack plane during the loading path adopted from Ref.* [24]

### 2.3.4 *Elastic-plastic constitutive models*

#### Kinematic hardening model

The classical elastic-plastic material constitutive model considered in this study is a rate-independent kinematic hardening model provided in the ANSYS finite element code as its described the effects of cyclic plasticity more accurately than the other widely used classical models; elastic-perfectly plastic and isotropic hardening, used in 3-D modelling of PICC. When a material described by this model attains a stress state defined by the yield surface then a permanent deformation occurs and the

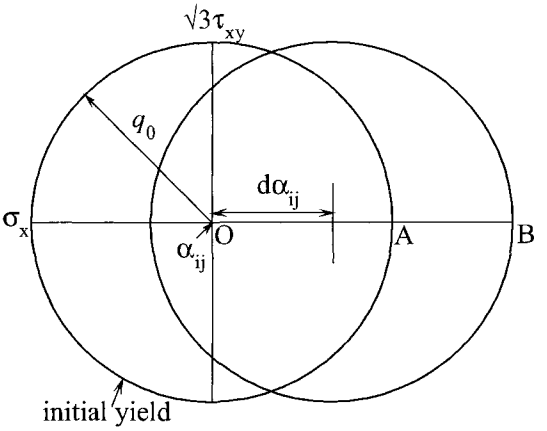


Figure 2.5: Yield surface for the kinematic hardening model.
*The yield surface translates in stress space, but remains constant in shape and size.*

material undergoes plastic flow. The yield function is given by:

$$\phi_y = f_y(\sigma_{ij} - \alpha_{ij}) - q_0^2 = 0. \tag{2.1}$$

This condition defines the yield surface with the back stress tensor, $\alpha_{ij}$, which specifies its centre, and $q_0$ which specifies the constant radius of the surface. As shown in Figure 2.5, the yield surface translates in stress space while remaining constant in shape and size. Because the plastic strain is path-dependent, the flow law defines the plastic strain in incremental form in terms of a plastic potential, $\Phi(\sigma_{ij})$, introduced by von Mises and is given by:

$$d\epsilon_{ij}^p = d\lambda \frac{\partial \Phi(\sigma_{ij})}{\partial \sigma_{ij}}, \tag{2.2}$$

where $\Phi$ is a scalar function of stress, and $d\lambda$ is also a non-negative scalar. As the surface translates, the increment in $\alpha_{ij}$ can be expressed as

$$d\alpha_{ij} = c d\epsilon_{ij}^p, \tag{2.3}$$

in which $c$ is a constant. The ANSYS theory manual [1] provides a full description of the application of this material model.

When employing the kinematic hardening model, the following material properties were used, see Table 2.2.

Table 2.2: Kinematic Hardening model: material properties

| **Property** | **Value** |
|---|---|
| Young's modulus, $E$ (GPa) | 204GPa |
| Poisson's ratio, $\nu$ | 0.30 |
| Tangent modulus, $E_t$ (MPa) | $E/20$ |
| Yield stress, $\sigma_o$ (MPa) | 230MPa |

**Ellyin-Xia material model**

This model is a rate-independent constitutive relation which defines two stress hypersurfaces that describe the evolution of the yield locus in stress space. The primary hypersurface, the yield surface, depends on the loading history defined by the locus of the elastic domain and defines the boundary between elastic and plastic loading while always remaining inside the secondary hypersurface, the stress memory surface, which describes the locus of the maximum equivalent stress experienced in the pervious loading history of the material. Figure 2.6 shows the evolution of the yield locus. The yield and memory surfaces are given by:

$$\varphi_y = f_y(\sigma_{ij} - \alpha_{ij}) - q^2 = 0, \tag{2.4}$$

$$\phi_m^\sigma = f_m^\sigma(\sigma_{ij} - \beta_{ij}) - R_{mem}^2(\sigma_{eq,max}) = 0. \tag{2.5}$$

respectively, where $\alpha_{ij}$ and $\beta_{ij}$ specify the location of the centre of the yield and memory surfaces respectively. And $q$ and $R_{mem}$ denote the size (radius) of the yield and memory surfaces respectively. For the case of a von Mises material:

$$f_y = \frac{3}{2}\bar{s}_{ij}\bar{s}_{ij}, \tag{2.6}$$

$$f_m^\sigma = \frac{3}{2}\hat{s}_{ij}\hat{s}_{ij}, \tag{2.7}$$

where

$$\bar{s}_{ij} = \sigma_{ij} - \delta_{ij}\bar{\sigma}_{kk}/3 \quad \text{and} \quad \bar{\sigma}_{ij} = \sigma_{ij} - \alpha_{ij},$$

$$\hat{s}_{ij} = \hat{\sigma}_{ij} - \delta_{ij}\hat{\sigma}_{kk}/3 \quad \text{and} \quad \hat{\sigma}_{ij} = \sigma_{ij} - \beta_{ij}.$$

The total stress increment is defined in terms of its elastic and plastic parts:

$$d\epsilon_{ij} = d\epsilon_{ij}^e + d\epsilon_{ij}^p \tag{2.8}$$

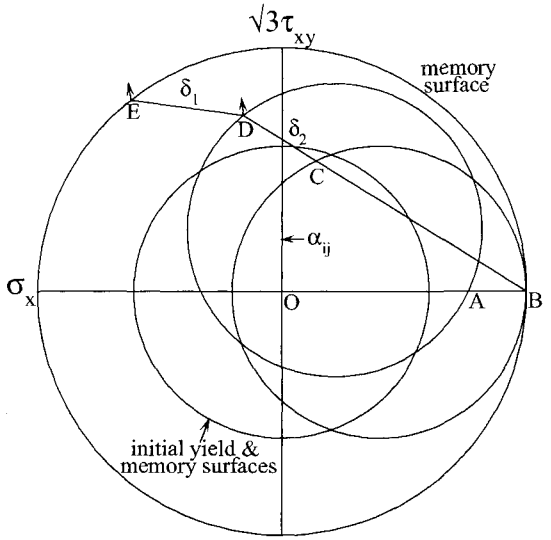


Figure 2.6: Stress hypersurfaces of Ellyin-Xia model

*The evolution of yield locus is described by the two hypersurfaces; yield and memory surfaces in stress space.*

The elastic part is obtained by using the generalized Hooke's law, and the plastic part of the total strain increment is given by:

$$d\epsilon_{ij}^{p} = cg\frac{\partial f_y}{\partial \sigma_{ij}}\frac{\partial f_y}{\partial \sigma_{kl}}d\sigma_{kl}, \tag{2.9}$$

where $c$ is defined by the state of stress and is taken as:

$$\begin{aligned} c = 1 \quad &\text{for} \quad \frac{\partial f_y}{\partial \sigma_{kl}}d\sigma_{kl} \geq 0 \quad \text{and} \quad f_y(\sigma_{ij} - \alpha_{ij}) - q^2 = 0 \\ c = 0 \quad &\text{for} \quad \frac{\partial f_y}{\partial \sigma_{kl}}d\sigma_{kl} < 0 \quad \text{or} \quad f_y(\sigma_{ij} - \alpha_{ij}) - q^2 < 0 \end{aligned} \tag{2.10}$$

and $g$ is the hardening modulus, and is given by:

$$g = \frac{1}{4q^2}\left(\frac{1}{E_t} - \frac{1}{E}\right), \tag{2.11}$$

$E$ is the modulus of elasticity and $E_t$ is the tangent modulus which is dependent on the mode of plastic loading. The Ellyin-Xia model defines two modes of plastic loading that describe the movement of the yield surface, stress memory surface and the tangent modulus.

The first is monotonic loading, ML, in which the stress memory surface expands while remaining tangent to the yield surface as the yield surface moves within the

memory surface as shown in the path AB in Figure 2.6 [12]. In order to determine the movement of the yield surface in this case, a Ziegler type rule is used where the motion of the surface is defined as function of stress, the present location of the centre of the surface and a scalar function $d\mu$.

$$d\alpha_{ij} = d\mu(\sigma_{ij} - \alpha_{ij}) \tag{2.12}$$

As stated earlier the stress memory surface remains tangent to the yield surface, therefore to ensure that this condition is satisfied for any particular stress state during ML, the movement of the centre of the memory surface $\beta_{ij}$ is obtained from the following equations:

$$\begin{aligned} &\frac{\partial f_y(\sigma_{ij} - \alpha_{ij})}{\partial \sigma_{ij}} = \lambda \frac{\partial f_y^{\sigma}(\sigma_{ij} - \beta_{ij})}{\partial \sigma_{ij}} \\ &f_y^{\sigma}(\sigma_{ij} - \beta_{ij}) - R^2 = 0 \end{aligned} \tag{2.13}$$

The second mode of plastic loading is reloading, RL, in which plastic deformation occurs after an elastic unloading. In this case the yield surface moves within the stress memory surface but does not remain tangent to it, as shown in path CD of Figure 2.6 [12]. Therefore the memory surface remains constant in size implying that the maximum equivalent stress value experienced remains the same during RL. Once the yield surface contacts the memory surface so that they are once again tangent, the plastic loading mode switches to ML. The movement of the yield surface centre along the direction of the line DE is obtained using a Mróz type rule:

$$d\alpha_{ij} = d\mu(\sigma_{ij}^{m} - \sigma_{ij}^{y}), \tag{2.14}$$

And the evolution of the memory stress surface is given by:

$$\frac{\partial \beta_{ij}}{\partial \ell_p} = \zeta(\sigma_{ij}^{mean} - \beta_{ij}) \tag{2.15}$$

where the mean stress $\sigma_{ij}^{mean}$ is the geometric centre of the cyclic stress path and $\ell_p$ is the accumulated plastic strain given by:

$$\ell_p = \int \left( \frac{2}{3} d\epsilon_{ij}^{p} d\epsilon_{ij}^{p} \right)^{1/2}. \tag{2.16}$$

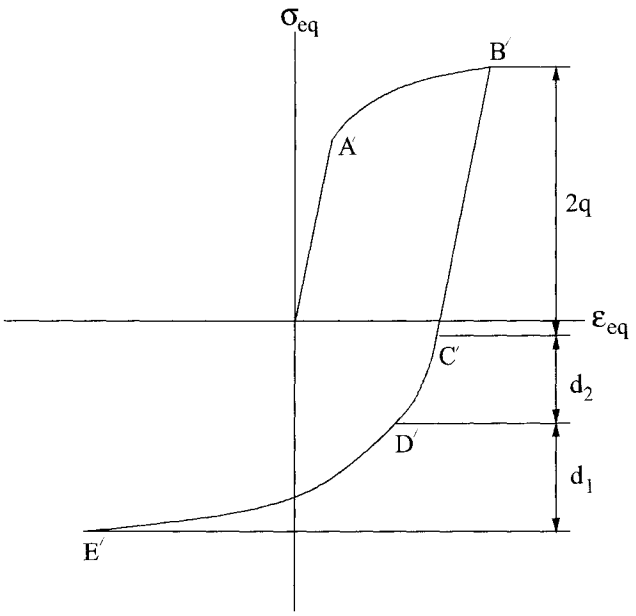


Figure 2.7: Uniaxial stress-strain curve

*Used for the determination of the tangent modulus, $E_t$ from the evolution of the yield surface.*

As stated earlier the tangent modulus is also dependent on the mode of plastic loading, and for the ML mode of plastic loading the tangent modulus $E_t$ is defined as a function of the equivalent stress and can be obtained using the following equation:

$$E_t = f(\sigma_{eq}) \tag{2.17}$$

While the tangent modulus for this case of RL plastic loading $E_t$ is given as a function of the form:

$$E_t = E_t(\sigma_{eff}, r) \tag{2.18}$$

where $r$ is given as the ratio:

$$r = \frac{\delta_1}{\delta_2} = \frac{d_1}{d_2} \tag{2.19}$$

$\delta_1$ is the distance DE and $\delta_2$, the distance CD, see Figure 2.6 [12]. And $r$ defines a corresponding point D′ on the reversed uniaxial stress-strain curve B′C′E′ such that $d_1$ and $d_2$ are the paths D′E′ and C′D′ respectively as shown in Figure 2.7 [12]. Transient hardening is captured by changes in the tangent modulus and the radius

of the yield surface which are measured by the accumulated plastic strain $\ell_p$ and these are given by:

$$q = q_{st} - (q_{st} - q_0)e^{-\beta \ell_p} \tag{2.20}$$

$$E_t = E_{t,st} - (E_{t,st} - E_{t,0})e^{-\beta \ell_p} \tag{2.21}$$

where $q_{st}$ is the yield surface and $E_{t,st}$, the tangent modulus at the saturated state and $q_0$ and $E_{t,0}$ are the corresponding monotonic (virgin) state values. For this study it was assumed that the material was already at stable state at the start of the analysis, i.e $\beta = 0$, therefore the monotonic curve is equal to the saturated curve. The above equations (2.20 and 2.21) become:

$$q = q_{st} \tag{2.22}$$

$$E_t = E_{t,st} \tag{2.23}$$

The materials properties are given in Table 2.3 and the virgin and cyclic stable stress-strain curves assumed to coincide and be represented by Ramberg-Osgood relation:

$$\frac{\epsilon_e}{\epsilon_0} = \frac{\sigma_e}{\sigma_{0c}} + \alpha \left( \frac{\sigma_e}{\sigma_{0c}} \right)^{1/n} \tag{2.24}$$

where $\sigma_e$ is the von Mises effective stress and $\epsilon_e$ is the corresponding effective strain, and $\alpha$ is taken as 0.02 and $1/n$ as 6.0 similar to the work of Wu [16]. Figure 2.8 shows the uniaxial stress-strain curve.

Table 2.3: Ellyin-Xia model: material properties

| **Property** | **Value** |
|---|---|
| Monotonic yield stress, $\sigma_o$ (MPa) | 230 |
| Cyclic yield stress, $\sigma_{oc}$ (MPa) | 230 |
| $\beta$ | 0 |

The model is implemented into the ANSYS finite element code using the User Programmable Features routine USERMAT (see Appendix A for the verification of the routine).

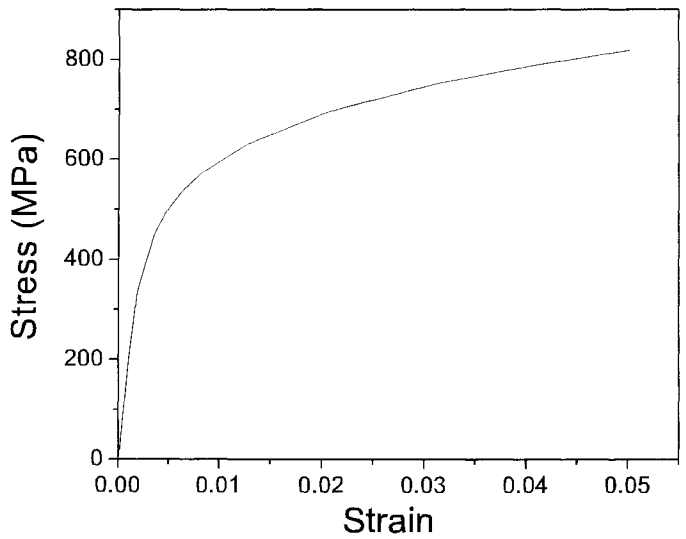


Figure 2.8: Stress-strain curves

*The virgin (initial) and stable (saturated) curves are the same for this study*

### 2.3.5 *Boundary conditions and loading*

Taking advantage of symmetry about the $xy$, $yz$ abd $zx$ planes, the following boundary conditions are applied to the model (see Fig. 2.1):

$$u_x(0, y, z) = 0 \quad \rightarrow \quad 0 \leq y \leq H/2; \quad 0 \leq z \leq t/2$$
$$u_y(x, 0, z) = 0 \quad \rightarrow \quad a \leq x \leq W/2; \quad 0 \leq z \leq t/2$$
$$u_z(x, y, 0) = 0 \quad \rightarrow \quad 0 \leq x \leq W/2; \quad 0 \leq y \leq H/2$$

The MT geometrical model was subjected to 20 constant-amplitude loading cycles with a stress ratio $R = 0$ and maximum stress $\sigma_{max} = 0.3\sigma_o$. Figure 2.9 shows a typical load cycle which comprises of approximately 83 load steps. During the loading path of a cycle a load of 1% of $\sigma_{max}$ is incrementally applied until the crack is fully open in order to provide good resolution for the detection of crack opening values and then by 10% of $\sigma_{max}$ thereafter. And during the unloading path of a cycle, the load is incrementally decreased by 5% of $\sigma_{max}$ before closure begins, 2% during closure until the crack is fully closed and then by 10% of $\sigma_{max}$ thereafter.

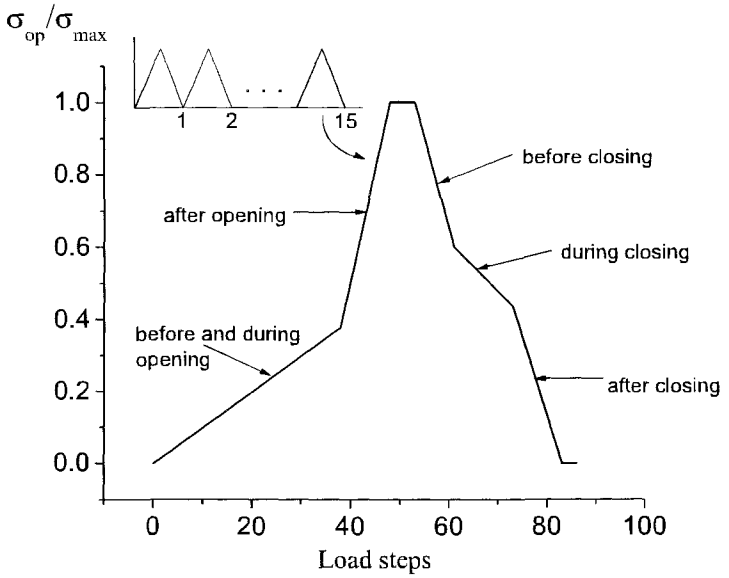


Figure 2.9: A typical loading cycle

*Shown are the different loading sections employed for reduced solution time while having convergence.*

### 2.3.6 *Computational code*

The PICC analyses were performed using the ANSYS finite element code ANSYS 6.0. In order to perform multiple batch runs and repeated analyses a batch script was written in the ANSYS Parametric Design Language, APDL. The summary of the script is as follows:

- mesh generation and definition of the material model
- application of initial boundary conditions

the script is then looped 20 times to represent 20 cycles as follows:

- loading path and determination of crack opening values
- crack advance by one element at maximum load
- unloading path, determination of closing values and crack surface contact

The analyses were conducted using the pre-conditioned conjugate gradient (PCG) iterative solver to within a tolerance of $1e-8$ to reduce disk usage and computation time. Due to the nonlinear nature of the PICC, SOLCONTROL, ON command was used to activate ANSYS optimized defaults for nonlinear solutions employing the full equilibrium iterations to ensure convergence for each load increment within a load step.

The opening stress results obtained for the $\Delta a_e$ 0.2mm mesh and the kinematic hardening model using the APDL script were checked against the results of Wu [16, 31] employing the stress-strain curve shown in Figure 2.8. Figure 2.10 shows that the crack opening values at the free surface (near plane stress region) of this 3-D study agrees well with the 2-D plane stress results of the above references. Note that these analyses are conducted to characterize the through thickness closure trends and not to predict exact crack opening values. At this stage it maybe worthwhile to point out

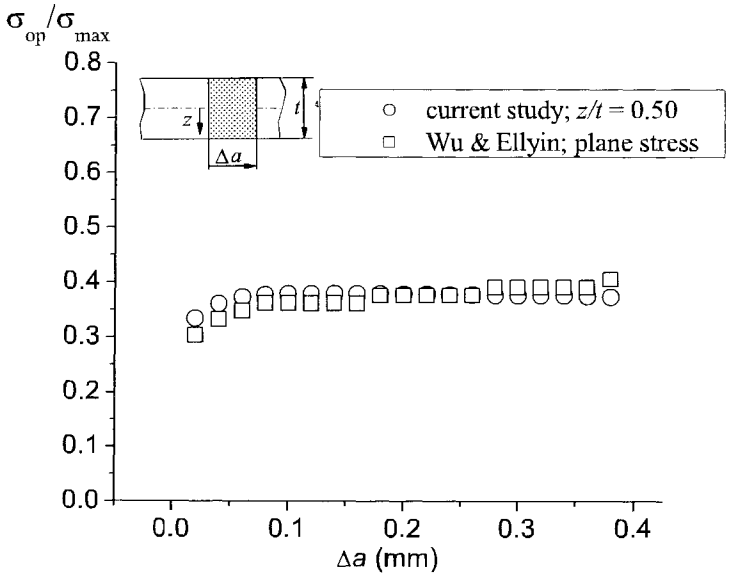


Figure 2.10: Verification plot

*Crack opening values of this work at free surface compare with the 2-D work of Wu and Ellyin.* [31]

that the concept of crack growth at each cycle in finite element implementation is a numerical artifice. In reality a crack does not grow cycle by cycle and each cycle in a

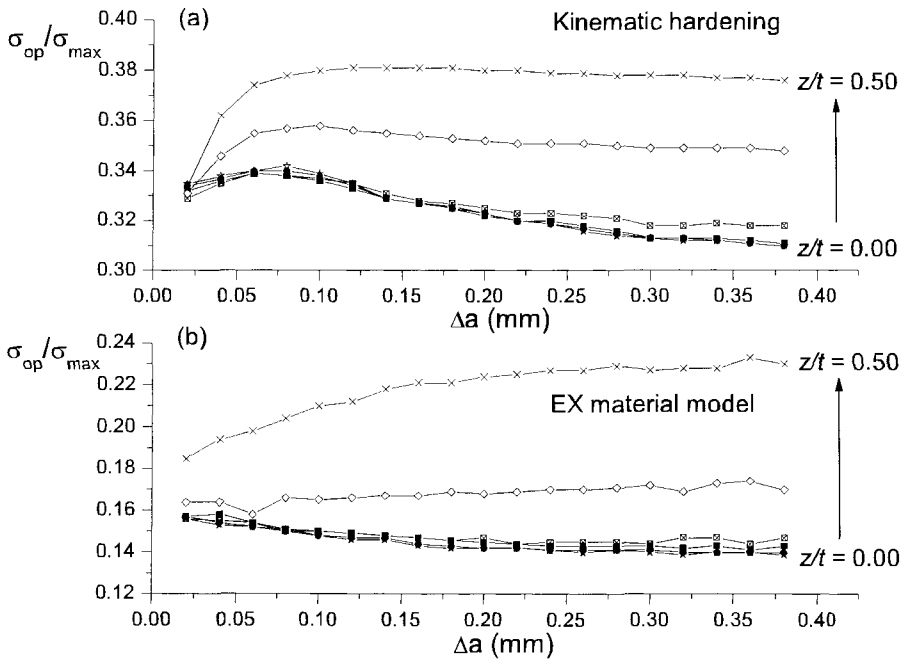


Figure 2.11: Crack opening level profiles through the thickness
*a) Kinematic hardening model, and b) Ellyin-Xia model (EX).*

finite element loading process may represent hundreds or thousands of cycles. Thus, discuss of the crack growth rate and its variation is purely interpretative. Crack opening profiles and crack opening stress levels are the main predictive parameters.

It should be noted that as shown in Figure 2.10, Plane stress stress analyses give results with similar trends to that obtained at the free surface and plane strain results to that at the mid-plane.

## 2.4 Kinematic hardening vs. Ellyin-Xia material model

### 2.4.1 *Crack opening stresses*

Normalized crack opening values $\sigma_{op}/\sigma_{max}$ are shown in Figure 2.11 for both material models employed. Both models show the expected tunnelling trend of crack growth as discussed earlier with opening occurring first at the interior surface $z/t = 0.00$ then outwards to the exterior surface $z/t = 0.50$. Although both models capture

the Bauschinger effect which has been shown to result in lower opening values, the plot shows a marked difference in the through thickness stress opening values between the two models. The Ellyin-Xia material model shows a trend of lower opening values with $\sigma_{op}/\sigma_{max}$ ratios of 0.14 at the interior ($z/t = 0.00$) to 0.23 at the free surface ($z/t = 0.50$), and is in good agreement with the experimental results obtained by Craig et al. [8] which varies from 0.10 to 0.30 as compared to 0.31 to 0.38 respectively for the kinematic hardening model. Thus the question may arise, why the difference?

Reasons for this are link to the following: Ellyin and Wu [13] have shown that classical models like the kinematic hardening do not accurately capture the unloading path of a cycle when compared to experimental results especially in the case of variable amplitude loading histories which shall be considered in the next chapter. Also the work of Meijer [32] on the uniaxial cyclic loading of aluminium showed that the numerical predictions of the kinematic hardening model in ANSYS do not agree well with experimental results, the results showed a marked difference in the hysteresis loops. Whereas the prediction of the Ellyin-Xia model was in good agreement with the experiment data.

In order to get some insight as to the reason for the difference in crack opening values, the stress and strain distributions along the crack plane will be examined below.

### 2.4.2 *Stress distribution*

Figures 2.12(a) and 2.12(b) show the normalize stress $\sigma_y/\sigma_0$ distribution along the crack plane for a typical load cycle after crack opening values have stabilized for the Ellyin-Xia model and the kinematic hardening model, respectively. The profiles show the stress distribution when the crack tip is at A for the point when the crack opens, point 1, and at maximum load, point 2. The crack is then advanced by an element length $\Delta a$ to B and unloaded to point 3, the minimum load.

Since these are typical stress distribution profiles, let us consider the stress profile for the minimum load point just before point 1 which would be similar to point

3. The profile shows that the kinematic hardening model (Fig. 2.12(b)) predicts a larger residual compressive zone around the crack tip with a maximum value of $-\sigma_0$ through the thickness as compared to the Ellyin-Xia model with maximum value of $-0.25\sigma_0$ in the interior and $-0.5\sigma_0$ at the exterior surface. Therefore for the crack to open, the stress required to overcome the residual compressive zone will be higher for the kinematic model then for the Ellyin-Xia model.

This can be seen in the profiles for point 1 when the crack opens. The profiles show higher opening values of $0.7\sigma_0$ at the interior to $0.3\sigma_0$ for the Ellyin-Xia model as compared to $0.6\sigma_0$ and $0.1\sigma_0$ respectively for the kinematic model. At first observation it would seem that the former should have higher opening values, however, it should be noted that the total stress change from compression (point 3), to tension (point 1) is greater in the kinematic hardening case: with values of $1.6\Delta\sigma_0$ at the interior to $1.1\Delta\sigma_0$ at the exterior for the kinematic hardening model as compared to $0.95\Delta\sigma_0$ to $0.55\Delta\sigma_0$ for the Ellyin-Xia model.

At the maximum applied load, point 2, the stress profiles prior to the crack advance are indicated by ②. Although the maximum stress values for the Ellyin-Xia model are higher than those of the kinematic model at B the next crack tip, the stress values drop faster and sharper in the former resulting in lower stress values away from the crack tip. Therefore this results in a smaller compressive zone at minimum load as seen in the stress distribution profile for point 3 in the Ellyin-Xia model as compared to the kinematic one. This trend is repeated for all the stabilized load cycles.

### 2.4.3 *Strain distribution*

Similar profiles for the strain component $\epsilon_y$ distribution along the crack plane are shown in Figure 2.13(a) and 2.13(b) for the Ellyin-Xia and kinematic models, respectively. The profiles for the Ellyin-Xia model shows a smaller total change in strain $\Delta\epsilon_y$ as compared to the kinematic model. This implies more hardening in the former which would result in lower opening stresses.

As mentioned above the classical models like the kinematic hardening model

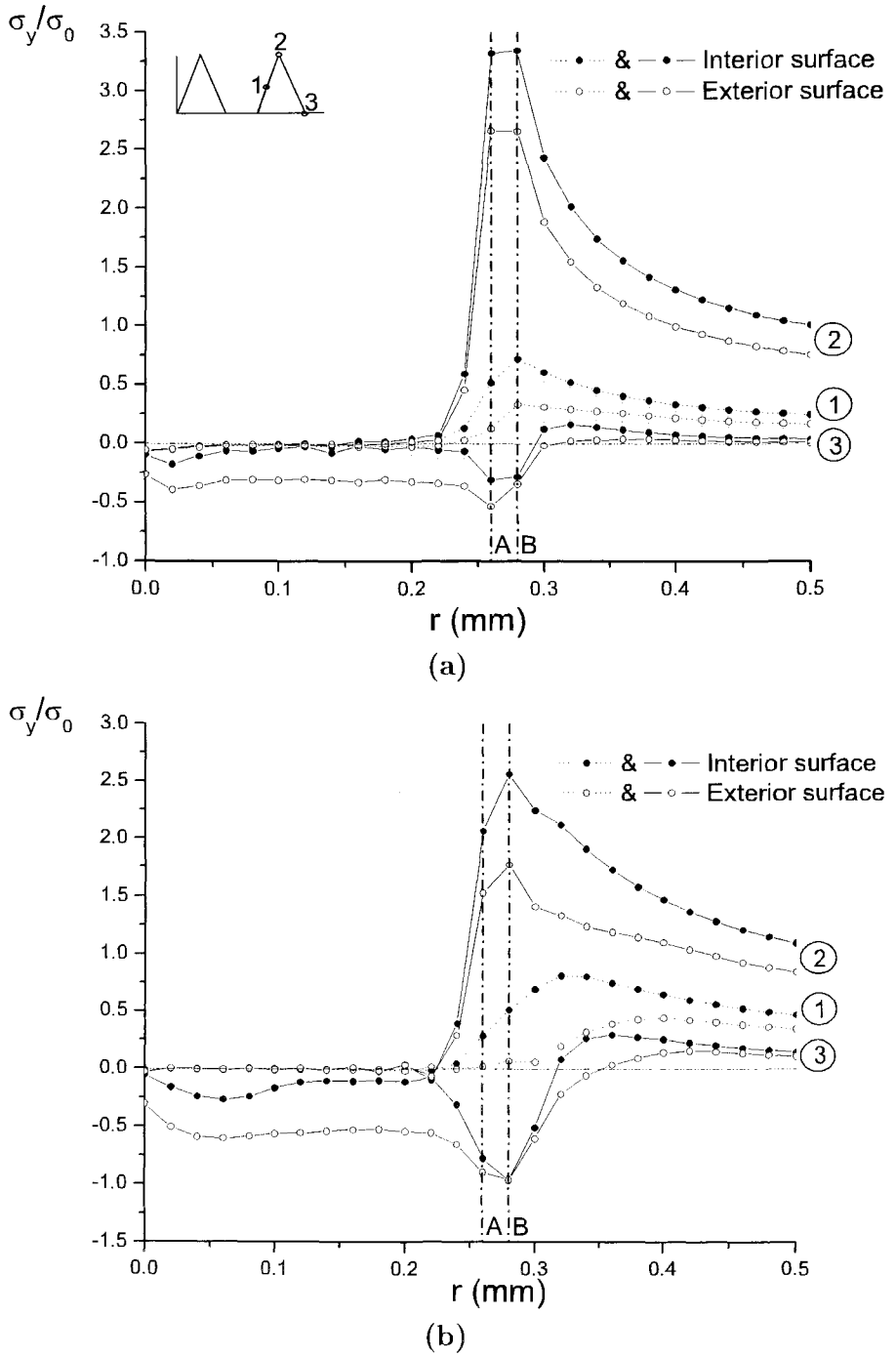


Figure 2.12: Stress distribution profiles

*a) Ellyin-Xia model, and b) Kinematic hardening model.*

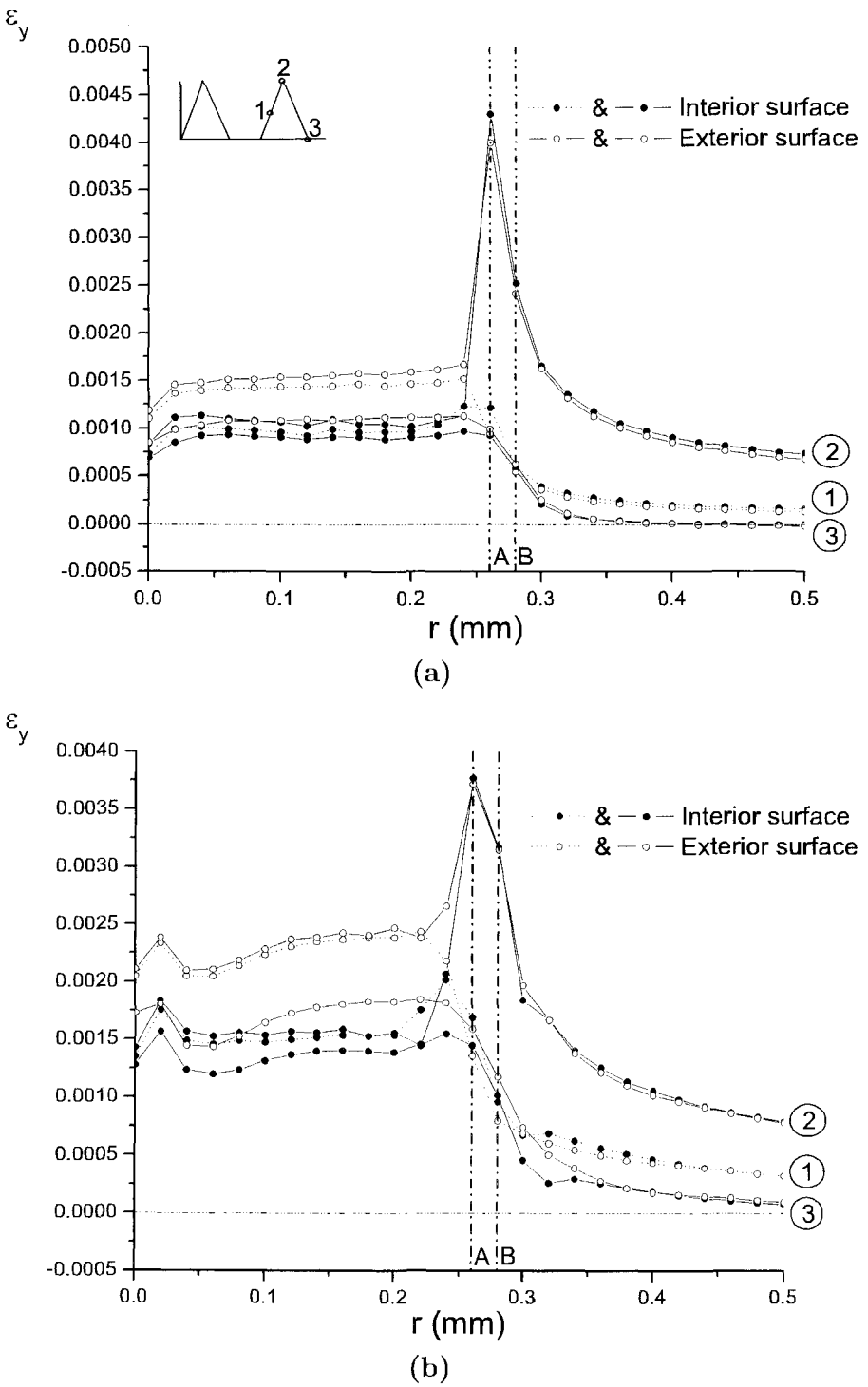


Figure 2.13: Strain distribution profiles

*a) Ellyin-Xia model, and b) Kinematic hardening model.*

do not accurately capture the unloading path and this is where and when the Bauschinger effect is defined. Thus a model that more accurately capture this path will capture this hardening effect better resulting in lower crack opening values.

# Bibliography


[1] *ANSYS User's Manual for Revision* 5.4. ANSYS Inc., Houston, volume iv theory edition, 1997.

[2] F. V. Antunes, L. F. P. Borrego, J. D. Costa, and J. M. Ferreira. A numerical study of fatigue crack closure induced by plasticity. *Fatigue & Fracture of Engineering Materials and Structures*, 27(9):825–825, 2004.

[3] R. S. Blandford, S. R. Daniewicz, and J. D. Skinner. Determination of the opening load for a growing fatigue crack: evaluation of experimental data reduction techniques and analytical models. *Fatigue & Fracture of Engineering Materials and Structures*, 25(1):17–26, 2002.

[4] R. G. Chermahini and A. F. Blom. Variation of crack-opening stresses in three-dimensions: finite thickness plate. *Theoretical and Applied Fracture Mechanics*, 15(3):267–276, 1991.

[5] R. G. Chermahini, K. N. Shivakumar, and J. C. Newman Jr. Three-dimensional finite-element simulation of fatigue crack growth and closure. In *Mechanics of Fatigue Crack Closure*, ASTM STP 982, pages 398–413, Philadelphia, 1988.

[6] R. G. Chermahini, K. N. Shivakumar, J. C. Newman Jr., and A. F. Blom. Three-dimensional aspects of plasticity-induced fatigue crack closure. *Engineering Fracture Mechanics*, 34:393–401, 1989.

[7] R. G. Chermahini, B. Palmberg, and A. F. Blom. Fatigue crack growth and closure behaviour of semicircular and semi-elliptical surface flaws. *International Journal of Fatigue*, 15(4):259–263, 1993.

[8] D. Craig, F. Ellyin, and Kujawski. The behaviour of small corner cracks in ferritic/pearlitic steel: experiments and analysis. *Fatigue & Fracture of Engineering Materials and Structures*, 18(7/8):861–873, 1995.

[9] D. S. Dawicke, A. F. Grandt, Jr., and J. C. Newman, Jr. Three-dimensional crack closure behavior. *Engineering Fracture Mechanics*, 36(1):111–121, 1990.

[10] J. D. Dougherty, J. Padovan, and T. S. Srivatsan. Fatigue crack propagation and closure behavior of modified 1070 steel: Finite element study. *Engineering Fracture Mechanics*, 56(2):189–212, 1997.

[11] W. Elber. The significance of fatigue crack closure. In *Damage Tolerance in Aircraft structure*, volume 486 of *ASTM STP*, pages 230–242, Philadelphia, 1971.

[12] F. Ellyin. *Fatigue Damage, Crack Growth and Life Prediction.* Chapman & Hall, London, 1997.

[13] F. Ellyin and J. Wu. Elastic-plastic analysis of a stationary crack under cyclic loading and effect of overload. *International Journal of Fracture*, 56:189–208, 1992.

[14] F. Ellyin and Z. Xia. A rate-independent constitutive model for transient non-proportional loading. *J. Mech. Phys. Solids*, 37(1):71–91, 1989.

[15] F. Ellyin, Z. Xia, and J. Wu. A new elastic-plastic constitutive model inserted into the user-supplied material model of ADINA. *Computers and Structures*, 56:189–208, 1992.

[16] Wu J. *Nonlinear Analyses of Cracked Bodies.* PhD thesis, University of Alberta, Edmonton, Alberta, 1995.

[17] R. C. McClung. Finite element analysis of fatigue crack closure: a historical and critical review. In *Fatigue '99: Proceedings of the seventh international fatigue congress*, volume 1, pages 495–502, Beijing, P. R. China, 8-12 June 1999.

[18] R. C. McClung. Finite element perspectives on the mechanics of fatigue crack closure. In *Fatigue '96: Proceedings of the seventh international fatigue congress*, volume 1, pages 345–356, Berlin, Germany, 6-10 May 1996.

[19] R. C. McClung and H. Sheitolgu. On the finite element analysis of fatigue crack closure - 1.Basic modelling issues. *Engineering Fracture Mechanics*, 33 (2):237–252, 1989.

[20] R. C. McClung and H. Sheitolgu. On the finite element analysis of fatigue crack closure - 2.Numerical results. *Engineering Fracture Mechanics*, 33(2):253–272, 1989.

[21] J. C. Newman Jr. Advances in finite-element modeling of fatigue-crack growth and fracture. In *Fatigue '02: Proceedings of the eight international fatigue congress*, pages 55–70, Stocknolm, Sweden, 3-7 June 2002.

[22] S. Pommier and Ph. Bompard. Bauschinger effect of alloys and plasticity-induced crack closure: a finite element analysis. *Fatigue & Fracture of Engineering Materials and Structures*, 23:129–139, 2000.

[23] W. T. Riddell, R. S. Piascik, M. A. Sutton, W. Zhao, S. R. McNeill, and J. D. Helm. Determining fatigue crack opening loads from near-crack-tip displacements measurements. In *Advances in Fatigue crack Closure Measurement and Analysis*, volume 2 of *ASTM STP 1343*, pages 157–174, Philadelphia, 1999.

[24] S. Roychowdhury and R. H. Dodds. Three-dimensional effects on fatigue crack closure in the small-scale yielding regime - a finite element study. *Fatigue & Fracture of Engineering Materials and Structures*, 26:663–673, 2003.

[25] S. Roychowdhury and R. H. Dodds Jr. A numerical investigation of 3-d small-scale yielding fatigue crack growth. *Engineering Fracture Mechanics*, 70(17): 2363–2383, 2003.

[26] J. D. Skinner. Finite element predictions of plasticity-induced fatigue crack closure in three-dimensional crack geometries. Master's thesis, Mississippi State University, Mississippi, 2001.

[27] J. D. Skinner and S. R. Daniewicz. Simulation of plasticity-induced fatigue crack closure in part-through crack geometries using finite element analysis. *Engineering Fracture Mechanics*, 69(1):1–11, 2002.

[28] K. Solanki, S. R. Daniewicz, and J. C. Newman Jr. Finite element modeling of plasticity-induced crack closure with emphasis on geometry and mesh refinement effects. *Engineering Fracture Mechanics*, 70(12):1475–1489, 2003.

[29] K. Solanki, S. R. Daneiwicz, and J. C. Newman Jr. Finite element analysis of plasticity-induced fatigue crack closure: an overview. *Engineering Fracture Mechanics*, 71(2):149–171, 2004.

[30] K. N. Solanki. Two- and three-dimensional finite element analysis of plasticity-induced crack closure - a comprehensive parametric study. Master's thesis, Mississippi State University, Mississippi, 2002.

[31] J. Wu and F. Ellyin. A study of fatigue crack closure by elastic-plastic finite element analysis for constant-amplitude loading. *International Journal of Fracture*, 82(1):43 – 65, 1996.

[32] Ellyin F. Xia Z. and Meijer G. Mechanical behavior of $Al_2O_3$-particle-reinforced 6061 aluminum alloy under uniaxial and multiaxial cyclic loading. *Composites Science and Technology*, 57(2):237–248, 1997.

[33] J. Z. Zhang and P. Bowen. On the finite element simulation of three-dimensional semi-circular fatigue crack growth and closure. *Engineering Fracture Mechanics*, 60(3):341–360, 1998.

[34] J. Z. Zhang, M. D. Halliday, P. Bowen, and P. Poole. Three dimensional elastic-plastic finite element modelling of small fatigue crack growth under a single tensile overload. *Engineering Fracture Mechanics*, 63(3):229–251, 1999.

# Chapter 3

# 3D Modelling of Plasticity Induced Fatigue Crack Closure: variable amplitude loading

## 3.1 Introduction

In practice many engineering structures are subject to variable amplitude loading histories rather than just a case of constant amplitude loading, with increasing $K$, decreasing $K$ or random loading. These types of loading histories influence the manner in which cracks would propagate if and when present in such structures. This chapter deals with the simplest of these histories which is an extension of the constant amplitude loading case already considered in the preceding chapter i.e.: the application of a single tensile or compressive overload during a load cycle.

Skorupa [25] in his review of the empirical trends indicated that experimental trends for the application of a single tensile overload are such that a crack growth retardation phenomena with some cases showing an initial acceleration in growth before the retardation. While the application of a compressive overload (underload) shows trends that vary from post underload crack growth acceleration to cases where the underload induces crack growth retardation. Various mechanisms have been identified to govern these growth effects: wake plasticity behind the crack tip, strain hardening response of the material, compressive residual stresses ahead of the crack

tip, fracture surface asperity contact, crack tip blunting and crack branching.

Of interest in this study are the mechanisms which can be captured by modelling the plasticity-induced crack closure process. As with chapter two, only a few of the 3-D works have considered these variable amplitude load histories, and those that do employ either the elastic-perfectly plastic or isotropic hardening models which as discussed in the foregoing chapter have limitations in describing the deformation behaviour of metals, particularly under cyclic loading. The objective of this work is to employ a material model that would accurately capture the effects of these influences on the plasticity-induced crack closure PICC process.

## 3.2 State of the Art Review

The rate of fatigue crack growth in structures subject to variable amplitude loading histories is strongly influenced by load interaction effects resulting in transient behaviour of the rate of fatigue crack growth. The transient behaviour may be an acceleration and/or retardation of the crack growth rate leading to an increase or decrease in the service life of the structure respectively. Various researchers have attributed the transient phenomena to mechanisms which contribute to the load interaction effects [1–7, 10, 11, 16–22, 25–29, 32, 33]:

- crack tip blunting,
- residual compressive stresses (RCS) ahead of the crack tip,
- plasticity-induced crack closure,
- strain hardening ahead of the crack tip,
- crack branching,
- fracture surface asperity contact, and
- reversed yielding.

Although there is agreement amongst researchers that a particular mechanism may not be solely responsible for the observed transient behaviour, there is no consensus as to which of these mechanisms is primarily responsible for the observed phenomena because the micromechanisms are not completely understood [2, 26, 33]. For this work, we shall focus on three mechanisms which can be captured by the present 3-D FE model: the residual compressive stresses ahead of the crack tip, the PICC process, and strain hardening ahead of the crack tip. The first two of these have been highly debated to be the dominant mechanism responsible for variable amplitude transients, but in this work the plasticity-induced crack closure phenomenon is seen as "the resulting effect" of the residual compressive stresses ahead of the crack tip and may be seen as "the cause". While the strain hardening mechanism although not the primary mechanism couples with either of these mechanisms. Also this work considers simple variable load histories: the effect of a single overload (OL)/underload (UL). The following gives a description of the mechanisms:

**Residual stresses**: The application of a single overload causes large residual plastic deformation which induces large residual compressive stresses (RCS) at and ahead of the crack tip upon unloading. Therefore when the loading returns to pre-overload values, the RCS generated as the crack propagates though smaller than the overload-RCS is enclosed within the overload-RCS zone. Therefore the load required to open the crack is higher than that needed for pre-overload loading conditions due to higher compressive stresses. This results in a retardation effect i.e $\Delta K_{eff,\,postOL} < \Delta K_{eff,\,beforeOL}$. Figure 3.1(a) shows a schematic of the growth retardation process. This mechanism implies that the post-overload retardation effect would be immediate with no transient acceleration [2, 19, 26], except for an instantaneous crack growth acceleration upon overload application.

For the case of the effect of a single underload, residual tensile stresses (RTS)

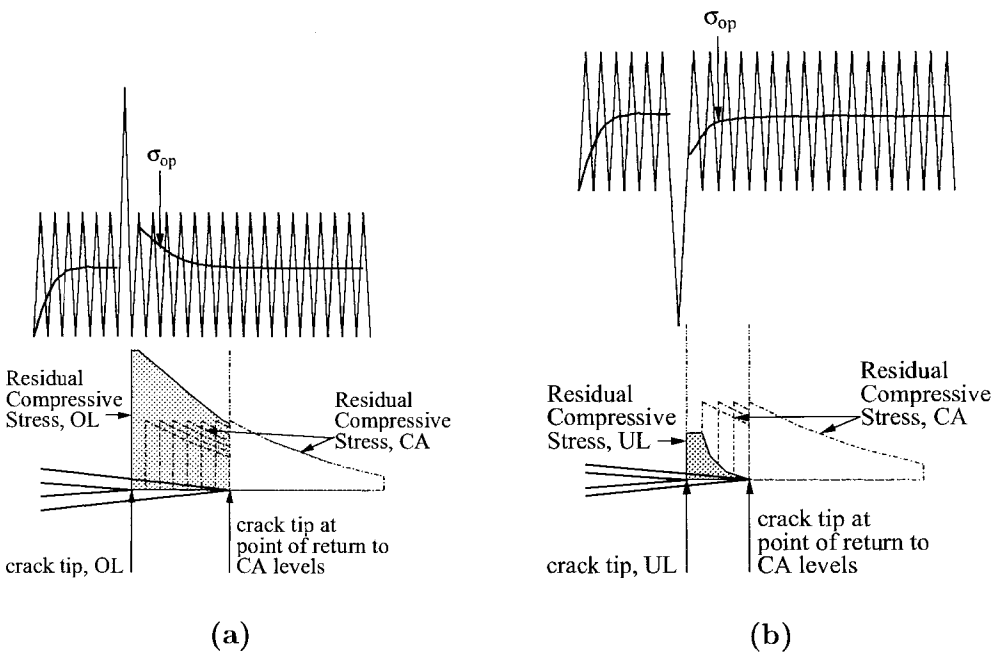


Figure 3.1: Schematic of the mechanism of residual stresses

*a) The overload generates a zone of residual compressive stresses (RCS), and b) The underload generates a zone of residual tensile stresses (RTS).*

are induced at and ahead of the crack tip by the residual plastic deformation due to compressive yielding as crack surface contact during the underload cycle. The RTS would reduce the magnitude of the effective compressive zone, therefore the load required to open the crack will be reduced as compared to pre-underload values resulting in an acceleration of the crack growth rate [26] i.e $\Delta K_{eff,UL} > \Delta K_{eff,before\,UL}$. Figure 3.1(b) shows a schematic of how growth acceleration occurs.

**Plasticity Induced Crack Closure (PICC)**: The PICC process first identified by Elber [8] has also been used to describe the transients associated with variable amplitude load histories. Unlike the mechanism of compressive residual stresses, the PICC mechanism accounts for an initial acceleration due to large tensile plastic deformation resulting from the applied overload

which reduces or eliminates the crack closure effect along the crack surfaces. Therefore $\Delta K_{eff,OL} > \Delta K_{eff,before\,OL}$, the driving force for crack growth is increased; thus, an acceleration in growth rate occurs. However, it should also be noted that the acceleration may be cancelled or reduced by ductile crack growth increment (DCGI) induced closure resulting from the applied overload. The DCGI induced closure then counters the reduction in closure caused by the overload tensile plastic deformation [11]. As the crack grows, it enters the overload plastic zone which causes the magnitude of the effective closure stresses to become higher than pre-overload values, thus the crack growth rate undergoes retardation.

As in the case of the residual compressive stress mechanism, compressive yielding due to the underload induces a residual tensile stress which reduces the magnitude of the closure effect of the plastic wake zone as the crack enters the residual tensile stress. Therefore the load required to open the crack is reduced leading to transient acceleration.

**Strain hardening**: As a plastic zone is formed during the loading path of a cycle, an associated plastic strain gradient develops ahead of the crack tip. In the event of an overload, the plastic strain gradient is larger then pre-overload values and this introduces humps of stretched material ahead of the crack tip. Upon unloading this region of stretched material within the plastic zone resists the elastic recovery of the material enclosing the plastic zone, thus creating a hardened wedge ahead of the crack tip. Figure 3.2 shows a schematic of the process. This hardened region ahead of the crack tip leads to retardation of the fatigue growth rate [2, 26]. A similar process occurs for an underload, the plastic strain gradient is largely reduced by the underload as compared to pre-underload values. This leads to a 'softened' zone, the crack tip is then resharpen which results in transient acceleration.

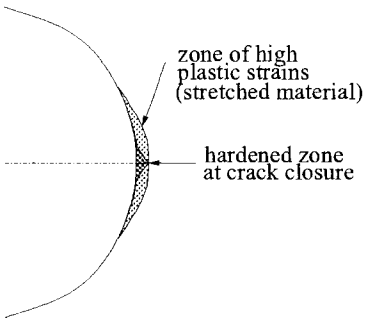


Figure 3.2: Strain hardening effect

It is well documented that the application of a single overload or block(s) of overloads results in a retardation effect. However, a number of researchers have observed transient acceleration before the retardation effect [1, 19, 20, 33], while other have only observed the retardation effect [25, 28]. It is the opinion of the author that there must occur an initial instantaneous acceleration during the overload cycle, see Fig. 3.3: the driving force for crack growth, $\Delta K_{eff}$, is such that for the overload cycle $\Delta K_{eff,\,OL} > \Delta K_{eff,\,before\,OL}$ which implies that the overload crack growth driving force is greater than the pre-overload value, thus the initial acceleration. And after the overload cycle, $\Delta K_{eff,\,before\,OL} > \Delta K_{eff,\,postOL}$, implying a retardation

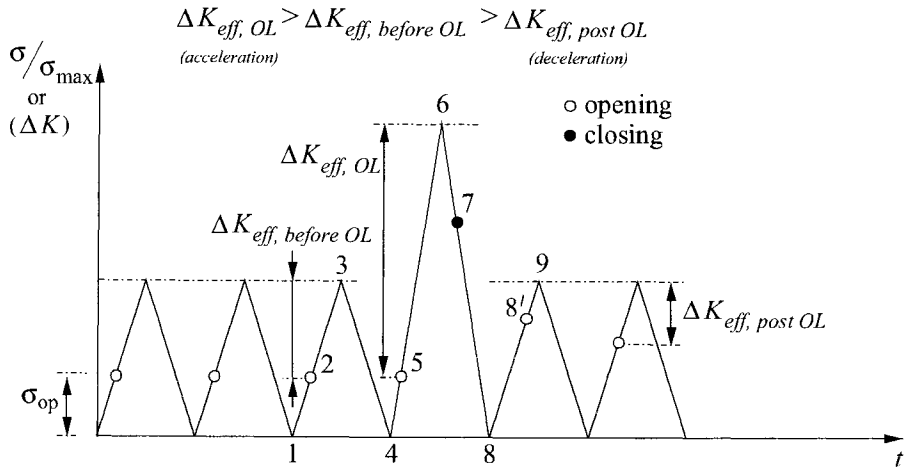


Figure 3.3: Schematic of the effect of driving force $\Delta K_{eff}$., on the acceleration and retardation of the fatigue crack growth rate for a tensile overload

effect. Note that the for the FE analyses which measures opening stresses, the initial acceleration would not be captured.

Also although compressive overloads have been documented to result in fatigue crack growth acceleration of the crack growth rate, the work of Buscher-mohler et al. [3] showed that compressive overload effects resulted in a retardation of the fatigue crack growth rate rather than acceleration while Carlson and Kardomateas [4] showed a transient retardation after an initial acceleration. These

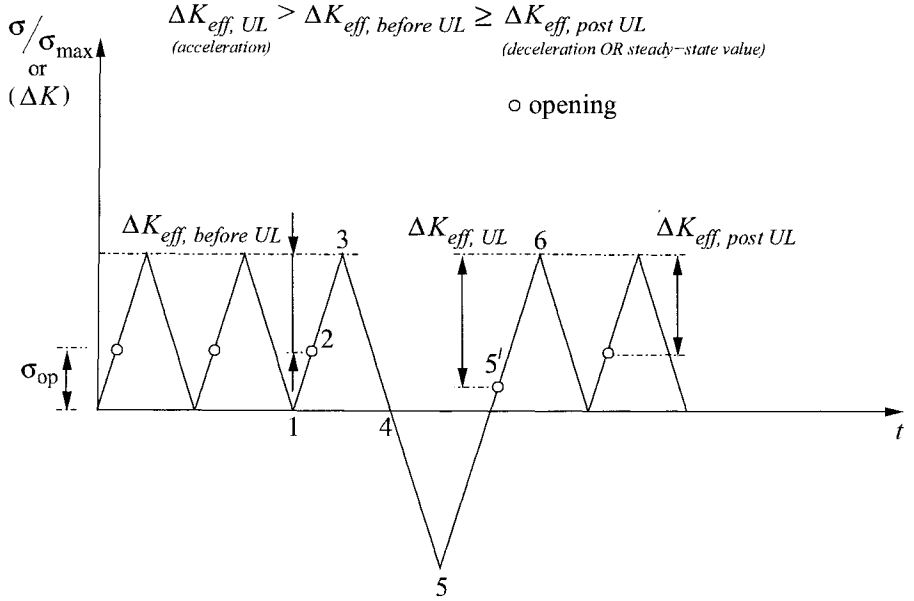


Figure 3.4: Schematic of the effect of driving force $\Delta K_{eff.}$, on the acceleration and retardation of the fatigue crack growth rate for a compressive overload (*underload*)

works demonstrated that the mechanisms discussed above are not responsible for this phenomenon but rather this transient retardation is due to other mechanisms. Similar to the case of the tensile overload, it is the opinion of the author that there must occur an initial instantaneous acceleration during the underload cycle, provided the compressive underload is large enough. Figure 3.4 shows schematically the driving force for crack growth, $\Delta K_{eff}$, is such that for the underload cycle $\Delta K_{eff,UL} > \Delta K_{eff,\,before\,UL}$ which implies that the underload crack growth driving force is greater than the pre underload value, thus an acceleration. And after the

overload cycle, $\Delta K_{eff,\,before\,UL} \geq \Delta K_{eff,\,post\,UL}$, which implies return to pre underload value or a retardation effect.

McEvily and Ishihara [19] demonstrated that the crack retardation effect is strongly related to the plane-stress surface layers. The work showed that if the surfaces were machined away after the application of an overload before loading of the specimen continues at pre-overload values, the retardation effect is largely reduced as compared to if the surfaces were intact. This implies that the crack still retains it tunnelling shape during the retardation effect. Figure 3.5 shows schematically a typical post-single tensile overload behaviour observed experimentally, with the following notable stages for a thin specimen:

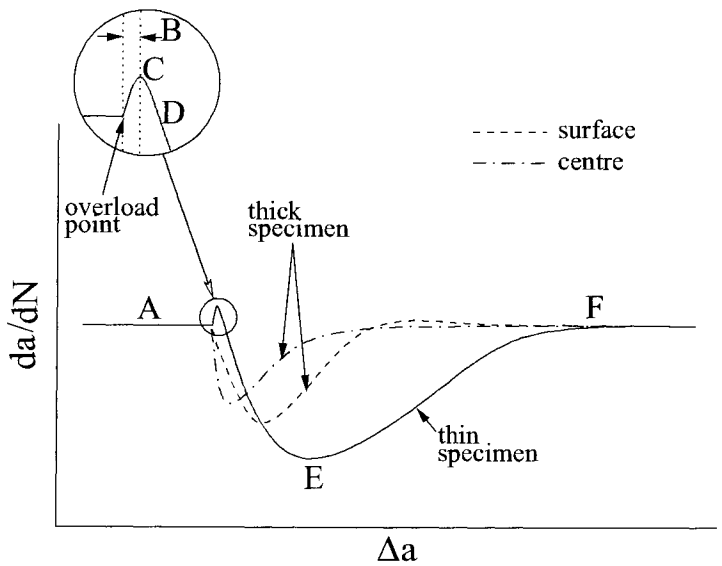


Figure 3.5: Schematic of the thickness effect on crack growth after the application of a tensile overload

*Typical crack growth rate showing delayed retardation following a tensile overload for: i) a thin specimen* [1, 25], *and ii) a thick specimen* [25]

1. region of stabilized crack growth before application of tensile overload - A

2. region of crack growth during the overload cycle - B - crack growth acceleration

3. region of crack growth deceleration - CD, but with a higher growth rate than the base load rate

4. region of crack growth retardation - DE

5. region of steady return to initial stabilized crack growth values - EF

and for a thick specimen, the last two regions are the dominant zones [25].

### 3.2.1 *Statement of the Problem*

The problem to be considered in this chapter is an extension of that studied in chapter two i.e. a constant amplitude loading onto which a single spike overload or an underload is superimposed during the cyclic loading of the structure, see Fig. 3.5. Of the works conducted on the 3-D modelling of the PICC process only a very few consider the PICC process under variable amplitude loading conditions. In these investigations they either consider the use of an elastic-perfectly plastic material model [5, 27] or an isotropic hardening material model [33] which do not consider the Bauschinger effect in cyclic plasticity. There are no known 3-D studies of the application of an underload.

As discussed in the pervious chapter, the choice of constitutive model employed for the analyses of the PICC is of major importance in obtaining good solution to the problem. This is especially the case when considering variable amplitude loading histories. Ellyin and Wu [10] have shown that the predicted response of a variable strain history when employing the classical isotropic and kinematic hardening models do not adequately capture the experimental response especially during the unloading process. This is not the case with the Ellyin-Xia constitutive model given in chapter one which showed a very good fit to the experimental data [9, 12, 13, 31].

Another factor of interest that influences the PICC process is the Bauschinger effect. Pommier and Bompard [21] have shown in a 2-D FE study that the crack opening levels after the application of an overload or an underload is highly depen-

dent on the material behaviour employed and that the Bauschinger effect plays a major role in the evolution of the crack opening levels. Figure 3.6 shows that after unloading the compressive residual stresses adjacent to the crack tip are Bauschinger effect dependent: the stresses are high if the effect is low or small if the effect is strong. Roychowdhury and Dodds, Jr. [23, 24] have also shown in 3-D FE constant-

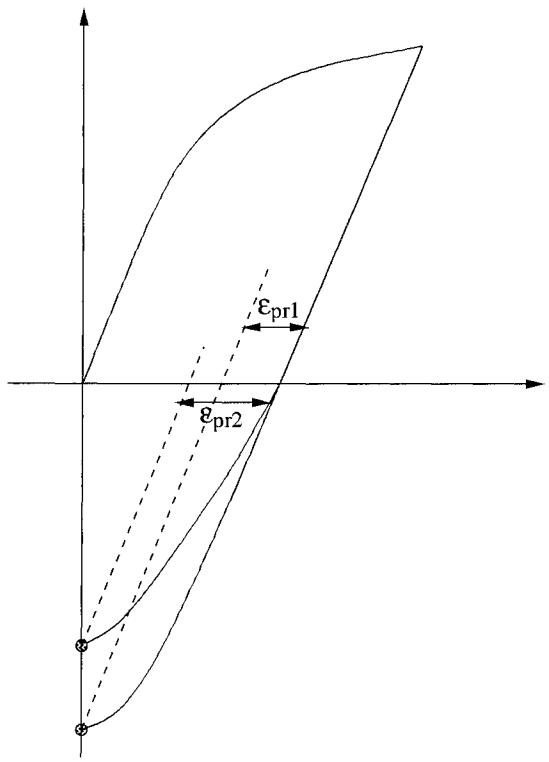


Figure 3.6: Schematic of the dependence of residual stresses on the Bauschinger effect

*Strong Bauschinger effect - small stresses, while weak Bauschinger effect - high stresses, adopted from Ref.* [21]

amplitude loading studies that analyses conducted using models that exhibit the Bauschinger effect show reduced crack opening levels in cyclic plasticity.

Therefore it is important to employ a model that captures the effects of cyclic plasticity more accurately especially during the unloading path of load cycles as this is where the Bauschinger effect is exhibited and the classical models fail to

properly fit experimental data. In this chapter, we consider the use of the Ellyin-Xia constitutive relation introduced in chapter two which can be used to model both proportional and non-proportional loadings conditions [9, 31], while taking into consideration the effects of cyclic plasticity. The material model was implemented into the ANSYS finite element code using the User Programmable Features routine USERMAT (see Appendix A for the verification of the routine). This material model is used to solve the variable crack problem subject to the following loading conditions: the effect of an single overload, and the effect of an single underload. The kinematic hardening model provided in the ANSYS material model library was also employed to solve the same crack problem, and the results for both models are compared.

## 3.3 Finite Element Model

The 3-D model employed for this study is similar to that used in the preceding chapter, therefore these analyses were also performed using a modified form of the APDL batch script used in chapter two. A summary of the computation hypotheses is as follows:

- **Mesh generation and definition of the material model**: The model was assumed to have ASTM 516 Gr. 70 steel material properties given in Table 3.1 with the following geometrical configuration: height, $H$ = 80mm; width, $W$ = 80mm; thickness, $t$ = 8mm and an initial crack length, $2a$ =8mm. One-

Table 3.1: Material properties

| **Property** | **Value** |
|---|---|
| Young's modulus, $E$ (GPa) | 204GPa |
| Poisson's ratio, $\nu$ | 0.30 |
| Yield stress, $\sigma_o$ (MPa) | 230MPa |

eighth of the geometry was modelled due to symmetry about the $xy$, $yz$ and

$zx$ planes using a 3-D 8- nodes structural solid, SOLID45 for the kinematic hardening model, and a 3-D 18x family element, SOLID185 for the Ellyin-Xia model. The mesh with smallest element length $\Delta a = 0.02$mm, 4129 elements and 5798 nodes which has been shown to satisfy convergence in chapter two was employed for these analyses with five layers through the half thickness of the geometry, i.e $0.25t$, $0.15t$, $0.05t$, $0.03t$ and $0.02t$ (with the smallest layer located on the free surface) to allow the capture of the rapid changing state of stress across the thickness of the geometry.

- **Application of initial boundary conditions**: The PICC crack problem is a variable boundary value problem because as the crack is propagated the boundary condition change. Therefore taking advantage of the three planes of symmetry; the following initial boundary conditions were applied to the model:

$$\begin{aligned} u_x(0,y,z) = 0 \quad &\rightarrow \quad 0 \leq y \leq H/2; \quad 0 \leq z \leq t/2 \\ u_y(x,0,z) = 0 \quad &\rightarrow \quad a \leq x \leq W/2; \quad 0 \leq z \leq t/2 \\ u_z(x,y,0) = 0 \quad &\rightarrow \quad 0 \leq x \leq W/2; \quad 0 \leq y \leq H/2 \end{aligned}$$

The model was then loaded through 20 cycles with a maximum stress, $\sigma_{max} = 0.3\sigma_0$ and an overload ($\sigma_{old} = 0.6\sigma_0$)/underload($\sigma_{uld} = -0.3\sigma_0$) was applied on the 5th cycle.

- **Loading path and determination of crack opening values**: The model was loaded incrementally using small load steps to allow the accurate capture of the crack opening values along the thickness of the model which are obtained by monitoring the reaction forces at the crack tip nodes. When the reaction force is in tension the crack is deemed to be fully open [30].

- **Crack advance**: The crack is advanced at a top of the load cycle i.e at the maximum load.

- **Unloading path and crack surface contact**: During the unloading path, the model was unloaded using small load steps to permit the proper simulation and capture of the crack surface contact process. The displacement values of the crack surface nodes were monitored, and once a surface node had a negative displacement the node was constrained in the crack surface plane. At the minimum load before the reloading, the constrains on the surface nodes are removed before reloading on the next cycle.

## 3.4 Effect of a single overload

The crack opening displacement profile at maximum load for the 5th cycle (overload cycle) and the 14th cycle (9 cycles after the application of the overload) are shown in Figures 3.7(a) and (b) for the Ellyin-Xia and kinematic hardening models respectively. The plots show that significant crack tip blunting occurs for both models during the overload cycle (5th cycle) as compared to constant amplitude (CA) cyclic loading displacements. It can be seen that after the overload the crack behaves as a notch (see the profiles for the 14th cycle - overload case) which results in an acceleration of the fatigue crack growth rate. This may be attributed to the fact that during the overload cycle, there is sufficient removal of pre-overload plasticity-induced crack closure resulting in blunting of the crack tip, therefore less load is required to separate the fracture surfaces, thus an increase of crack growth rate during the overload cycle [14, 15, 29].

Figures 3.8(a) and (b) show the normalized crack opening stress $\sigma_{op}/\sigma_{max}$ for the Ellyin-Xia and kinematic hardening models respectively. The opening profile of the analysis employing the Ellyin-Xia model follows the expected trend for thick specimen [26] shown in Fig. 3.5 in which the crack opening stress increases with a retardation effect and then declines gradually to pre-overload opening values (Note: these analyses measure the crack opening stresses, therefore the initial crack growth acceleration during the overload cycle is not captured, *see Fig. 3.3*). The model also

captures the relation between crack retardation effect and the plane-stress surface layers [19], showing that the effect is stronger at the near surface layers: the profile shows the retardation effect increases with $z/t$ from $0.00 \rightarrow 0.50$.

Although the analysis employing the kinematic hardening model also shows a retardation effect, its profile shows a different trend. After the retardation effect peaks, the values across the thickness remains near constant instead of declining to pre-overload values as expected. Also the associated relationship between retardation and plane-stress surface layers is not captured, as the opening profile shows that the retardation is smallest at the surface.

In order to get a better understanding of the observed trends, let us examine the stress and strain distributions.

### 3.4.1 *Stress and strain distributions*

The distribution of non-dimensional stress component normal to crack plane, $\sigma_y/\sigma_0$, is shown in Figures 3.9 for the Ellyin-Xia and kinematic hardening models, respectively. The stress distribution is shown for the interior surface as the general trend is similar through the thickness of the plate. The abscissa indicates the distance from the initial crack tip along its plane. In Fig. 3.9(a-i) and 3.9(b-i) the crack is at point A (after 4 cycles of growth) and point B (2 cycles after the overload), while for Fig. 3.9(a-ii) and 3.9(b-ii) the crack tip is at C (9 cycles after the overload). The plots show the distribution profiles at the point when the crack becomes open and at minimum load.

As expected during the application of the overload the crack opens at the same level as the base constant amplitude (CA) cyclic load, however, after the overload application, the residual stress patterns are different. For the Ellyin-Xia model, the profiles in Figure 3.9(a-i) show that after the application of the overload a large residual compressive stress zone is formed at the overload crack tip A and its wake which rapidly declines away from the front as compared to constant amplitude (CA)

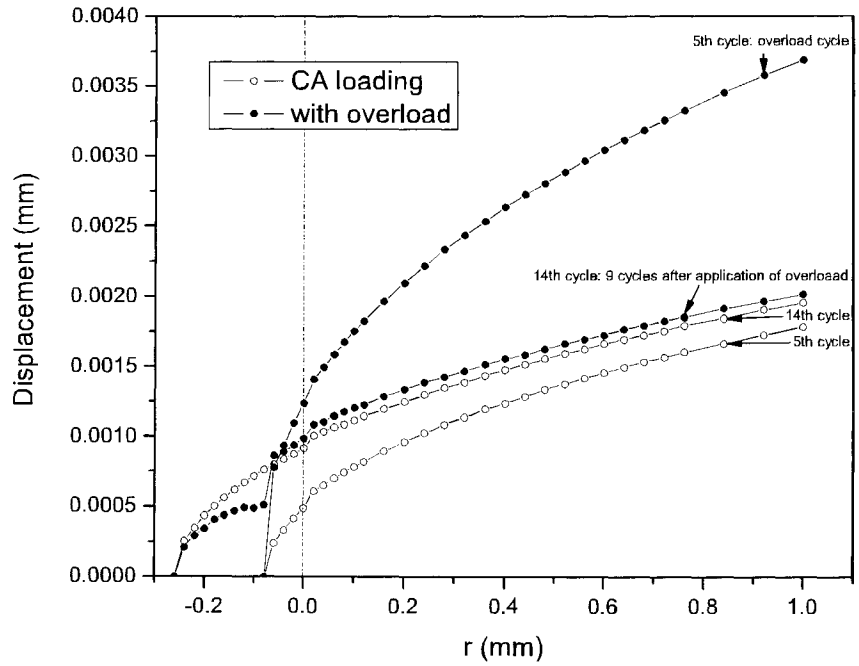


(a)

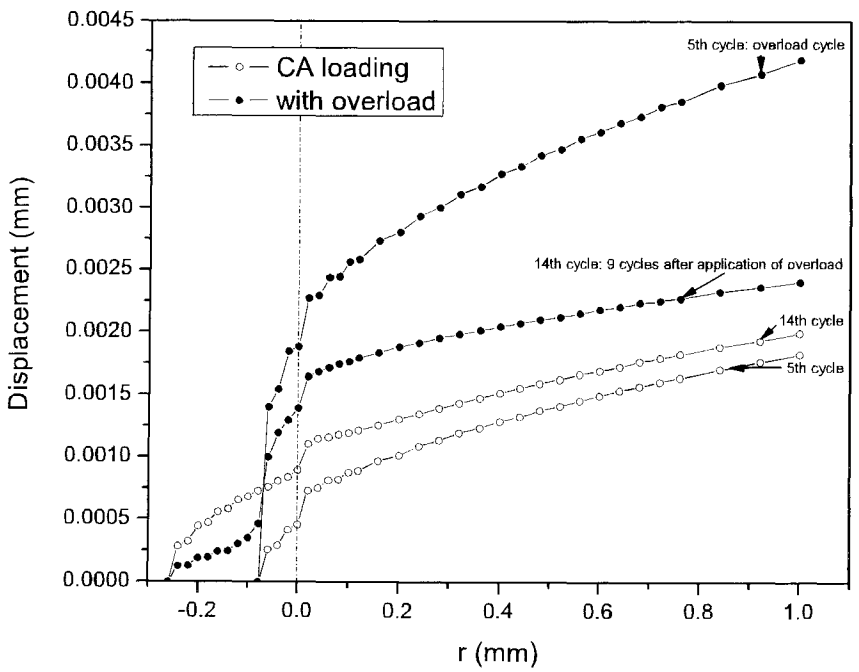


(b)

Figure 3.7: Displacement profiles for the 5th cycle (the overload cycle for OL), and the 14th cycle at maximum load.

*a) Ellyin-Xia model, and b) Kinematic hardening model.*

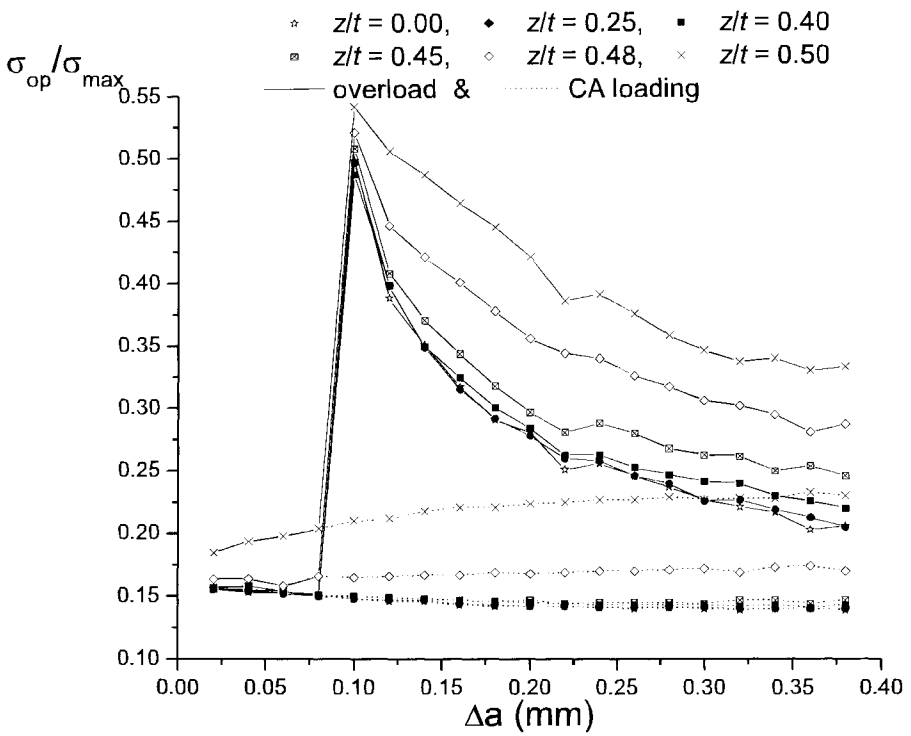


(a)

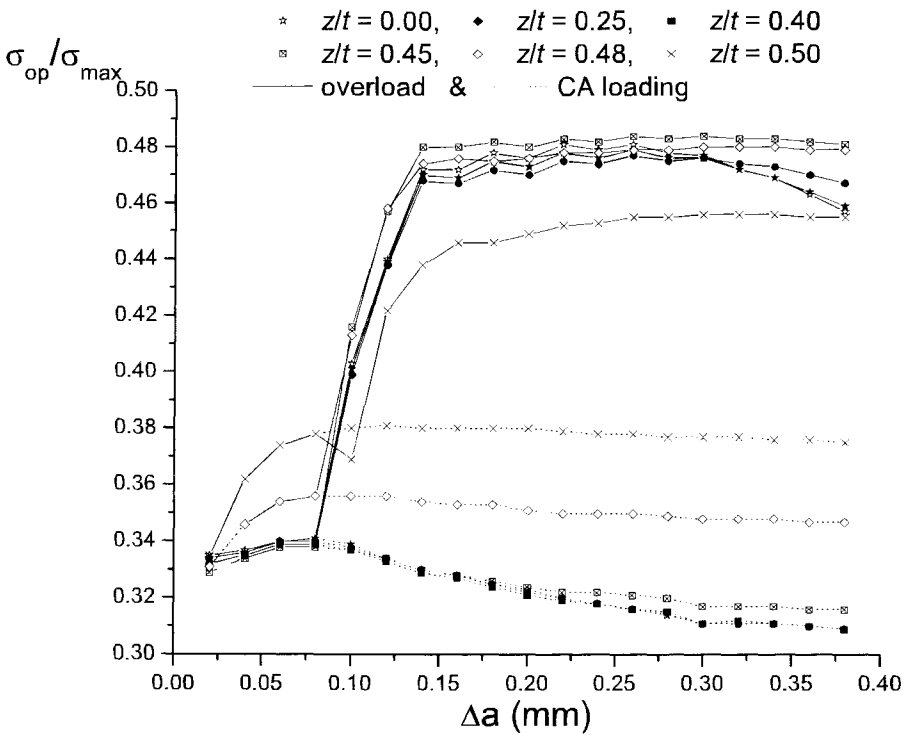


(b)

Figure 3.8: Crack opening stress profiles

*a) Ellyin-Xia model, and b) Kinematic hardening model.*

values. Also due to the application of the overload a large strain gradient develops at the crack tip, A, as seen in the strain profile shown in Figure 3.10(a-i). The high strain stretches the material adjacent to the overload crack tip and its wake which upon unloading creates a harden zone ahead of the crack tip (See Fig. 3.2). This coupled effect results in the retardation effect following the overload as seen in the crack opening stress profile, Figure 3.8(a)

At the minimum load 2 cycles after the overload at crack tip, B, the value of residual stresses have started to decline but the stress profile at crack opening are higher than the CA loading values, see Figure 3.9(a-i). And at 9 cycles after the overload shown in Figure 3.9(a-ii) the stress profiles indicate that the influence of the residual stresses at the overload point are no longer observable at the current crack tip, C, because the residual stresses at this point have returned to CA values, but the profile at crack opening remain higher than CA values. This trend implies that a higher global load must be attained to overcome the residual stresses therefore the driving force for crack propagation is reduced resulting in the retardation effect but with declining magnitude as seen in Figure 3.8(a). Although at the crack tips, B, 2 cycles and, C, 9 cycles after the application of the overload, the strain profile have returned to CA values as, see in Figure 3.10(a-i) and (a-ii). This trend implies that the strain hardening contributes at the start of the retardation effect but not significantly as the crack grows.

The profiles for the kinematic hardening model in Figure 3.9(b-i) show large compressive residual stresses at minimum load after the applied overload but with a very gradual decrease away from the overload crack tip and the absence of a large strain gradient at the crack tip, A, at the opening load as seen in the strain profile shown in Figure 3.10(b-i). This trend might explain why the kinematic model predicts near constant retardation opening values seen in Figure 3.9(b). Furthermore, the profile for the crack opening point at the crack tip, B, 2 cycles after the overload, show that the stresses ahead of the crack tip are still compressive. This trend can

be seen clearly for the profiles 9 cycles after the overload. At minimum load before loading on this cycle, the residual stresses at the current crack tip, C, are smaller than the CA values and the profile at the point of crack opening are compressive at the crack tip and of lower magnitude than CA values. Also the strain distribution profiles for the crack tip at B and C in Figure 3.10(b-i) and (b-ii) show a different trend with negative (compressive) strains. This should imply an acceleration effect because the effective global load required to open the crack should be smaller. Although the kinematic model captures the expected retardation effect, the stress profile obtained with this model cannot be used to explain the mechanisms involved.

## 3.5 Effect of a single underload

The effect of an underload on the normalized crack opening stress $\sigma_{op}/\sigma_{max}$ for the two models employed for this study are shown in Figure 3.11. The profile obtained employing the Ellyin-Xia model shows an initial acceleration followed by a brief retardation period before rapidly returning to near pre-underload values, see Figure 3.11(a). Although the general trend of transients after an underload have been observed to be an acceleration effect with retardation, the work of Buschermohler et al. [3] demonstrated experimentally that for the alloy 40CrMoV 4 7, no significant acceleration was noticed but a retardation was observed. And also Carlson and Kardomateas [4] showed in their work that transient retardation occurred after the acceleration upon return to pre-underload loading conditions. Although these works could not identify which mechanisms are responsible for this retardation effect, numerical analysis performed by Buschermohler et al. employing a PICC model showed that the PICC process was not responsible because only the acceleration could be captured.

Also the profile obtained while employing the kinematic hardening as seen in Figure 3.11(b) shows a similar trend with an initial acceleration followed by the

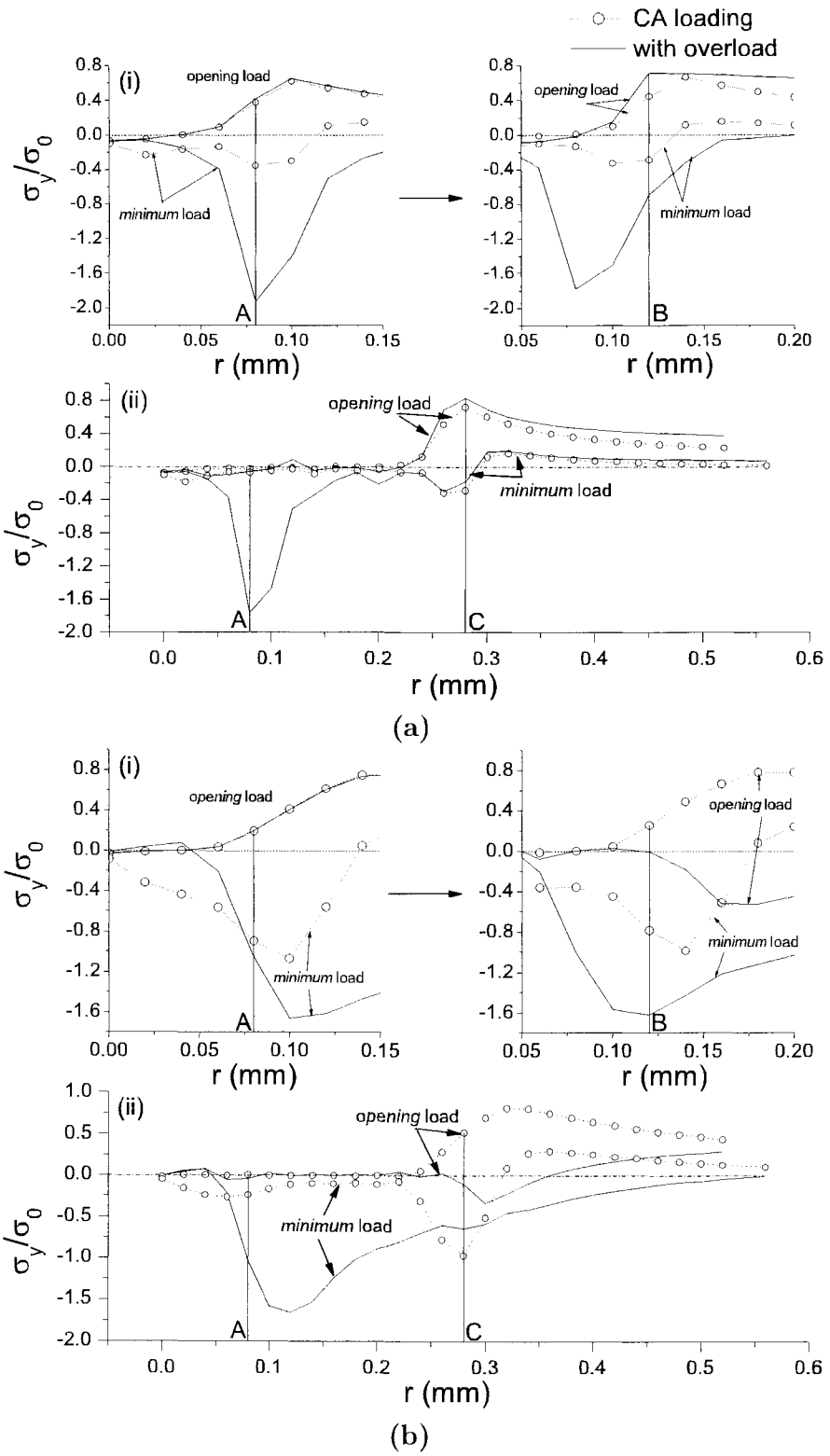


Figure 3.9: Distribution profiles of the stress component normal to the crack plane *a) Ellyin-Xia model, and b) Kinematic hardening model.*

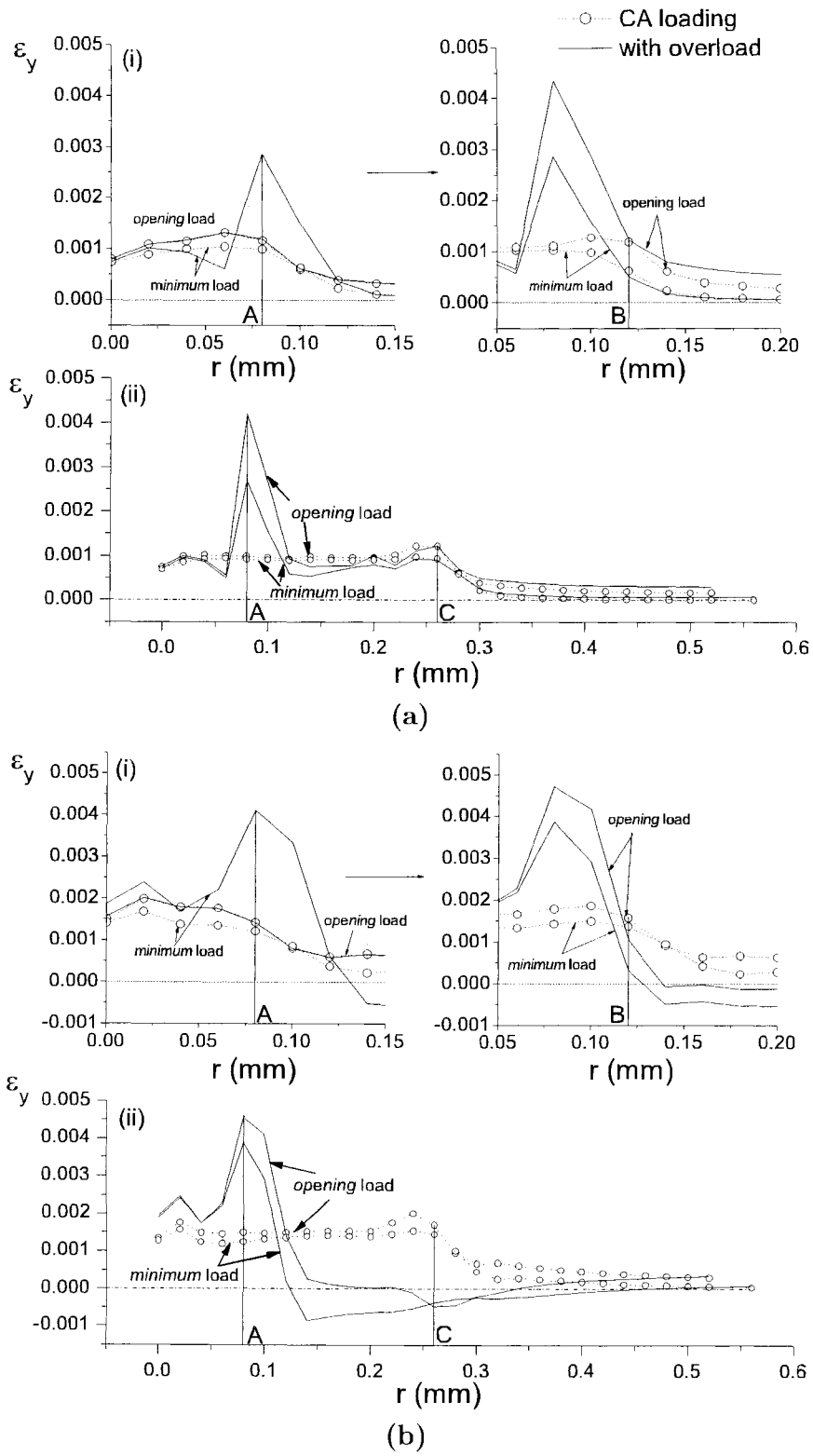


Figure 3.10: Distribution profiles of the strain component normal to the crack plane *a) Ellyin-Xia model, and b) Kinematic hardening model.*

retardation effect which occurs over a longer region of crack growth. The region over which the retardation effect occurs is similar to the near constant retardation trend observed in the case of an overload as shown in Figure 3.8(b). The stress and strain distribution profiles are considered next to get a better understanding of the trends observed.

### 3.5.1 *Stress and strain distributions*

Similar to the case of an overload, the $\sigma_y/\sigma_0$ and $\epsilon_y$ distributions for an underload are shown in Figures 3.12 and 3.13 for the two models employed in this study for the interior surface as the general trend is similar through the thickness of the plate. The plots show the distribution profiles at the point when the crack becomes open and at minimum load. Figures indicated by (a-i) and (b-i) show distribution profiles when the crack tip is at point A (after 4 cycles of growth) and point B (2 cycles after the underload) respectively. While those identified with (a-ii) and (b-ii) show the distribution profiles when the crack tip is at point C (9 cycles after the underload).

Figure 3.12(a-i) shows that for the Ellyin-Xia model, the underload introduces large compressive residual stresses at the crack tip A and in its wake and the compressive plastic deformation, see Figure 3.13(a-i. Both of these contribute to reduce the crack opening stress (Fig. 3.12(a-i)) resulting in the acceleration effect seen in Figure 3.11(a). The profiles in Figures 3.12(a-i) and (a-ii) 2 and 9 cycles after the underload, when the crack tip is at points, B and C respectively, show that the magnitude of the residual stresses generated by the underload is reduced as the crack propagates and the profiles then tends to those of the CA profiles as seen in Figure 3.11(a). The residual stresses and the strain hardening which occurs at the underload crack tip after the return to pre-underload loading as seen in Figures 3.12(a-i) and (a-ii) combine to result in the retardation effect as seen in Figure 3.11(a).

For the case of the kinematic hardening model, large residual stresses are intro-

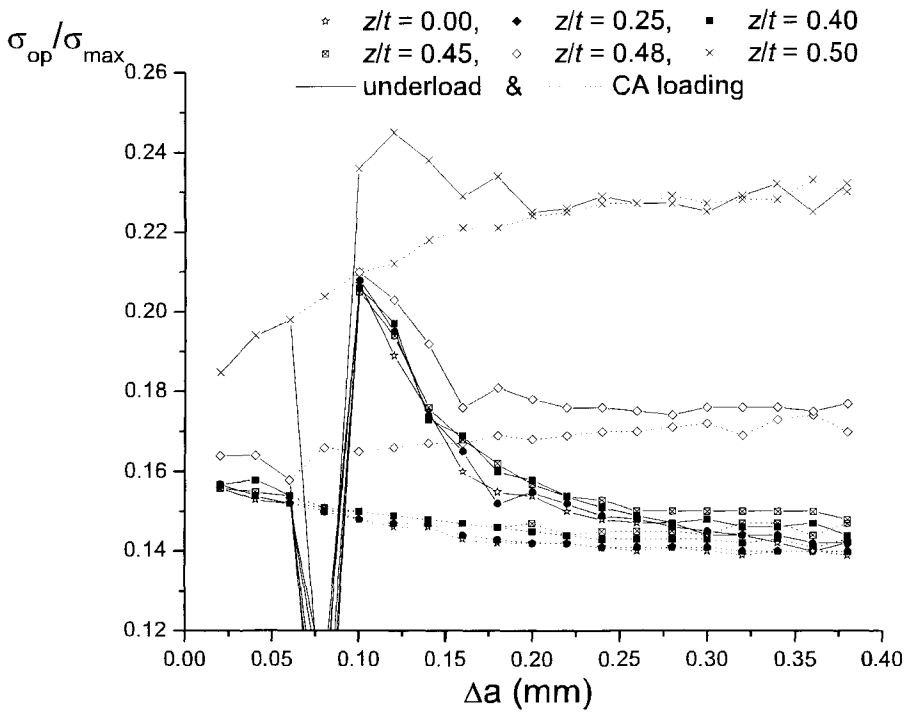


(a)

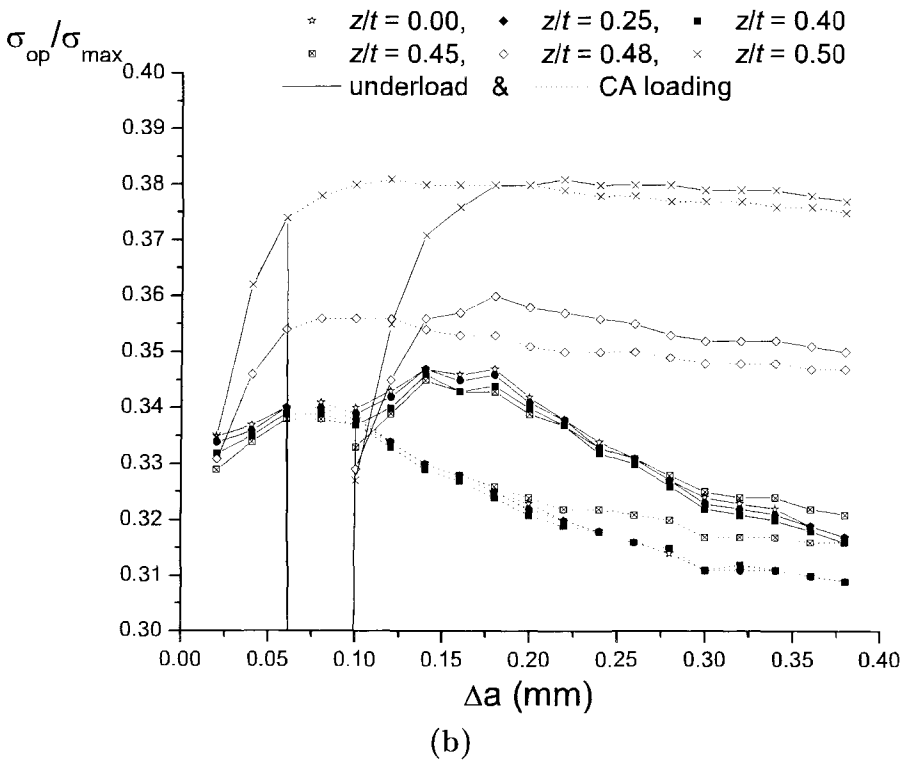


(b)

Figure 3.11: Crack opening stress profiles

*a) Ellyin-Xia model, and b) Kinematic hardening model.*

duced at the underload crack tip, A, which couple with compressive plastic deformation indicated in Figure 3.13(b-i combine to reduce the crack opening stress resulting in the acceleration effect seen in Figure 3.11(b). The profiles for 2 and 9 cycles after the underload in Figures 3.12(b-i) and (b-ii) respectively show that after the underload higher compressive residual stresses begin to develop along the crack surface (crack wake) as compared to the CA loading case. Although the strain profiles for these points show no difference from the CA profiles, see Figures 3.12(b-i) and (b-ii), the lower opening stress resulting due the underload leads to the acceleration effect seen in Figure 3.11(b).

## 3.6 Kinematic hardening vs. Ellyin-Xia material model

From the foregoing it was observed that the two models predict different trend as regards the effect of an overload or an underload. On close observation for the case of an overload, it is noticed that the marked different is in the unloading path of each load cycle. As mentioned in '*the statement of the problem*', Ellyin and Wu [10] have demonstrated that classical models such as the kinematic hardening model do not adequately capture the experimental response especially during the unloading process. This would explain why the Ellyin-Xia model predicted trends of the transient of an overload as seen in Figure 3.8(a) is in good agreement with the experiment observation of Skorupa [25] see Figure 3.5, while the kinematic model does not adequately predict this trend as shown in Figure 3.8(b).

The two models for the case of an underload both predict initial acceleration followed by a retardation effect. The retardation effect which is longer lasting in the kinematic model may be attributed to the inability of the model to appropriately capture the unloading process of a cycle. Also the strain profiles for the kinematic model after the underload shown in Figure 3.13(b) show no strain hardening at the underload crack tip, A, upon return to pre-underload loading values which would

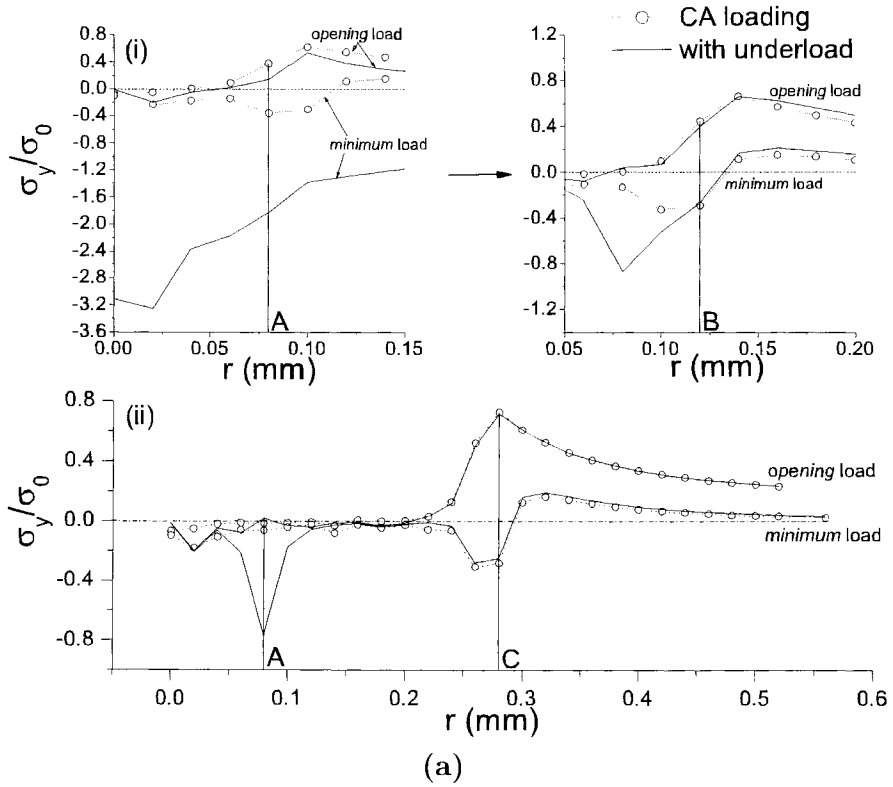


(a)

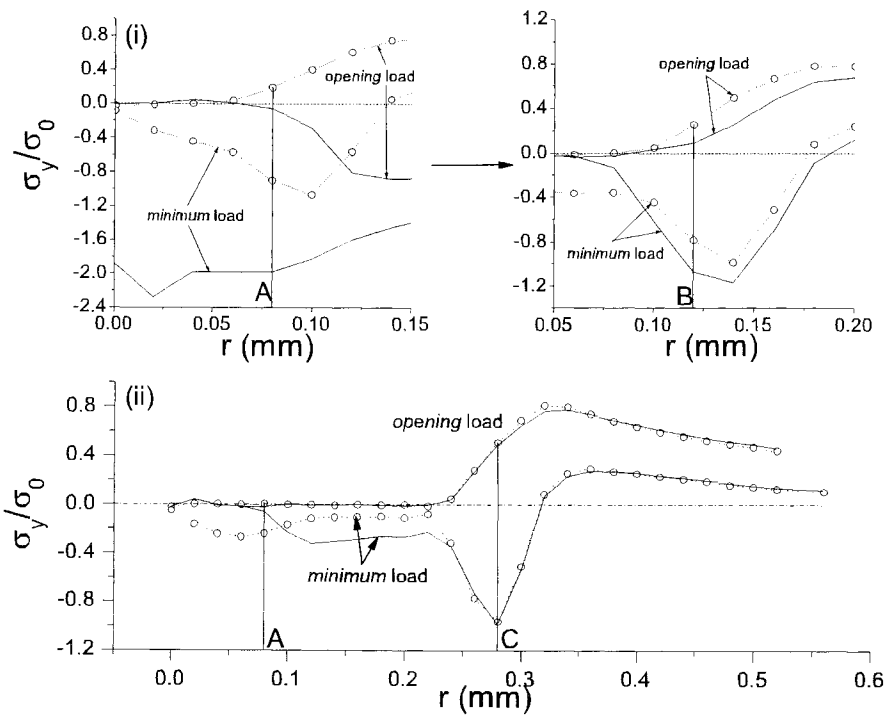


(b)

Figure 3.12: Distribution profiles of the stress component normal to the crack plane *a) Ellyin-Xia model, and b) Kinematic hardening model.*

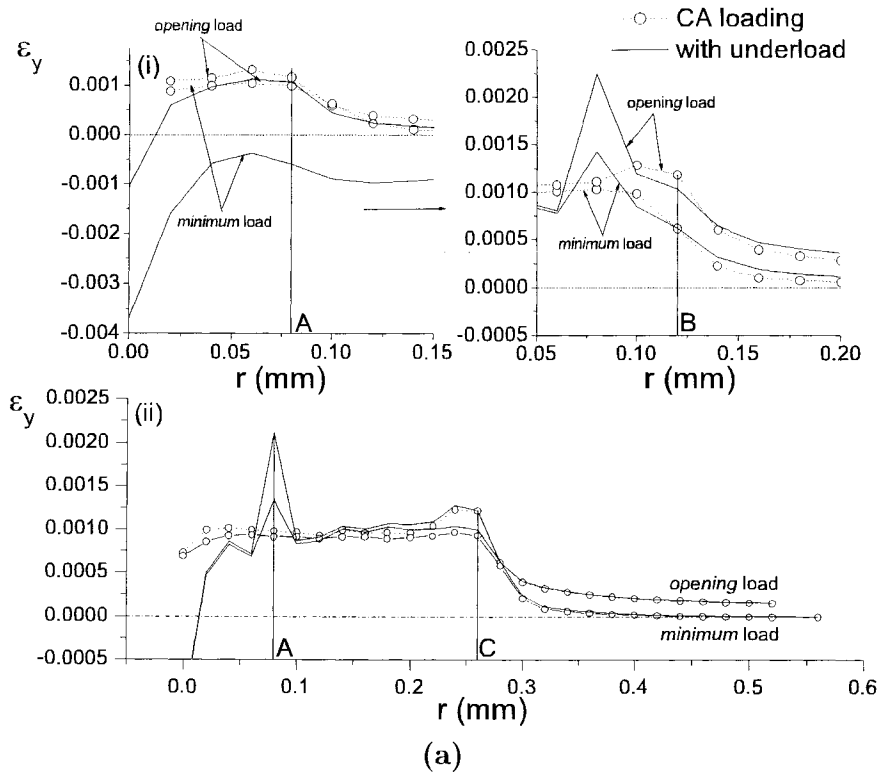


Figure 3.13: Distribution profiles of the strain component normal to the crack plane *a) Ellyin-Xia model, and b) Kinematic hardening model.*

explain the retardation effect. However, the Ellyin-Xia model predict a trend of strain hardening of the underload crack tip at the onset of the retardation effect as seen in Figure 3.13(a). This is attributed to the model's ability to capture the effects of cyclic plasticity accurately, and has been demonstrated by Ellyin and Meijer [9, 31].

# Bibliography


[1] C. Bichler and R. Pippan. Direct observation of the residual plastic deformation caused by a single tensile overload. In *Advances in Fatigue crack Closure Measurement and Analysis*, volume 2 of *ASTM STP 1343*, pages 191–206, Philadelphia, 1999.

[2] L. P. Borrego, J. M. Ferreira, J. M. Pinho da Cruz, and J. M. Costa. Evaluation of overload effects on fatigue crack growth and closure. *Engineering Fracture Mechanics*, 70(11):1379–1397, 2003.

[3] H. Buschermohler, Memhard D., and Vormwald M. Fatigue crack growth acceleration or retardation due to compressive overload excursions. In *Fatigue '96: Proceedings of the sixth international fatigue congress*, volume 1, pages 583–588, Berlin, Germany, 6-10 May 1996.

[4] R. L. Carlson and G. A. Kardomateas. Effects of compressive load excursions on fatigue crack growth. *International Journal of Fatigue*, 16(2):141–146, 1994.

[5] R. G. Chermahini, K. N. Shivakumar, and J. C. Newman Jr. Three-dimensional finite-element simulation of fatigue crack growth and closure. In *Mechanics of Fatigue Crack Closure*, ASTM STP 982, pages 398–413, Philadelphia, 1988.

[6] A. A. Dabayeh, C. MacDougall, and T. H. Topper. Crack opening stress reductions due to underloads and overloads in 2024-T351 Aluminum and SAE 1045 steel. In *Fatigue '96: Proceedings of the sixth international fatigue congress*, volume 1, pages 583–588, Berlin, Germany, 6-10 May 1996.

[7] J. D. Dougherty, T. S. Srivatsan, and J. Padovan. Fatigue crack propagation and closure behavior of modified 1070 steel: Experimental results. *Engineering Fracture Mechanics*, 56(2):167–187, 1997.

[8] W. Elber. The significance of fatigue crack closure. In *Damage Tolerance in Aircraft structure*, volume 486 of *ASTM STP*, pages 230–242, Philadelphia, 1971.

[9] F. Ellyin. *Fatigue Damage, Crack Growth and Life Prediction.* Chapman & Hall, London, 1997.

[10] F. Ellyin and J. Wu. Elastic-plastic analysis of a stationary crack under cyclic loading and effect of overload. *International Journal of Fracture*, 56:189–208, 1992.

[11] F. Ellyin and J. Wu. A numerical investigation on the effect of an overload on fatigue crack opening and closure behaviour. *Fatigue & Fracture of Engineering Materials and Structures*, 22(10):835–835, 1999.

[12] F. Ellyin and Z. Xia. A rate-independent constitutive model for transient non-proportional loading. *J. Mech. Phys. Solids*, 37(1):71–91, 1989.

[13] F. Ellyin, Z. Xia, and J. Wu. A new elastic-plastic constitutive model inserted into the user-supplied material model of ADINA. *Computers and Structures*, 56:189–208, 1992.

[14] Hammouda, Ahmad, Sherbini, and Sallam. Fatigue crack growth due to two successive single overloads. *Fatigue & Fracture of Engineering Materials and Structures*, 21(12):1537–1547, 1998.

[15] Hammouda, Ahmad, Sherbini, and Sallam. Deformation behaviour at the tip of a physically short fatigue crack due to a single overload. *Fatigue & Fracture of Engineering Materials and Structures*, 22(2):145–151, 1999.

[16] M. Jono. Fatigue life prediction - Acceleration of fatigue crack growth under variable amplitude loadings. In *Fatigue '96: Proceedings of the sixth international fatigue congress*, volume 1, pages 543–552, Berlin, Germany, 6-10 May 1996.

[17] M. S. Jono, Sugeta A., and Uematsu Y. Fatigue crack growth and crack closure behaviour of Ti-6Al-4V alloy under variable-amplitude loadings. In *Advances in Fatigue crack Closure Measurement and Analysis*, volume 2 of *ASTM STP 1343*, pages 265–284, Philadelphia, 1999.

[18] M. Lang. Description of load interaction effects by $\delta K_{eff}$ concept. In *Advances in Fatigue crack Closure Measurement and Analysis*, volume 2 of *ASTM STP 1343*, pages 207–223, Philadelphia, 1999.

[19] A. J. McEvily and S. Ishihara. On the development of crack closure at high R levels after an overload. *Fatigue & Fracture of Engineering Materials and Structures*, 25(11):993–993, 2002.

[20] S.-J. Park and J.-H Song. Simulation of fatigue crack closure behaviour under variable-amplitude loading by a 2D finite element analysis based on the most appropriate mesh size concept. In *Advances in Fatigue crack Closure Measurement and Analysis*, volume 2 of *ASTM STP 1343*, pages 337–348, Philadelphia, 1999.

[21] S. Pommier and Ph. Bompard. Bauschinger effect of alloys and plasticity-induced crack closure: a finite element analysis. *Fatigue & Fracture of Engineering Materials and Structures*, 23:129–139, 2000.

[22] M. S. Ramos, M. V. Pereira, Darwish F. A., Motta S. H., and Carneiro M. A. Effects of single and multiple overloading on the residual fatigue life of a structural steel. *Fatigue & Fracture of Engineering Materials and Structures*, 26:115–121, 2003.

[23] S. Roychowdhury and R. H. Dodds. Three-dimensional effects on fatigue crack closure in the small-scale yielding regime - a finite element study. *Fatigue & Fracture of Engineering Materials and Structures*, 26:663–673, 2003.

[24] S. Roychowdhury and R. H. Dodds Jr. A numerical investigation of 3-d small-scale yielding fatigue crack growth. *Engineering Fracture Mechanics*, 70(17): 2363–2383, 2003.

[25] M. Skorupa. Load interaction effects during fatigue crack growth under variable amplitude loading - a literature review. Part I: Empirical trends. *Fatigue & Fracture of Engineering Materials and Structures*, 21(8):987–1006, 1998.

[26] M. Skorupa. Load interaction effects during fatigue crack growth under variable amplitude loading - a literature review. Part II: Qualitative interpretation. *Fatigue & Fracture of Engineering Materials and Structures*, 22(10):905–926, 1999.

[27] K. N. Solanki. Two- and three-dimensional finite element analysis of plasticity-induced crack closure - a comprehensive parametric study. Master's thesis, Mississippi State University, Mississippi, 2002.

[28] R. R. Stephens, R. I. Stephens, D. E. Lemm, S. G. Berge, H. O. Liknes, and C. J. Cousins. Role of crack closure mechanisms on fatigue crack growth of Ti-62222 under constant-amplitude and transient loading at -54, 25, and 175°c. In *Advances in Fatigue crack Closure Measurement and Analysis*, volume 2 of *ASTM STP 1343*, pages 224–245, Philadelphia, 1999.

[29] G. Wheatley, X. Z. Hu, and Estrin Y. Effects of a single tensile overload on fatigue crack growth in 316l steel. *Fatigue & Fracture of Engineering Materials and Structures*, 22(12):1041–1051, 1999.

[30] J. Wu and F. Ellyin. A study of fatigue crack closure by elastic-plastic finite element analysis for constant-amplitude loading. *International Journal of Fracture*, 82(1):43 – 65, 1996.

[31] Ellyin F. Xia Z. and Meijer G. Mechanical behavior of $Al_2O_3$-particle-reinforced 6061 aluminum alloy under uniaxial and multiaxial cyclic loading. *Composites Science and Technology*, 57(2):237–248, 1997.

[32] R. Yang. Prediction of crack growth under complex loading cycles. *International Journal of Fatigue*, 16(6):397–402, 1994.

[33] J. Z. Zhang, M. D. Halliday, P. Bowen, and P. Poole. Three dimensional elastic-plastic finite element modelling of small fatigue crack growth under a single tensile overload. *Engineering Fracture Mechanics*, 63(3):229–251, 1999.

# Chapter 4

# 3D modelling of cyclically loaded Composite Patch Repair of a Cracked Plate

## 4.1 Introduction

This chapter deals with an extension to the crack problem considered in the preceding chapters: the bonded patch repair of a cracked structure. A considerable amount of research has been conducted on extending the service life of crack engineering structures with the emphasis on the life extension of aging aircraft structures using various repair techniques. The underlining theory of the any repair technique is the efficient transfer of load to the reinforcement from the cracked structure such that the driving force for crack propagation is reduced. The aim is to restore the damage tolerance and residual strength of the structure such that there is an overall reduction in the crack growth rate resulting in an extension in the service life of the structure.

In order to accomplish the requirement of efficient load transfer in the repaired structure, two techniques have been and are more widely employed for repairs in the aerospace industry. And these techniques have led researchers to investigate the effectiveness of crack repairs: (i) Mechanically fastened repairs which employ either bolts or rivets as fasteners to secure a metallic reinforcement to the cracked

structure. The fasteners introduce additional stress concentration due to the need to drill holes, and also the applied metallic reinforcement causes a discontinuity in the local geometry causing change in the stress distribution of the repair area resulting in additional stress concentration around the boundary of the of the repair area. Therefore, although the mechanically fastened repair may help to increase the service life of the structure, the additional stress concentrations generate further damage in the structure which provide the ideal environment for new cracks [2, 21, 26]. (ii) The development in the area of advanced composites with their high specific strength, high specific stiffness and excellent thermal characteristics and adhesives has made it possible to bond reinforcing patches to cracked metallic plates. The process, referred to as "crack patching" does not generate high stress concentrations by avoiding drilling of holes and providing better stress distribution in the repair area. The latter of these, crack patching technology has been proven to be an effective method for restoring the residual strength and damage tolerance of cracked structures [2, 5, 9, 20].

For the case of adhesively bonded patch repair, researchers have investigated the effectiveness of composite patch repairs for both thin and thick structures. Although majority of studies conducted on patch repair technology have considered the case of thin structure repair, a few of the mentioned studies have also investigated thick structure repair. These studies on thick structure repair generally consider the case where linear elastic fracture mechanics is sufficient to capture the behaviour of the base-plate. The present investigation extends the plasticity-induced crack closure model to the thin patch repair of a thick plate under constant amplitude loading conditions in order to obtain a good understanding of "thin patch" repair effectiveness while the base-plate is subject to the effects of cyclic plasticity. The words "thin patch" and "thick patch base-plate" are used in the sense that $t_p/t_{bp} << 1$, where $t_p$ is the patch thickness and $t_{bp}$ that of the base-plate.

## 4.2 State of the Art review

Adhesively bonded patch repair technology developed mainly due to the requirement to restore residual strength and also extend the fatigue service life of cracked aircraft structures. This led researchers to investigate the effectiveness of adhesively bonded patch repairs using both experimental and numerical techniques. These techniques allow investigators obtain an excellent understanding of how adhesively bonded patch repairs improve the durability and damage tolerance of the repaired structure [1, 3–26]. The review of literature for this study focuses on a numerical technique: the finite element method as a procedure to evaluate the effectiveness of adhesively bonded composite patch repair technology.

Ideally, the finite element (FE) analysis of a cracked structure repaired with an adhesively bonded composite patch is a 3-D problem. But this can become computationally intensive due to large number of nodal degrees of (DOF) required in a 3-D finite element model. Therefore to reduce cost and computation time, different FE models have been employed by researchers.

Two-dimensional finite element models require less modelling effort than three-dimensional models and also include fewer DOF. These include: models that utilized plane stress 2-D elements or Mindlin plate elements to model the cracked plate and the composite patch, and shear springs for the adhesive layer. Naboulsi and Mall [15–17] introduced a 2-D finite element three layer technique for the analysis of patch repairs of cracked metallic structures by employing Mindlin plate elements with transverse shear deformation capability for the base-plate, the adhesive and the composite patch. This technique was extended by Schubbe and Mall [20] for the modelling of cracked thick metallic structure repairs. Also various researchers [7, 8, 14] have employed a 2-D finite element code developed especially for fracture mechanics analysis by Cornell University. These 2-D models or pseudo 3-D models have the following limitation: The model cannot capture the crack front shape

which has been shown to influence the stress intensity factor variation through the thickness of the actual cracked structure [12, 21]. Thus a full 3-D model allows for a better understanding of the crack front shape evolution and through the thickness stress and strain distributions.

Three-dimensional models have also been employed with care taken while trying to limit the number of elements across the thickness of the finite element model to reduce the overall number of DOF in the model. This is due to the presence of an adhesive layer in the repair which has a thickness, $t_a$, such that $t_a << \{t_{bp}, t_p\}$ results in large aspect ratios that might compromise results. Umamaheswar and Ripudaman [24] utilized what they called "an intermediate model": single brick elements across the thickness of each component layer which gives a model size that matches that of 2-D models and a behaviour that agrees closely with a full 3-D model.

Following are design considerations taken into account when picking an adhesive and composite patch for the repair of a cracked structure:

**Adhesive**: The effectiveness of employing patch repair technology for the repair of a cracked structure would be highly dependent on the properties of the adhesive used to join the composite patch to the cracked structure. Therefore for efficient transfer of cyclic shear loads from the cracked structure to the composite patch, while resisting conditions that would weaken the bond resulting in the adhesive failure, the adhesive layer should have the following characteristics. The shear strength of the adhesive is maximized to obtain the strongest possible patch repair, and the peel stresses that result in de-bonding of the patch is minimized by optimizing the shape of the patch [7, 19].

**Composite patch**: The patch is made up of high-performance fibre reinforced composites which can be designed to meet specific application requirements. These composites have attributes which are of advantage to the designer [2, 5]:

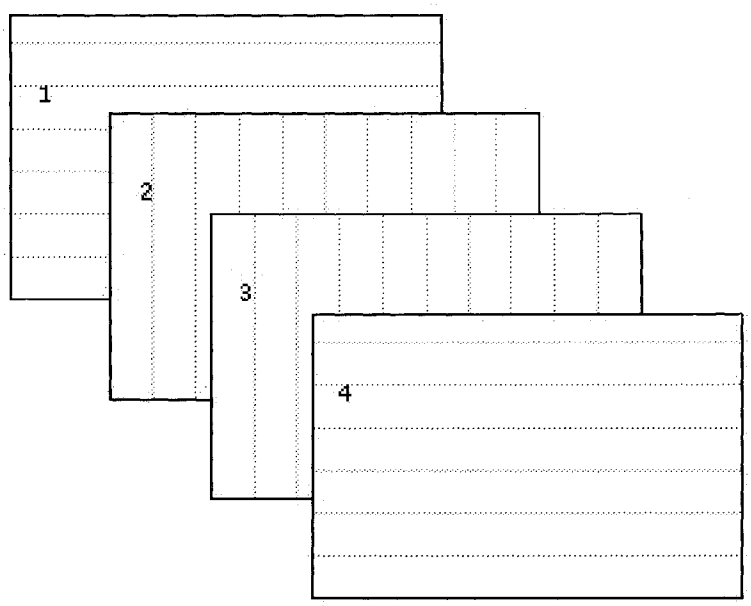


Figure 4.1: Layers of a composite patch
*Shown above is an example of a composite patch with* $[0/90]_S lay - up$

- composites can be designed to have high elastic modulus and stiffness which allows for reduced patch thickness such that the stiffness ratio of the repaired structure is given by:

$$S = \frac{E_p t_p}{E_{bp} t_{bp}} \tag{4.1}$$

  where the stiffness ratio, $S$, is maintained within the range: $1.0 < S < 1.5$

- a high resistance to damage by cyclic loading
- can be easily formed to complex shapes
- excellent corrosion resistance

The patch is designed such that the fibres are oriented perpendicular to the crack plane for the efficient transfer of loads for the base-plate to the patch. Figure 4.1 shows a $[0, 90]_S$ lay-up employed for the repair of a cracked plate subject to model I loading conditions. The edge of the patch is tapered to

reduce the effects of peel stresses on the structure which would otherwise result in de-bonding of the patch.

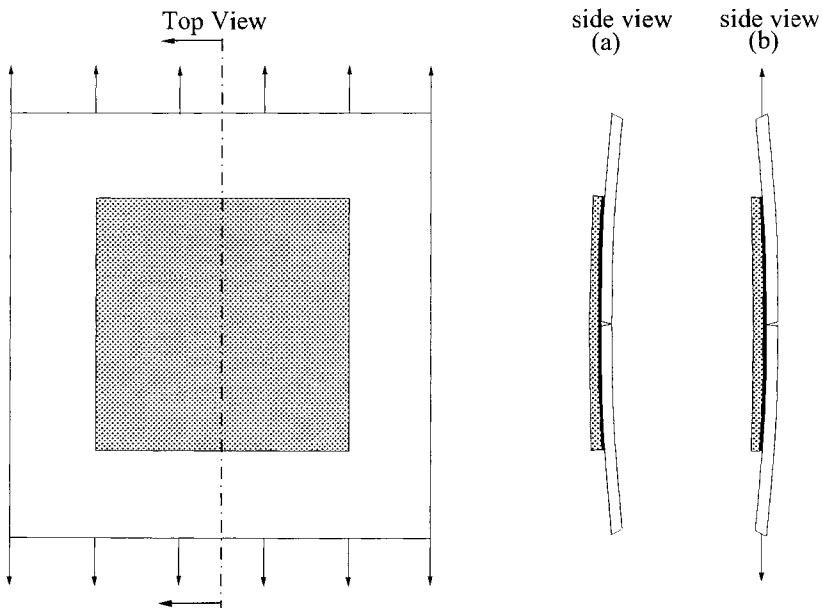


Figure 4.2: Bending effects of a single-sided repair
*Out-of-plane bending due to (a) thermal residual stresses, and (b) mechanical loading adopted from Ref.* [11]

Once the repair is made, the resulting symmetry of the repaired structure affects the overall effectiveness of the repair and these are usually of two types: symmetric (double-sided) repairs which provides for a more effective reinforcement to the cracked base-plate, and asymmetric (single-sided) repairs when only one face of the cracked structure is accessible for repair. Asymmetric repairs result in out-of-plane bending effects which occur due to: (i) A shift in the neutral axis of the repaired structure under mechanical loading conditions. (ii) A variation of the stress intensity factor across the thickness of the structure which is influenced by the crack tip shape [11, 12]. (iii) The mismatch in the coefficient of thermal expansion (CTE) of the base-plate structure and the patch repair results in asymmetric repairs and also in out-of-plane bending effects. Therefore the mismatch in the CTE must be taken into consideration to obtain an effective repair. As the $CTE_p$ of the patch

approaches that of the base-plate $CTE_{bp}$, the residual stresses that would result due to the CTE mismatch is reduced thus resulting in greater repair life. Figure 4.2 shows out-of-plane bending effects that result due to mechanical loading and thermal residual stresses for an asymmetric repair.

### 4.2.1 *Statement of the problem*

This investigation extends the application of the Ellyin-Xia constitutive relationship to the analyses of the adhesively bonded patch repair technology. The majority of works on the analyses of the adhesively bonded composite patch repairs consider two types of nonlinearity: geometrical nonlinearity and material nonlinearity of the adhesive. These works generally assume the base-plate to have linear elastic material properties. This helps simplify the analysis due to the fact that these investigations consider a thin base-plate ($t_{bp} < 3$mm) usually assumed to have the material properties of aluminium which has an elastic modulus that is usually smaller than that of the applied high-performance fibre reinforced patch (usually made of graphite/epoxy or boron/epoxy composites) employed for the repair. These meet the $1.0 < S = \frac{E_p t_p}{E_{bp} t_{bp}} < 1.5$ design requirement and also allows for linear elastic fracture mechanics to be employed for the analyses of the repaired structure: the base-plate. From the above inequality, it can be seen that when the elastic modulus of the composite patch is larger than that of the base-plate, the thickness of the patch may be reduced considerably resulting in a "thin patch repair" while providing the necessary stiffness and strength to allow for effective load transfer and bridging of the crack structure thereby restoring the damage tolerance and extending the fatigue life of the base-plate.

While for the case of a thick base-plate considered in this study, the material of base-plate has an elastic modulus which is higher than that of the composite patch. This implies that the requirement of $1.0 < S < 1.5$ cannot be maintained if the thickness of the composite patch, $t_p$, is desired to be limited such that $t_p < t_{bp}$.

Thus by limiting the patch repair to a "thin repair", the overall patch stiffness and strength are such that they lead to the inadequacy of linear elastic fracture mechanics for the evaluation and analyses of the base-plate in the repaired structure. Therefore for this case one must employ an elastic-plastic analysis of the base-plate to capture the inelastic domain around the crack tip and the resulting closure phenomenon associated with the cyclic plasticity.

Therefore, the model employed to study the plasticity induced crack closure phenomenon in the previous chapters is extended to investigate the adhesively bonded patch repair of a cracked plate. Due to the limitations of the more commonly employed classical material models to adequately capture the effects of cyclic plasticity, the Ellyin-Xia material model is employed as the elastic-plastic formulation needed to describe the behaviour of the base-plate. Also in order to obtain a better understanding of the opening process in the base-plate for a patch repair, a 3-D model is employed to capture the crack tip opening stress profile and the crack surface displacement profile across the thickness.

## 4.3 Finite Element Model

The 3-D finite element model of the adhesively bonded composite patch repair of a cracked plate employs the same geometrical configuration as the cracked plate used in the previous investigations, Chapters 2 and 3 for the base-plate. Therefore, the geometrical model and mesh for the previous studies was extended to include the adhesive and patch layers, and the initial boundary conditions were changed to incorporate the addition of the adhesively bonded patch. Thus, the APDL batch script was modified to account for these changes, with other parts of the script: the determination of crack opening values, loading conditions, and the computational code remaining the same as in previous investigations. The finite element computation script remains similar to that employed earlier, therefore only a summary of the hypotheses is presented:

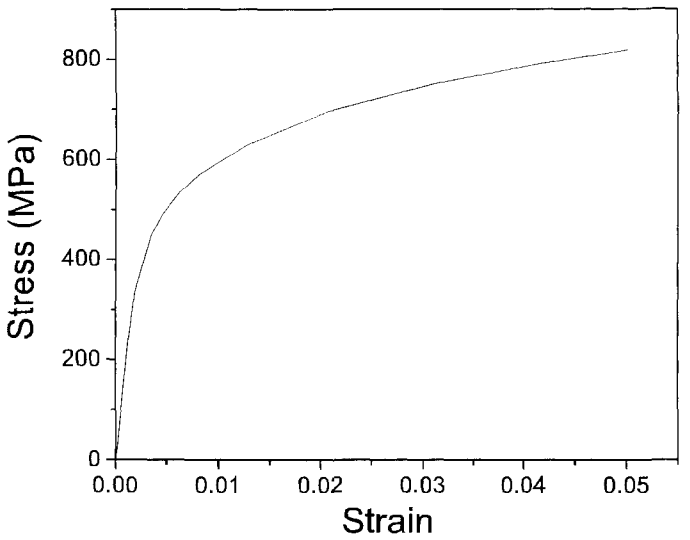


Figure 4.3: Stress-strain curves

*The virgin (initial) and stable (saturated) cyclic curves are the same for this study*

- **Mesh generation and definition of the material properties**: The geometrical model of the repaired crack is composed of: a cracked base-plate assumed to have ASTM 516 Gr. 70 steel incorporating the Ellyin-Xia model (see Figure 4.3 for the stress-strain curve) with an initial crack length, $2a = 8$mm, an adhesive layer and graphite/epoxy composite patch. The material properties used in this study are given in Table 4.1 and the geometrical configuration and mesh of the model are shown in Figure 4.4(a) and 4.4(b) respectively.

  A double-sided patch repair is considered for this study in order to eliminate bending effects due to a shift in the neutral axis if a single-sided repair is considered. This allows only one-eighth of the geometry to be modelled due to symmetry about the $xy$, $yz$ and $zx$ planes. The mesh of the base-plate is composed of 3-D 8-nodes structural solids of the 18x family element, SOLID185, while the adhesive and patch are composed of 3-D 8-nodes SOLID45 elements of ANSYS computer code. The mesh has smallest element length $\Delta a = 0.02$mm in the vicinity of the crack tip with five layers through the half thickness of the

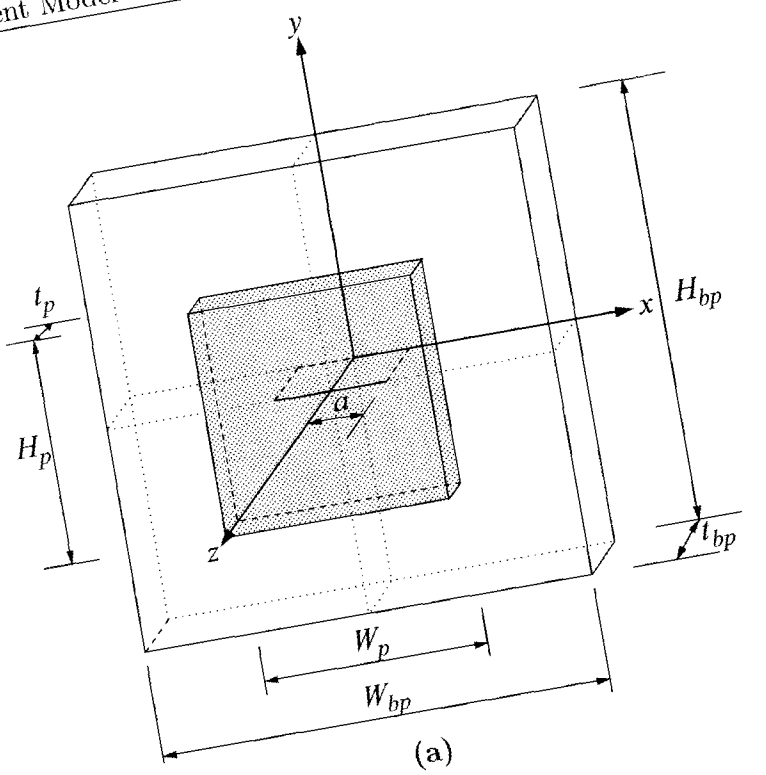


(a)

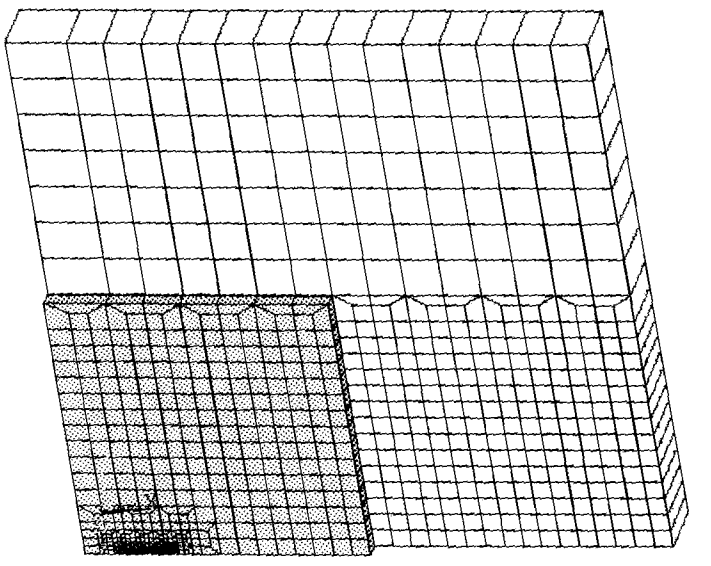

(b)

Figure 4.4: (a) Geometrical configuration of the adhesively bonded composite repair of a cracked plate, and (b) Finite element mesh

Table 4.1: Material properties of base-plate, adhesive and patch

| *Layer* | *Length* $L$ (mm) | *Width* $W$ (mm) | *Thickness* $t$ (mm) | *Material properties* |
|---|---|---|---|---|
| Steel base-plate | $L_{bp} = 80$ | $W_{bp} = 80$ | $t_{bp} = 8$ | $E = 204$GPa<br>$\nu = 0.30$<br>$\sigma_o = 230$MPa |
| Adhesive | $L_a = 40$ | $W_a = 40$ | $t_a = 0.125$ | $E = 2.4$GPa<br>$\nu = 0.33$ |
| Composite Patch | $L_p = 40$ | $W_p = 40$ | $t_p = 2 \rightarrow 8$ | $E_y = 134$GPa<br>$E_x = E_z = 10.3$GPa<br>$\nu_{xy} = \nu_{yz} = 0.33$<br>$\nu_{xz} = 0.53$<br>$G_{xy} = G_{yz} = 5.5$GPa<br>$G_{xz} = 3.2$GPa |

base-plate around the crack tip(i.e $0.25t_{bp}$, $0.15t_{bp}$, $0.05t_{bp}$, $0.03t_{bp}$ and $0.02t_{bp}$) with the smallest layer located adjacent to the adhesive layer to allow the capture of the rapid changing state of stress across the thickness of the geometry. The rest of the mesh is composed of single elements across the thickness to limit the total number of elements, therefore allowing for fast computation time.

- **Application of initial boundary conditions**: The boundary conditions of the previous investigations were extended to appropriately capture a double-sided adhesively bonded patch repair. The crack repair problem remains a variable boundary value problem, therefore taking advantage of the three planes of

symmetry the following initial boundary conditions are applied to the model:

$$u_x(0,y,z)=0 \rightarrow \begin{cases} 0 \le y \le H_{bp}/2; & 0 \le z \le t_{bp}/2 \\ 0 \le y \le H_a/2; & t_{bp}/2 \le z \le t_a \\ 0 \le y \le H_p/2; & (t_{bp}/2+t_a) \le z \le t_p \end{cases}$$

$$u_y(x,0,z)=0 \rightarrow \begin{cases} a \le x \le W_{bp}/2; & 0 \le z \le t_{bp}/2 \\ a \le x \le W_a/2; & t_{bp}/2 \le z \le t_a \\ 0 \le x \le W_p/2; & (t_{bp}/2+t_a) \le z \le t_p \end{cases}$$

$$u_z(x,y,0)=0 \rightarrow 0 \le x \le W_{bp}/2; \quad 0 \le y \le H_{bp}/2$$

The model was then loaded through 20 cycles with a maximum stress, $\sigma_{max} = 0.3\sigma_0$ employing a script in the following form:

- **Loading path and determination of crack opening values**: The model was loaded incrementally using small load steps to allow the accurate capture of the crack opening values along the thickness of the model which are obtained by monitoring the reaction forces at the crack tip nodes. When the reaction force is in tension the crack is fully open [28]

- **Crack advance**: The crack is advanced by one element at the top of a load cycle, i.e at maximum load.

- **Unloading path and crack surface contact**: During the unloading path, the model was unloaded using small load steps to permit the proper simulation and capture of the crack surface contact process. The displacement values of the crack surface nodes were monitored, and once a surface node has negative displacement the node is constrained in the crack surface plane. At minimum load before the reloading, the constrains on the surface nodes are removed before reloading.

## 4.4 Displacement profile

Figures 4.5(a) and 4.5(b) show the crack displacement profile at crack tip when the crack just becomes fully opened for the mid-plane of the base-plate and the base-

plate surface bonded to the patch respectively for the 14th load cycle. Patch A represents the patch with thickness 0.5mm, B: 1mm, C: 2mm, and D: 4mm. The results show that as the thickness of the patch is increase the displacement profile of the base-plate decreases through the thickness.

Also Figures 4.6(a) and 4.6(b) show the base-plate displacement profile at $\sigma_{max}$ for the mid-plane and the surface bonded to the patch respectively for the 14th load cycle. Likewise it can be seen that as the patch thickness is increased the displacement profile decreases. Taking a closer look at these figures show that the effects of plastic deformation are present and results in the sudden change which can be seen at the point corresponding to the initial crack tip (i.e $r = 0$) [27]. The change in the displacement profiles at $r = 0$ is more prominent when the crack just becomes fully open, Figures 4.5(a) and 4.5(b), then for the profiles at maximum load, Figures 4.6(a) and 4.6(b). These jumps in displacement profile can be attributed to the build-up of residual stresses and wake plasticity at and ahead of the initial crack tip (in the region $r \leq 0$) which results in plasticity-induced closure as the crack propagates. Therefore, this region $r \leq 0$ experiences the effects of PICC resulting in lower displacement profiles as compared to if the region was subject to only elastic deformation. Therefore as stated in the *"Statement of the Problem"* when considering a repair where the stiffness, S, requirement can not be met it would be necessary to employ a model with an accurate elastic-plastic formulation that would capture the resulting contribution or effects of cyclic plasticity on the repaired structure.

The Influence of the patch repair on the plate can be seen in Figures 4.7 and 4.8 for the 14th load cycle, and Table 4.2 gives the crack tip opening displacement (CTOD) values for the patched and unpatched cases and the ratio $\text{CTOD}_{pd}/\text{CTOD}_{unpd}$. CTOD is taken as the displacement of the nodes an element $\Delta a_e$ behind the crack tip. Figure 4.7 and Table 4.2 show the CTOD profiles through the thickness of the

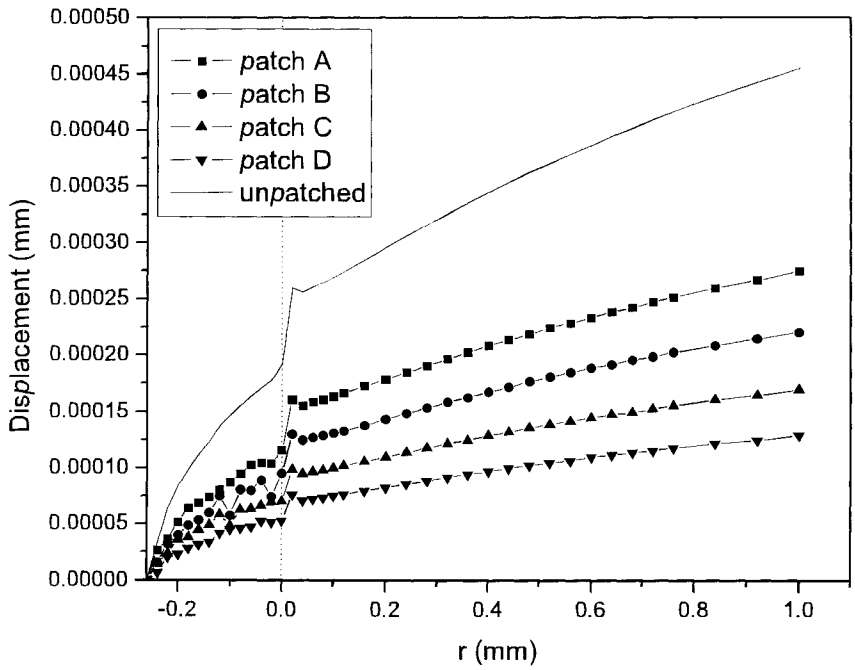


(a)

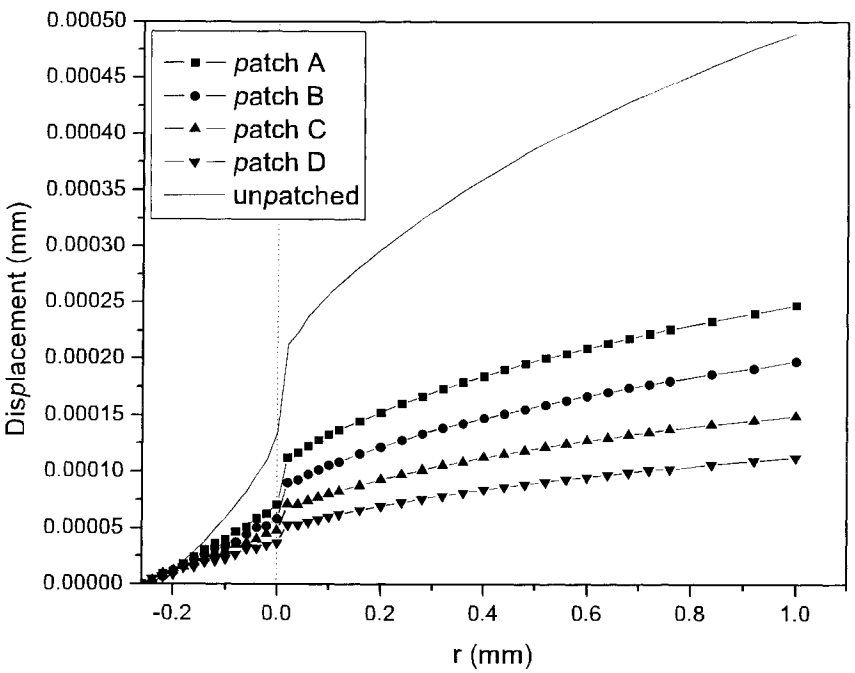


(b)

Figure 4.5: (a) Crack displacement profile for the mid-plane, and (b) surface adhesively bonded to the patch at crack opening

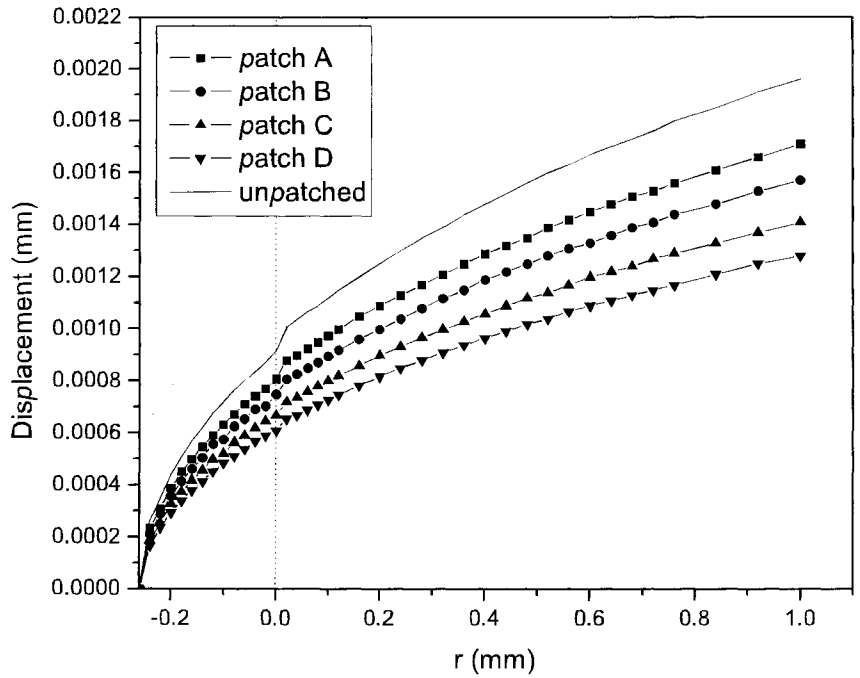


(a)

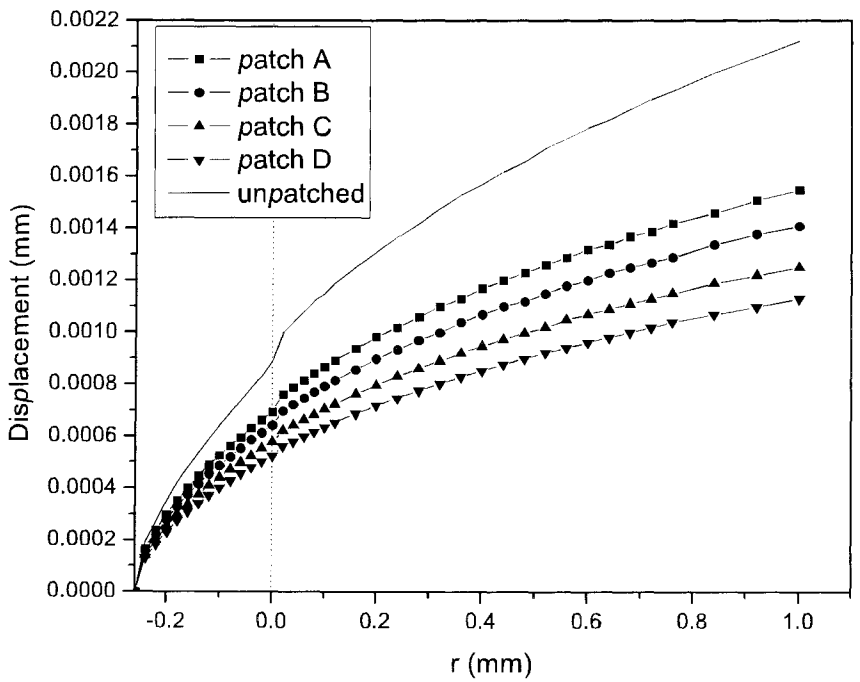


(b)

Figure 4.6: (a) Crack displacement profile for the mid-plane, and (b) surface adhesively bonded to the patch at maximum load

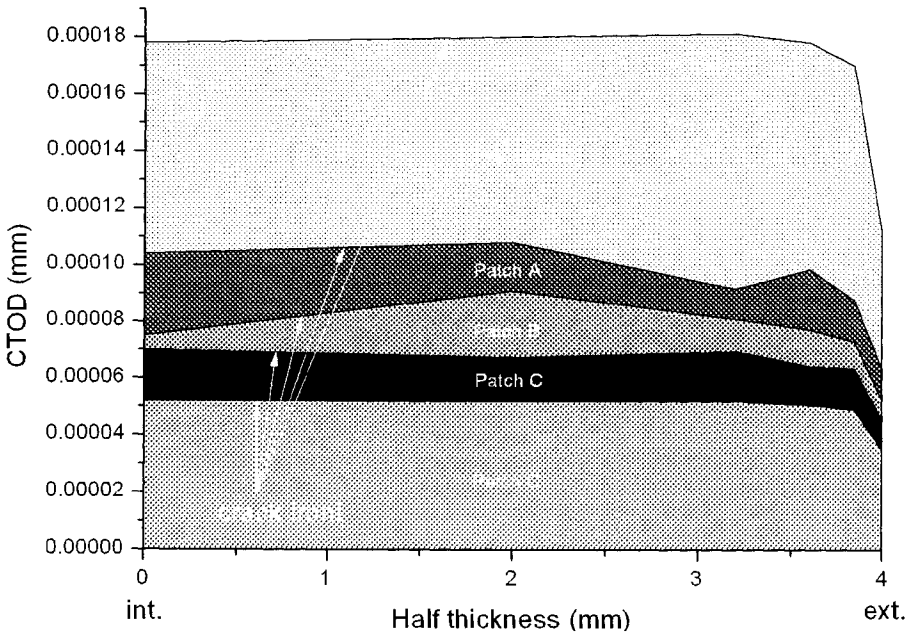


Figure 4.7: CTOD (a $\Delta a_e$ element behind the crack front) profile through the thickness of the plate for the unpatched and patched cases at crack opening load

cracked plate at the point the crack becomes open. It can be seen that the patch repair has a closure effect on the CTOD profiles with reductions in displacements as the patch thickness is increased (Patch A $\rightarrow$ D). A similar trend can be seen in Fig. 4.8 and Table 4.2, the through thickness CTOD profiles at maximum load. This implies that $\delta_t$ is reduces by the patch repair, and is more effective with an increase in patch thickness. For small scale yielding:

$$\delta_t \propto \frac{J}{\sigma_0} \approx \frac{K_{eff}^2}{E\sigma_0} \tag{4.2}$$

Therefore reducing $\delta_t$ results in a reduction in the $K_{eff}$ the driving force for crack growth. If $K_{eff} \leq K_{TH}$ then there will be no crack growth.

## 4.5 Opening stress profile and $K$ profile

The opening stress profiles for the mid-plane of the base-plate and the surface bonded to the patch are shown in Figures 4.9 and 4.10 respectively. It can be seen that as

the thickness of the patch is increased the effects of cyclic plasticity on the base-plate is reduced. Also, since the opening stress values for all the patch thicknesses considered are greater then zero (i.e $\sigma_{op}/\sigma_{max} > 0$) it implies that the effects of cyclic plasticity are present in the base-plate and would contribute to or affect the effectiveness of the patch repair. Therefore the plots show that although the patch provides a load transfer reinforcement to the base-plate thereby resulting in an increase in damage tolerance and service life of the repaired structure, the effects of cyclic plasticity (plasticity-induced crack closure) are also beneficial to the repair. Since the plate undergoes small scale yielding in the vicinity of the crack front, the path independent $J$-Integral is used to obtain the $K$ (Eqn. 4.2) as a measure of the crack growth driving force. Figure 4.11 shows the $K$ profile through the thickness of the plate for both unpatched and patched cases. The plot shows that the patch repair strongly influences the driving force for crack growth at the surface of the cracked base-plate ($z/t = 0.50$) to which the patch is bonded, the *outer surface*: patch A $\rightarrow$ D show a large decrease in the driving force, $K$. Also for the nodes at $z/t = 0.48$ - the *adjacent plane to outer surface*, through to $z/t = 0.00$ - the *mid-plane*, there is a significant reduction in the driving force values as compared to the unpatched case. This trend implies that the patch repair is effective in reducing the driving force for crack propagation.

Although the general trend is a reduction in $K$ values, a careful look at Figure 4.11 shows that as patch thickness increases, $K$ values decrease at the outer surface, while at the adjacent plane through to the mid-plane $K$ values increase. The latter phenomenon can be attributed to the effects of PICC which also contribute to reduce $K$, therefore as patch thickness increases the contributing effects of PICC in lowering $K$ is reduced.

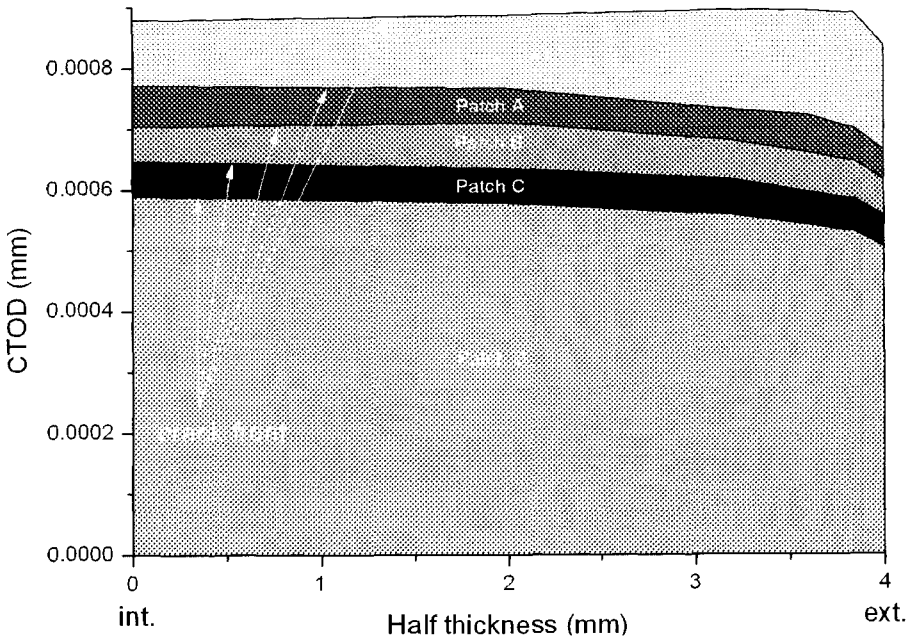


Figure 4.8: CTOD (a $\Delta a_e$ element behind the crack front) profile through the thickness of the plate for the unpatched and patched cases at maximum load

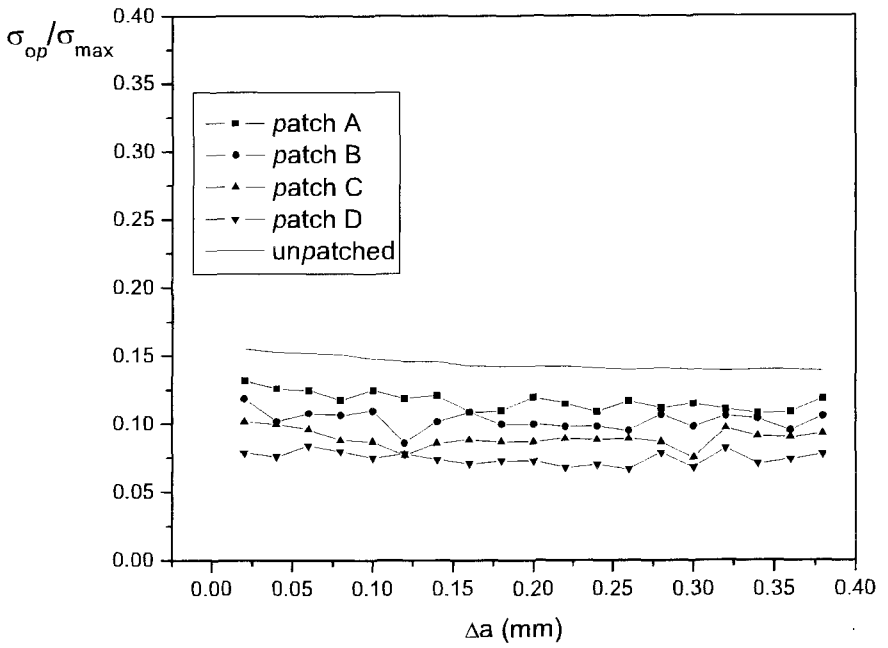


Figure 4.9: Stress opening profile for the mid-plane of the base-plate

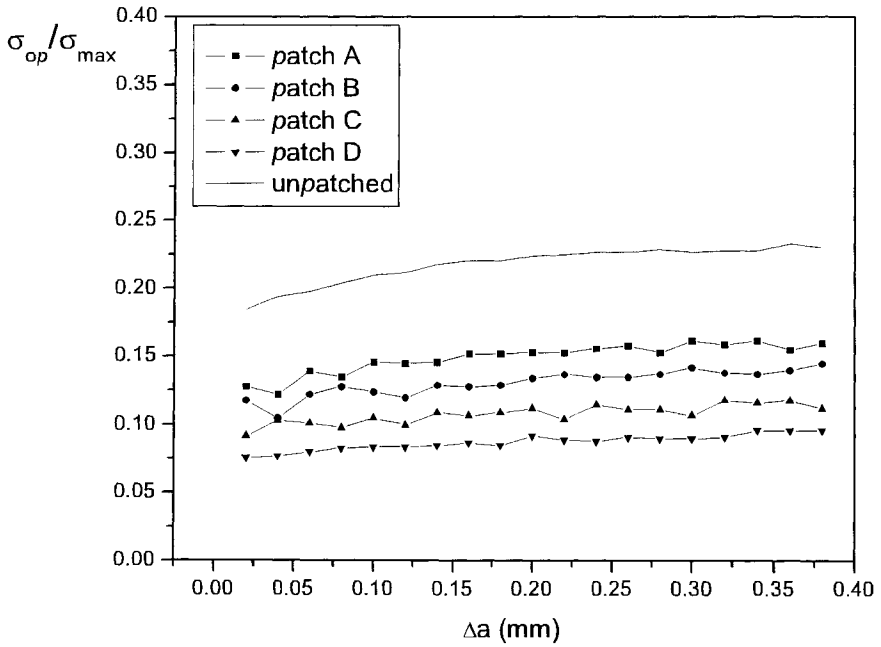


Figure 4.10: Stress opening profile for surface adhesively bonded to the patch

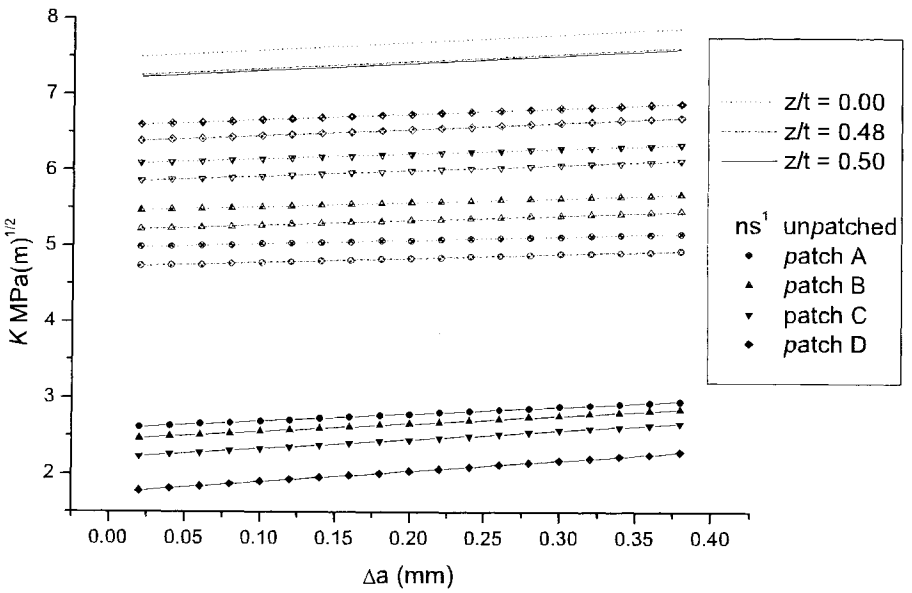


Figure 4.11: $K$ profile through the thickness of the plate for the unpatched and patched cases. [1] ns = no symbol

Table 4.2: CTOD through the thickness of the plate

| Parameters | Displacement at crack tip | | | | | | | | | |
|---|---|---|---|---|---|---|---|---|---|---|
| | Unpatched | | Patched | | | | | | | |
| | | | A | | B | | C | | D | |
| | int. | ext. | int. | ext. | int. | ext. | int. | ext. | int. | ext. |
| CTOD crack open | 1.78e-4 | 1.11e-4 | 1.04e-4 | 6.31e-5 | 7.5e-5 | 5.23e-5 | 7.01e-5 | 4.51e-5 | 5.2e-5 | 3.48e-5 |
| $CTOD_{pd}/CTOD_{unpd}$ | 1 | 1 | 0.58 | 0.57 | 0.42 | 0.47 | 0.39 | 0.41 | 0.29 | 0.31 |
| CTOD max. load | 8.78e-4 | 8.34e-4 | 7.71e-4 | 6.62e-4 | 7.04e-4 | 6.13e-4 | 6.47e-4 | 5.54e-4 | 5.89e-4 | 5.03e-4 |
| $CTOD_{pd}/CTOD_{unpd}$ | 1 | 1 | 0.88 | 0.79 | 0.80 | 0.74 | 0.74 | 0.66 | 0.67 | 0.60 |

# Bibliography


[1] R. H. Andruet. *Special 2-D and 3-D Geometrically Nonlinear Finite Elements for Analysis of Adhesively Bonded Joints.* PhD thesis, Virginia Polytechnic Institute and State University, Blacksburg, Virginia, 1998.

[2] J. B. Avram. Fatigue response of thin stiffened aluminum cracked panels repaired with bonded composite patches. AFIT/GMS/ENY/01M-01, School of Engineering, Air Force Institute of Technology (AU), Wright-Patterson AFB OH, 2001.

[3] A. A. Baker. Repair of cracked of defective metallic components with advanced fibre composites - an overview of Australian work. *Composite Structures*, 2: 153–181, 1984.

[4] A. A. Baker. Crack patching: Experimental Studies, Practical Applications. In *Bonded Repair of Aircraft Structure*, pages 107–172, Dordrecht, 1988. Martinus Nijhoff Publishers.

[5] A. A. Baker. Bonded composite repair for fatigue-cracked primary aircraft structure. *Composite Structures*, 47:431–443, 1999.

[6] A. A. Baker, R. J. Callinan, M. J. Davis, R. Jones, and J. G. Williams. Repair of mirage III aircraft using BFRP crack patching technology. *Theoretical and applied fracture mechanics*, 2:1–16, 1984.

[7] M. Belhouari, B. B. Bouiadjra, A. Megueni, and K. Kaddouri. Comparison of double and single bonded repairs to symmetric composite structures: a numerical analysis. *Composite Structures*, 65:47–53, 2004.

[8] B. B. Bouriadjra, M. Belhouari, and B. Serier. Computation of stress intensity factors for repaired cracks with bonded composite patch in mode I and mixed mode. *Composite Structures*, 56:401–406, 2002.

[9] K.-H. Chung and W.-H. Yang. A study on the fatigue crack growth behaviour of thick aluminum panels repaired with a composite patch. *Composite Structures*, 60:1–7, 2003.

[10] R. Jones, S. Barter, L. Molent, and S. Pitt. Crack patching: an experimental evaluation of fatigue crack growth. *Composite Structures*, 67:229–238, 2005.

[11] J. C. Klug and C. T. Sun. Large deflection effects of cracked aluminum plates repaired with bonded composite patches. *Composite Structures*, 42:291–296, 1998.

[12] W.-Y. Lee and J.-J. Lee. Successive 3d fe analysis technique for characterization of fatigue crack growth behavior in composite-repaired aluminum plate. *Composite Structures*, 66:513–520, 2004.

[13] R. Z. Marioli-Riga, G. J. Tsamasphyros, and G. N. Kanderrakis. Design of emergency aircraft repairs using composite patches. *Mechanics of Composite Materials and Structures*, 8:199–204, 2001.

[14] A. Megueni, B. Bachir Bouiadjra, and B. Boutabout. Computation of the stress intensity factor for patched crack with bonded composite repair in pure mode ii. *Composite Structures*, 59:415–418, 2002.

[15] S. Naboulsi and S. Mall. Modeling of a cracked metallic structure with bonded composite patch using the three layer technique. *Composite Structures*, 35: 295–308, 1996.

[16] S. Naboulsi and S. Mall. Nonlinear analysis of bonded composite patch repair of cracked aluminum panels. *Composite Structures*, 41:303–313, 1998.

[17] S. Naboulsi and S. Mall. Characterization of fatigue crack growth in aluminum panels with a bonded composite patch. *Composite Structures*, 37:321–334, 1997.

[18] M. Nishino and Aoki T. Nonlinear analysis and damage monitoring of a one-sided patch repair with delamintion. *Composite Structures*, In Press, Corrected Proof, 2005.

[19] P. D. Roberts. Patching cracked steel pressure vessels. Master's thesis, University of Alberta, Edmonton, Alberta, 1995.

[20] J. J. Schubbe and S. Mall. Modeling of cracked thick metallic structure with bonded composite patch repair using three-layer technique. *Composite Structures*, 45:185–193, 1999.

[21] D.-C. Seo and J.-J. Lee. Fatigue crack growth behavior of cracked aluminum plate repaired with composite patch. *Composite Structures*, 57:323–330, 2002.

[22] G.-C. Tsai and Shen S. B. Fatigue analysis of cracked thick aluminum plate bonded with composite patches. *Composite Structures*, 64:79–90, 2004.

[23] T. V. R. S. Umamaheswar and R. Singh. Modelling of patch repairs to a thin cracked sheet. *Engineering Fracture Mechanics*, 62:267–289, 1999.

[24] T. V. R. S. Umamaheswar and R. Singh. Modeling strategies for a single-sided repair. In *The Third Joint Conference on Aging Aircraft 1999*, ASTM STP 1343, 1999.

[25] C. H. Wang. Fatigue crack closure analysis of bridged cracks representing composite repairs. *Fatigue & Fracture of Engineering Materials and Structures*, 23: 477–488, 2000.

[26] W.-C. Wang and J.-S. Hsu. Investigation of the size effect of composite patching repaired on edge-cracked plates. *Composite Structures*, 49:415–423, 2000.

[27] J. Wu. *Nonlinear Analyses of Cracked Bodies*. PhD thesis, University of Alberta, Edmonton, Alberta, 1995.

[28] J. Wu and F. Ellyin. A study of fatigue crack closure by elastic-plastic finite element analysis for constant-amplitude loading. *International Journal of Fracture*, 82(1):43 – 65, 1996.

# Chapter 5

# Conclusions & Future work

## 5.1 Conclusions

The purpose of this thesis was to study the mechanics of the plasticity-induced crack closure phenomenon in a cracked plate subject to: (i) constant amplitude loading conditions, and (ii) variable amplitude (effect of an overload/underload) loading conditions while employing a material constitutive relation proposed by Ellyin and Xia to capture the effects of cyclic plasticity. The results obtained with this material model were compared to the results obtained from the classical kinematic hardening model.

The following conclusions were obtained from considering the crack opening stress profiles across the thickness, the stress and strain distribution profiles, and crack displacement profiles. For the case of constant amplitude loading:

1. The results obtain with the Ellyin-Xia model show a lower crack opening stress profile as compared to the classical kinematic hardening model. This may be attributed to the way in which each model captures the unloading path of a load cycle. As stated in the preceding chapters, the classical material models do not accurately capture the unloading and reloading paths during a load cycle, while the Ellyin-Xia model captures them accurately by employing two hyper-surfaces and two types of loading.

And for the case of variable amplitude loading:

2 The results of the analysis for a single spike overload when employing the Ellyin-Xia model show trends that are in good agreement with experimental observations: post overload retardation in crack growth rate followed by a gradual return to pre-overload rates. While the classical kinematic hardening model shows retardation effect which remains constant and does not return to pre-overload levels.

3 In the event of a single spike underload (compressive overload), the results obtained when employing the Ellyin-Xia model agrees with both "types" of experimental observations. That is, there is a marked acceleration in the crack growth rate and then a slight retardation before the growth rate returns to pre-underload growth rates. While the results obtained with the classical kinematic hardening model show a marked acceleration which is more pronounced and a retardation effect that is also longer lasting.

These differences are also attributed to the inability of the classical models to accurately capture the unloading process of a load cyclic.

Also this thesis extends the use of the Ellyin-Xia model to investigate the effects of cyclic plasticity on the effectiveness of an adhesively bonded composite patch repair of a cracked structure where an elastic-plastic formulation is necessary for the base-plate.

4 The results show that the plasticity-induced crack closure phenomenon is beneficial to the repair when the base-structure still undergoes plastic deformations.

## 5.2 Future Work

This research may be extended for future works in the areas plasticity-induced crack closure, and patch repair technology. Areas of interest for plasticity-induced crack closure include: the use of a criterion for crack propagation, consideration of mixed mode loading conditions, and a mesh that would permit the capture of crack front

shape evolution. And for patch repair technology: the consideration of bending effects (i.e single-sided repairs and CTE mismatch), and geometric and material nonlinearities of the adhesive.

# Appendix A

# Verification of Ellyin-Xia Model

This appendix compares results of the implementation of the Ellyin-Xia elastic-plastic constitutive relation into ANSYS using the User Programmable Features subroutine USERMAT with results obtained by Ellyin et. al. from the implementation of the model into ADINA which were verified with experimental results.

Two examples simulated in ADINA by Ellyin and co-researchers are simulated in ANSYS. Theses examples are modelled using SOLID185, a 3-D 8-node structural solid, which allows the use of USER subroutine USERMAT. For these problems only one element is used in a uniform stress state, with the material properties for 304 stainless steel. Material properties inputed into the computation code include; elastic modulus $E$, elastic Poisson's ratio $\nu$, $R_{lim}$, , and two uniaxial stress-strain curves, the virgin state and saturated state as discussed in chapter 3. Full details on the examples and the material properties are not included here, and can be obtained from Ellyin and co-researchers.

### Transient nonproportional cyclic responses

The single element model is subject to three types of non-proportional strain cycling in axial-torsional strain space. Figures A.1 and A.2 show that the ANSYS results are in good agreement with the ADINA results. Note scale difference between left and right Figures.

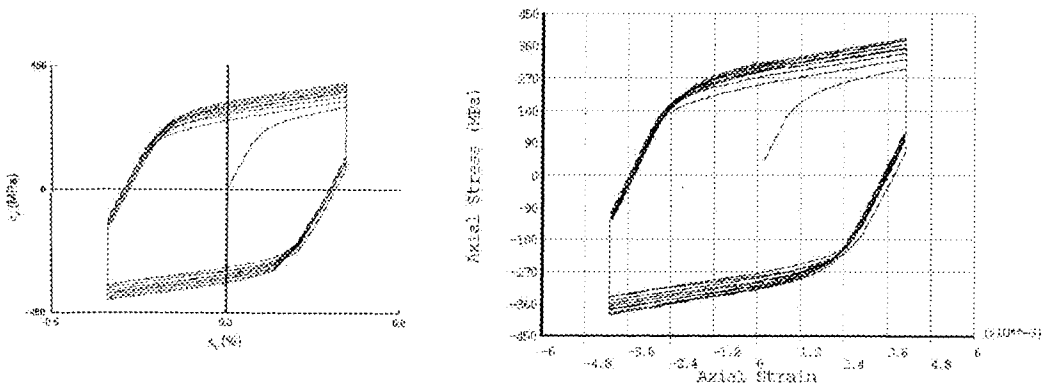


Figure A.1: Non-proportional transient cyclic loading - Part I
*Left: ADINA result; right: ANSYS result*

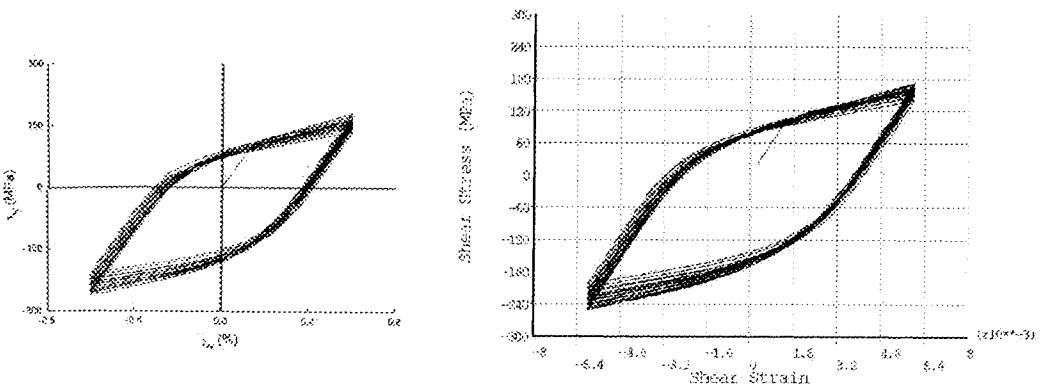


Figure A.2: Non-proportional transient cyclic loading - Part II
*Left: ADINA result; right: ANSYS result*

### Ratcheting under cyclic loading with mean stress

For this example, the single element model is subjected to a displacement load $\pm 0.002$, and a hoop stress of 80MPa. The results are shown in Figures A.3, A.4 and A.5 are in good agreement with the results from ADINA. Note scale difference between left and right Figures.

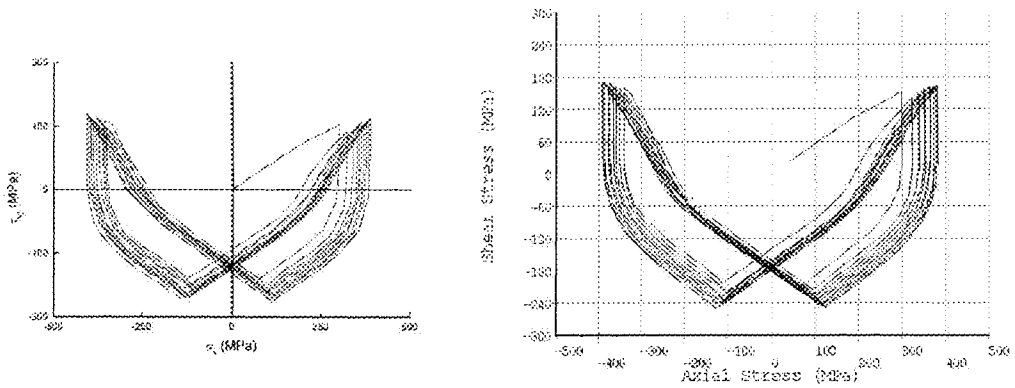


Figure A.3: Ratcheting under cyclic loading with mean stress - Part I
*Left: ADINA result; right: ANSYS result*

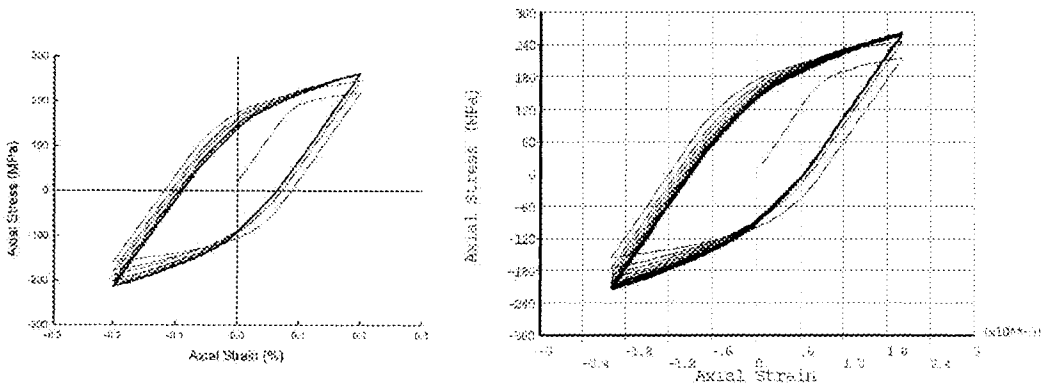


Figure A.4: Ratcheting under cyclic loading with mean stress - Part II
*Left: ADINA result; right: ANSYS result*

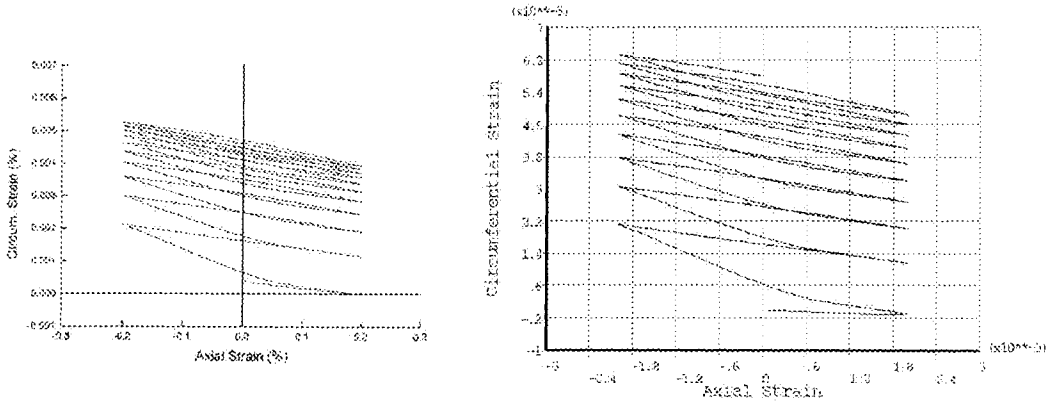


Figure A.5: Ratcheting under cyclic loading with mean stress - Part III
*Left: ADINA result; right: ANSYS result*